THE UNIVERSITY *of* EDINBURGH

Numerical Studies of Composite Higgs Models

Alessandro Lupo

Doctor of Philosophy
The University of Edinburgh
July 2023

Abstract

The Standard Model (SM) of particle physics describes the strong and electro-weak interactions with remarkable accuracy. Despite its success open questions, such as the Naturalness problem of the Higgs boson's mass, suggest that the SM has to be considered an effective theory valid up to a certain cutoff scale at least in the TeV range.

Models in which the Higgs boson emerges as a composite state extend the SM in order to solve its issues in the Higgs sector. These theories postulate the existence of new interactions and fundamental particles, offering a rich and interesting phenomenology. A quantitative understanding of their dynamics is crucial in order to aid the direct search of new physics. Due to the non-perturbative nature of such interactions, analytical solutions are often not reliable. Nonetheless, numerical simulations can be used within the established framework of lattice gauge theories. Within this context, this work develops numerical and analytical tools towards a quantitative, non-perturbative understanding of composite Higgs models. The focus will be centred around two gauge theories, described respectively by the gauge groups $SU(4)$ and $Sp(4)$, with fermions transforming in multiple representations of the gauge group. The discussion will be articulated around the phenomenology of these theories, the strategies for simulating them on the lattice, and the development of techniques that allow to unfold their dynamics.

Lay Summary

The Standard Model (SM) of particle physics is the mathematical framework that describes three of the known fundamental forces: the electromagnetic, the weak and strong nuclear forces. No experiment has been capable of detecting solid deviations from its predictions, marking the astonishing success of the SM in predicting the natural phenomena that it aims to describe. It is well-established, however, that the SM cannot account for *any* observation: from the lack of an explanation for gravity to the lack of accountability of dark matter, many problems remain open. Among them, there is the puzzle of the Higgs boson mass, the so-called Naturalness problem.

The Higgs boson, discovered in 2012, was the last missing fundamental component to the SM. While its finding crystallised the success of the theory, the experimental value of its mass of approximatively $125GeV$ clashes with the number than a more 'natural' theory would provide. In order to justify the experimental value, in fact, the SM should engineer highly fine-tuned cancellations. This and other reasons pushed towards the idea that the observed Higgs might be not a fundamental but rather a light composite objects: a bridge between the SM and a new, more fundamental theory.

This work arises in this context, with the idea of establishing tools to explore and understand the vast landscape of composite models. Quantitative knowledge about the dynamics of composite Higgs theories is in fact crucial in order to understand whether they can be phenomenologically viable, and it can provide inputs for the direct search of new physics in particle colliders.

Declaration

I declare that this thesis was composed by myself, that the work contained herein is my own except where explicitly stated otherwise in the text, and that this work has not been submitted for any other degree or professional qualification except as specified.

Parts of this work have been published in [1, 2], the latter awaiting peer review. The generation of the gauge configurations, the computation of the observables and the analysis of [1] have been done by the author of this thesis. In [2], the development of the code has been done by the author of this thesis. The generation of the configurations and the analysis have been carried with the other authors.

(*Alessandro Lupo, July 2023*)

Acknowledgements

I offer my deepest gratitude to my supervisor, Luigi Del Debbio, for the opportunity to work with him on this project. His guidance and feedbacks have been truly valuable in shaping my attitude towards physics.

Not for the first time, nor for the last, my gratitude and affect to Nazario Tantalo.

I am truly thankful to Marco Panero for the enjoyable collaborations, and for the great amount of help I received from him during these years.

I warmly thank the group from Swansea for the enjoyable collaboration of the last years.

I was lucky enough to share the office with Raoul Hodgson and Nelson Lachini: this work is also built upon many, interesting discussions we had together.

Contents

List of Figures

List of Tables

Chapter 1

Gauge Theories

We refer to gauge theories as field theories with a Lagrangian that is invariant under transformations of a group of gauge symmetries, called "gauge group". The theory is specified by such group, together with field content transforming in some of its representations. A key aspect is that such transformations are taken to be local, i.e. they are functions of the spacetime coordinates. As we shall see, gauge invariance can be achieved by coupling the original field content to additional "gauge fields". Such a construction turns out to be relevant for the description of fundamental interactions.

1.1 General aspects

Let G be a semi-simple, compact connected Lie Group with elements denoted by g. A gauge transformation is a function that maps space-time points into elements of the group $x \mapsto g(x)$. The group G is referred to as "gauge group". Let ϕ be a collection of scalar fields transforming in the representation R of G

$$\phi_i(x) \mapsto U_R(g(x))_{ij}\, \phi_j(x) \equiv U_R(x)_{ij}\, \phi_j(x) \ , \qquad i = 1 \dots \dim_R \ , \tag{1.1}$$

where the sum over indices is understood. The matrices U associated to group elements connected to the identity can be represented in terms of the group generators in the representation R, T^a_R,

$$U_R(x) = \exp\left(i\omega^a(x)T^a_R\right) \ , \qquad a = 1 \dots \dim_G \ , \tag{1.2}$$

which form a Lie Algebra

$$[T^a, T^b] = if^{abc}T^c \ , \tag{1.3}$$

where f^{abc} are the structure constant of the group. Writing a Lagrangian density with a canonical kinetic term,

$$\mathcal{L}_{\text{kin}} = \partial_\mu \phi_i^\dagger \, \partial^\mu \phi_i \ , \tag{1.4}$$

results in a theory that is not invariant under gauge transformations. In order to make this term gauge-invariant, one can introduce a covariant derivative D_μ so that $D_\mu\phi$ transforms in the same representation as the field ϕ. This requires the introduction of a "gauge field" $A_\mu \equiv A^a_\mu T^a_R$ that transforms, under a gauge transformation, as

$$A_\mu(x) \mapsto U(x)A_\mu(x)U^\dagger(x) - iU(x)\partial_\mu U^\dagger(x) \ . \tag{1.5}$$

It is useful to write explicitly an infinitesimal gauge transformation

$$\phi_i \mapsto \phi_i + i\omega^a(T^a_R)_{ij}\phi_j \ , \tag{1.6}$$

$$A^a_\mu \mapsto A^a_\mu - f^{abc}\omega^b A^c_\mu - \partial_\mu \omega^a \ . \tag{1.7}$$

Regardless of the representation in which the fields ϕ are accommodated, the transformation of the gauge fields only depend on the structure constants. The covariant derivative can be then defined as

$$D_\mu\phi = \partial_\mu\phi + iA_\mu\phi \ , \tag{1.8}$$

which allows to write a gauge-invariant kinetic term for the ϕ fields, at the cost of introducing interaction terms between the ϕ and A_μ fields

$$\mathcal{L} = D_\mu\phi^\dagger D^\mu\phi \ . \tag{1.9}$$

A kinetic term for the gauge fields should be added. By defining the "field-strength" tensor $F_{\mu\nu}$,

$$F_{\mu\nu} \equiv i[D_\mu, D_\nu] = \partial_\mu A_\nu - \partial_\nu A_\mu + i[A_\mu, A_\nu] \,, \tag{1.10}$$

one can define the gauge invariant "Yang-Mills" kinetic term for the gauge fields

$$\mathrm{Tr}_G F_{\mu\nu} F^{\mu\nu} \,. \tag{1.11}$$

The field strength $F^a_{\mu\nu}$ transforms as

$$F^a_{\mu\nu} \mapsto U F^a_{\mu\nu} U^\dagger \,. \tag{1.12}$$

The full gauge-invariant Lagrangian density we obtain in this setup is then

$$\mathcal{L} = D_\mu \phi^\dagger D^\mu \phi - \frac{1}{4g^2} \mathrm{Tr}_G \left(F_{\mu\nu} F^{\mu\nu} \right) \tag{1.13}$$

The importance of gauge theories can be understood by looking at specific examples for the gauge group G, the field ϕ and the representation R to which they belong. Gauge theories, in fact, provide a framework to build models that describe the fundamental interactions between particles. To this end, it is useful to parametrise the equations from this Section in order to explicitly show the coupling between A_μ and ϕ, that we denote as g. This is done by simply rescaling $A_\mu \to g A_\mu$, i.e.

$$D_\mu = \partial_\mu + i g A^a_\mu T^a_R \,, \tag{1.14}$$

$$F_{\mu\nu} \equiv \frac{i}{g} [D_\mu, D_\nu] \tag{1.15}$$

$$F^a_{\mu\nu} = (\partial_\mu A_\nu - \partial_\nu A_\mu) + g f^{abc} A^b_\mu A^c_\nu \,, \tag{1.16}$$

$$\mathcal{L}_{\mathrm{Yang-Mills}} = -\frac{1}{4} \mathrm{Tr}_G \left(F_{\mu\nu} F^{\mu\nu} \right) \,. \tag{1.17}$$

The discussion is easily extended to spinors, where the kinetic term is modified to be $\bar{\psi} i \not{D} \psi$ instead of $\bar{\psi} i \not{\partial} \psi$. Mass terms for the scalar or fermionic fields are also easily added. It is important to notice, however, that the gauge fields are not allowed a mass term in the Lagrangian. This is because a mass term for spin 1 fields,

$$m^2 A_\mu A^\mu \,, \tag{1.18}$$

is not gauge invariant. In order to make contact with phenomenology, where certain gauge bosons are found to be massive, a mechanism to generate a mass for such particles while preserving gauge invariance must be provided. This will be briefly discusses in the context of the Standard Model.

Abelian Example: Electrodynamic Lagrangian

Abelian theories are described by an Abelian gauge group. An example that is already relevant for the description of natural phenomena is provided by the Lie Group $U(1)$ together with a massive Dirac field ψ transforming as $\psi \mapsto e^{i\alpha(x)}\psi$ and goes under the name of Electrodynamics. The Lagrangian density, according to the prescription of the previous Section, is

$$\begin{aligned} \mathcal{L} &= -\frac{1}{4}F_{\mu\nu}F^{\mu\nu} + \bar{\psi}\left(i\gamma_\mu D^\mu - m\right)\psi \\ &= -\frac{1}{4}F_{\mu\nu}F^{\mu\nu} + \bar{\psi}\left(i\gamma_\mu \partial^\mu - m\right)\psi - e\,\bar{\psi}\gamma_\mu\psi\, A_\mu \ . \end{aligned} \tag{1.19}$$

By identifying A^μ with the electromagnetic potential, so that the electric and magnetic fields are respectively $\vec{E} = -\vec{\partial}A^0 - \partial^0\vec{A}$ and $\vec{B} = \vec{\partial}\times\vec{A}$, the equation of motions for the field A_μ are the inhomogeneous Maxwell equations

$$\partial_\mu F^{\mu\nu} = J_\nu \ , \tag{1.20}$$

where $J^\mu = \bar{\psi}\gamma^\mu\psi \equiv (\rho, \vec{j})$ is the Noether current associated to the global $U(1)$ symmetry. The equation of motions for the ψ and $\bar{\psi}$ field are simply the Dirac equations coupled to the electromagnetic field. This gauge theory therefore describes the electromagnetic interactions between the electron field ψ, and the photon field A_μ. The parameter e appearing in the Lagrangian is related to the coupling of electromagnetism.

Non-Abelian Example: Chromodynamics Lagrangian

Chromodynamics describes the strong interaction between quarks and gluons. It is characterised by the gauge group $SU(3)$, corresponding to eight gauge bosons (gluons) and $N_f = 6$ flavors of Dirac fermions in the fundamental representation (quarks). The Lagrangian, according to the prescription given

above, is

$$\mathcal{L} = -\frac{1}{4}\sum_{a=1}^{N_c}\left(F^a_{\mu\nu}F^{\mu\nu}_a\right) + \sum_{f=1}^{N_f}\bar{\psi}_f\left(iD_\mu\gamma^\mu - m\right)\psi_f \ , \tag{1.21}$$

where

$$D_\mu = \partial_\mu + igA^a_\mu T^a \ . \tag{1.22}$$

1.2 Quantisation

More than one approach can lead to the quantisation of gauge theories. Here we adopt the path integral formalism, which is practical for the computations ahead. Since details are not propaedeutical for this work, and are easily found in the literature, this section only contains a sketch of the very delicate idea of quantisation. Consider a gauge group coupled, for simplicity, to a single fermionic field ψ. The quantum properties of the gauge theory are described by the partition function

$$\mathcal{Z} = \int \mathcal{D}A\,\mathcal{D}\bar{\psi}\,\mathcal{D}\psi\; e^{iS[A,\bar{\psi},\psi]+iS_{\text{gauge}-\text{fix}}[A,\bar{\psi},\psi]} \ , \tag{1.23}$$

where the action $S[A,\bar{\psi},\psi]$ is obtained from the space-time integration of the Lagrangian density of the theory. The gauge-fixing term, necessary in the continuum, removes the redundant degrees of freedom due to the gauge symmetry. The integration measure is intended as a sum over all possible field configurations. In this formalism, the expression for the evaluation of a correlation function is

$$\langle O[A,\bar{\psi},\psi]\rangle = \frac{1}{\mathcal{Z}}\int \mathcal{D}A\mathcal{D}\bar{\psi}\mathcal{D}\psi\, O[A,\bar{\psi},\psi]\, e^{iS[A,\bar{\psi},\psi]+iS_{\text{gauge}-\text{fix}}[A,\bar{\psi},\psi]} \ . \tag{1.24}$$

Upon quantisation, the fields are understood as distribution-valued operators $\hat{A},\hat{\bar{\psi}},\hat{\psi}$ acting on the Hilbert space of the states of the theory. The expectation value $\langle O\rangle$ of Eq. (1.24) corresponds to the vacuum expectation value of the time-ordered product $\langle 0|\mathcal{T}\hat{O}|0\rangle$.

1.3 Renormalisation

The quantities appearing in the (bare) Lagrangian of a quantum field theory are the result of a choice in parametrising the interactions. A bare Lagrangian can describe a universe with different physics depending on how the bare parameters are set up to match a certain condition. This can be, for instance, the matching of a physical observable computed in theory with its experimental value. This procedure is called renormalisation: matching the predictions obtained from a bare Lagrangian to the related physical quantities, allows the renormalised Lagrangian to describe a specific universe (our, if the matching is done to experimental quantities).

The first step of the renormalisation procedure is the addition of a regularisation, which introduces an ultraviolet (UV) cutoff Λ. An example is the lattice regularisation: by defining the theory on a lattice of spacing a, momentum's components are bounded by π/a in the UV. In addition, by working in a finite volume of size L, the lattice regularisation provides an additional IR cutoff, $2\pi/L$.

At fixed Λ, one then computes the quantity of interests and matches the theory prediction to related experimental values at a certain energy scale μ. For a gauge theory, typical bare parameters requiring a matching condition are the gauge coupling g (generally a set of) and the fermionic mass m (generally a set of). Let $C_\Lambda(g_0, m_0)$ be a correlation function of n fundamental fields, that is computed within the bare theory with UV cutoff Λ, and $C(g(\mu), m(\mu), \mu)$ the renormalised correlator obtained by matching at the scale μ. If the correlation function renormalises multiplicatively, the relation between the two can be expressed as

$$C(g(\mu), m(\mu), \mu) Z^n \left(g_0, \frac{m_0}{\Lambda}, \frac{\mu}{\Lambda}\right) = C_\Lambda(g_0, m_0) \ . \tag{1.25}$$

The independence of $C_\Lambda(g_0, m_0)$ from the renormalisation scale μ leads to the Callan-Symanzik equation

$$\left(\mu\frac{\partial}{\partial\mu} + \beta\frac{\partial}{\partial g} + \gamma_m m\frac{\partial}{\partial m} + n\gamma\right) C(g(\mu), m(\mu), \mu) = 0 \ , \tag{1.26}$$

where

$$\gamma\left(g, \frac{m}{\mu}\right) = \mu \frac{\partial \log Z}{\partial \mu} \tag{1.27}$$

$$\gamma_m\left(g, \frac{m}{\mu}\right) = \mu \frac{\partial \log m}{\partial \mu} \tag{1.28}$$

$$\beta\left(g, \frac{m}{\mu}\right) = \mu \frac{\partial g}{\partial \mu} \ . \tag{1.29}$$

These quantities encode the running of the parameter of the theory with the renormalisation scale. Of particular interest is the β function, dictating the running of the gauge couplings. Different β functions can in fact lead to gauge theories with drastically different phenomenologies, as we shall see in the next section.

1.4 UV and IR scenarios

The behaviour of the β function at different energy scales characterises very different types of gauge theories, which we examine in this section. Theories for which the coupling vanishes towards the UV are called asymptotically-free, a notable example being QCD. Asymptotic freedom can be understood by looking at the perturbative expansion of the β function. Consider a gauge theory with N_{R_i} active Dirac flavors of fermions in the representation R

$$\beta(g) = -b_1 \frac{g^3}{(4\pi)^2} - b_2 \frac{g^5}{(4\pi)^2} + O(g^7) \ , \tag{1.30}$$

with

$$\begin{aligned} b_1 &= \frac{11}{3} C_A - \frac{4}{3} N_{R_i} \lambda_R \ , \\ b_2 &= \frac{34}{3} C_A^2 - \frac{4}{3} (5 C_A + 3 C_R)\, \lambda_R\, N_{R_i} \ , \end{aligned} \tag{1.31}$$

where $C_{R/A}$ are the quadratic Casimirs of the representation R and the adjoint, while λ_R is the normalization of the trace of the generators of the representation R_i,

$$\mathrm{Tr}\left(T^a_{R_i}\, T^b_{R_i}\right) = \delta^{ab}\ \lambda_{R_i} \ . \tag{1.32}$$

Appendix A contains additional group-theoretical details. When the number of active flavors is such that

$$N_{R_i} < N_{\text{AF}} \equiv \frac{11 C_A}{4 \lambda_R} \,, \tag{1.33}$$

the leading term in the UV expansion of the β function, b_1, is positive. As a result, the β function has a trivial fixed-point at the origin, $\beta(0) = 0$, and the theory is free at high energy. When fermions in multiple representations are present, with n_i fermions in the representation R_i, the equations for the coefficients are easily modified

$$\begin{aligned} b_1 &= \frac{11}{3} C_A - \frac{4}{3} \sum_i \, N_{R_i} \, \lambda_{R_i} \,, \\ b_2 &= \frac{34}{3} C_A^2 - \frac{4}{3} \sum_i \, (5 C_A + 3 C_{R_i}) \, N_{R_i} \, \lambda_{R_i} \end{aligned} \tag{1.34}$$

In this work, we will only be interested in asymptotically free theories. The number of fermions is then bounded from above according to the previous equations. Moving towards the IR, a number of scenarios can occur (cf. Fig 1.1).

- The theory confines: as the coupling g or equivalently $\alpha = g^2/(4\pi)$ increases, a critical value α_{cr} can be reached at which the fermions condensate, spontaneously breaking the flavor symmetry of the UV theory. In this case, one can expect a set of Nambu Goldstone bosons (NGB) lighter than the other states in the IR theory. In the small mass and energy regime, predictions from chiral perturbation theory (ChPT) are expected to be verified [20–23]. QCD is an example of such a scenario, and one of the models that we analyse in this work falls into the same category.

- The theory is IR conformal: approaching the IR, the coupling may reach a fixed point α_{IR} at which the coupling stops running. As a consequence, the critical value at which the fermions condensate is not reached. ChPT is not suitable to describe such a behaviour, which rather abides scaling relations such as the ones described in [24–28].

- The theory confines, but has a near-conformal dynamics. In addition to the light pNGB due to the breaking of the flavor symmetry, which still become massless at the chiral point, an additional scalar state, the

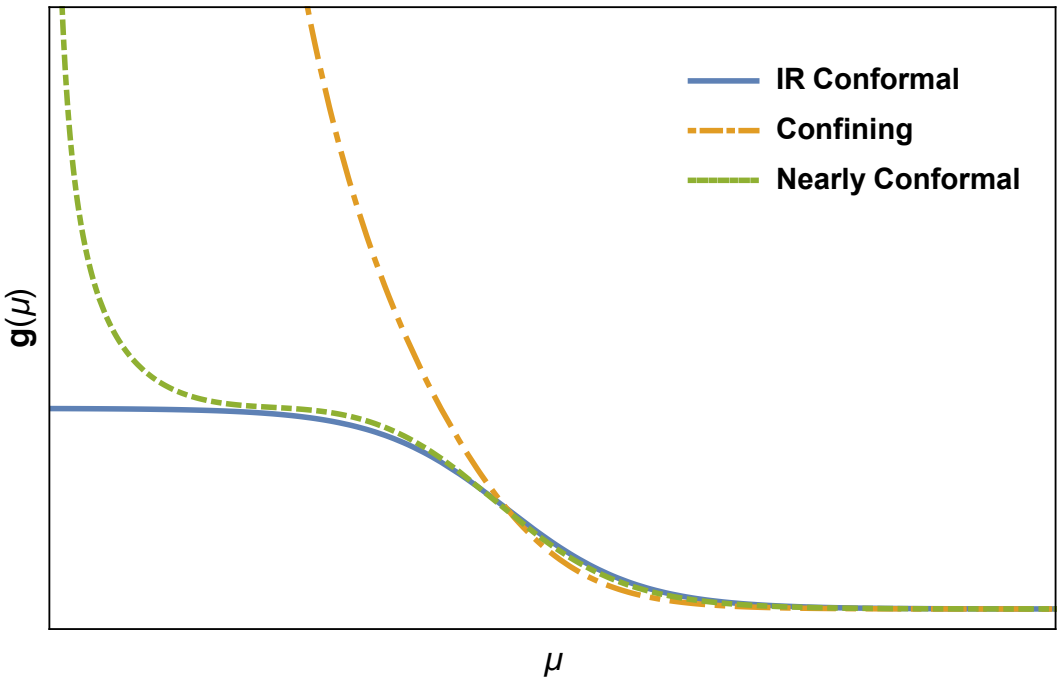

Figure 1.1 *Varieties of IR behaviours for the running coupling g with the energy scale μ. The continuous line corresponds to an IR conformal scenario: the coupling stops running approaching the IR, and the theory exhibits scale invariance. The dashed-dotted line correspond to a confining theory: a scale is dynamically generated, precluding conformality. The dotted line corresponds to a nearly conformal scenario: the theory is still confining, but scale invariance is approximately realised.*

dilaton, is found to be light compared to the rest of the spectrum. Such particle, interpreted as a Goldstone boson (GB) due to the breaking of scale invariance, is described in the IR by dilaton effective field theory [29–35].

It should be stressed that while the upper bound for asymptotic freedom can be determined perturbatively, both $\alpha_{\rm cr}$ and $\alpha_{\rm IR}$ can be large, so that perturbative predictions are affected by uncontrolled systematics. One therefore has to turn towards other tools. While effective theories allow for a non-perturbative description of the IR, lattice simulations provide a well-established way of performing full non-perturbative studies of these models. This is partially the context in which this work arises, and lattice results will find extensive space in the next chapters. Despite analytical predictions not being reliable, perturbation theory is still useful to introduce the concept of the conformal window.

1.4.1 Conformal Window

The search for the conformal window corresponds to finding an IR fixed-point that is not trivial, i.e. not at zero coupling, so that the theory is still interacting. Following the seminal work of Banks and Zaks [36], we consider a situation in which the 2-loop coefficient of the perturbative expansion of the β function,

$$b_2 = \frac{34}{3} C_A^2 - \frac{4}{3} \sum_i \left(5C_A + 3C_{R_i}\right) N_{R_i} \lambda_{R_i} \ , \tag{1.35}$$

is negative. Then there can be a value of b_1 such that the two-loop β function vanished. This is referred to as a Banks-Zaks (BZ) fixed point,

$$\alpha_{\rm IR} \simeq \alpha_{\rm BZ} = -\frac{4\pi b_1}{b_2} \ll 1 \ . \tag{1.36}$$

This perturbative consideration suggests that, at small coupling, there can be a number of fermions low enough to guarantee asymptotic freedom, yet large enough that $b_1 \ll 1$. As $\alpha_{\rm BZ}$ increases, non-perturbative effects greatly complicate the estimate of the lower bound for the conformal window. This can be understood, at fixed number of colors N_c, by decreasing the number of fermions. The negative coefficient b_2 becomes smaller in magnitude, while b_1 remains positive. The value $\alpha_{\rm BZ}$ consequently grows larger until the two-loop result looses predictive power.

1.5 Flavor Symmetry and Breaking Patterns

In this section, we analyse symmetry breaking patterns of chiral symmetry that are relevant for this work. A treatment of this problem is found e.g. in Ref. [37]. Consider a gauge theory coupled to N massless Dirac fermions, or equivalently $2N$ two-component spinors, in the representation R of the gauge group. Due to the lack of the mass term, which would mix different chiralities, the fermionic sector exhibits, classically, the global symmetry $SU(N)_L \times SU(N)_R \times U(1) \times U(1)$. Accounting for the Adler-Bell-Jackiw anomaly, we identify the flavour symmetry group

$$SU(N)_L \times SU(N)_R \times U(1) \ . \tag{1.37}$$

We are interested in understanding what subgroup H is left unbroken when such symmetry is broken, either spontaneously or explicitly. The former

case arises when the bilinear operator acquires dynamically a non-vanishing vacuum expectation value (VEV). Different situations can arise depending on the representation of the gauge group in which the fermions are accommodated. The fermionic bilinear acquiring a VEV can be written as

$$\langle \bar{\psi}_{\bar{R}}\, \psi_R \rangle \ , \tag{1.38}$$

in terms of Dirac spinors ψ_R, where $\bar{R}$ is the conjugate representation of R. For the purpose of this Section, such term can be expressed in terms of two-component left-handed spinors χ

$$\langle \epsilon_{\alpha\beta} \chi_R^{\alpha} \chi_{\bar{R}}^{\beta} \rangle \ , \tag{1.39}$$

where α, β are spinor indices, and ϵ is the antisymmetric Levi-Civita tensor.

- If the representation R is complex, R and $\bar{R}$ are distinct representations, Eq. (1.39) is invariant under $H = SU(N)$ transformations. The symmetry breaking patterns is then

$$SU(N)_L \times SU(N)_R \longrightarrow SU(N)_V \ . \tag{1.40}$$

- If the representation R is real, the conjugate representation $\bar{R}$ is related to R by a similarity transformation which involves a symmetric form δ_{ab}, a, b being color indices. The condensate

$$\langle \epsilon_{\alpha\beta} \chi_R^{\alpha} \chi_{\bar{R}}^{\beta} \rangle = \langle \epsilon_{\alpha\beta} (\chi_R^{\alpha})_a \delta^{ab} (\chi_R^{\beta})_b \rangle \ , \tag{1.41}$$

  is invariant under $H = SO(2N)$. The symmetry breaking pattern is

$$SU(2N) \longrightarrow SO(2N) \ , \tag{1.42}$$

  which generated $2N^2 + N - 1$ Goldstone bosons.

- If the representation R is pseudoreal, the conjugate representation $\bar{R}$ is related to R by a similarity transformation which involves an antisymmetric form $\Omega_{ab} = -\Omega_{ba}$, a, b being color indices. The condensate

$$\langle \epsilon_{\alpha\beta} \chi_R^{\alpha} \chi_{\bar{R}}^{\beta} \rangle = \langle \epsilon_{\alpha\beta} (\chi_R^{\alpha})_a \Omega^{ab} (\chi_R^{\beta})_b \rangle \ , \tag{1.43}$$

is invariant under $H = Sp(2N)$. The symmetry breaking pattern is

$$SU(2N) \longrightarrow Sp(2N) \ , \tag{1.44}$$

which generated $2N^2-N-1$ Goldstone bosons. Details about the various groups are found in Appendix A.

1.6 The Standard Model

The Standard Model is a gauge theory coupled to both fermionic and scalar fields. It is associated with the gauge group

$$G_{\rm SM} = SU(3) \times SU(2)_L \times U(1) \ , \tag{1.45}$$

modulo subgroups that act trivially on all fields. The $SU(3)$ part taken in isolation is known as Quantum Chromodynamics (QCD). Similarly, the $SU(2)_L \times U(1)$ sector is called Electro-Weak (EW). The total amount of gauge bosons is $8 + 3 + 1$. These are coupled to fermionic fields in various representations $(R_{SU(3)}, R_{SU(2)_L}, Y)$ of $G_{\rm SM}$, where $R_{SU(3)}$ and $R_{SU(2)_L}$ denote the representations of the individual subgroups, and Y is the charge under the $U(1)$, referred to as "hypercharge". The Higgs boson, whose coupling with the other fields determine the masses of certain combinations of fermionic and bosonic degrees of freedom, is also coupled to $SU(2)_L \times U(1)$. The fermions appear in three "generations" that are identical, apart from their couplings to the Higgs. The first generation, written in terms of Weyl spinors and classified by the representation of $G_{\rm SM}$, is the following

- Leptons: electric neutrino and left-handed electron, $E = (\nu_e, e_L) \in (\mathbf{1}, \mathbf{2}, -1/2)$. Right-handed electron $e_R \in (\mathbf{1}, \mathbf{1}, -1)$.
- Quarks: left-handed up and down quarks, $Q = (u_L, d_L) \in (\mathbf{3}, \mathbf{2}, 1/6)$. Right-handed up quark $u_R \in (\mathbf{3}, \mathbf{1}, 2/3)$. Right-handed down quark $d_R \in (\mathbf{3}, \mathbf{1}, -1/3)$.

The heavier generations of leptons consist of the muon and the tau, and their respective neutrinos. The heavier generations of quarks consist of strange (s) and charm (c), bottom (b) and top (t). (c, s) and (t, b) form $SU(2)$ doublets similarly to (u, d). The Higgs field is

- $H \in (\mathbf{1}, \mathbf{2}, 1/2)$.

The Higgs field is self-interacting, with a potential

$$V(\phi) = \mu^2 \phi^\dagger \phi - \lambda (\phi^\dagger \phi)^2 \ , \tag{1.46}$$

and it is coupled to the fermions à la Yukawa

$$\mathcal{L}_{H-\text{Quark}} = -\lambda_d \bar{Q} \phi d_R - \lambda_u \bar{u}_L (i\sigma_2 \phi^*) Q \phi + h.c. \ , \tag{1.47}$$

where σ_2 is the second Pauli matrices with $SU(2)_L$ indices.

$$\mathcal{L}_{H-\text{Leptons}} = -\lambda_e \bar{E} \phi e_R + h.c. \tag{1.48}$$

Similar terms describe the other two generations. Once the Higgs acquires a VEV, $\langle \phi \rangle = (0, v/\sqrt{2})$, mass terms are generated for the fermionic degrees of freedom arranged into Dirac fermions, e.g. $m_e(\bar{e}_L e_R + \bar{e}_R e_L)$. The interactions are engineered such that, in the SM, neutrinos are massless. The spontaneous symmetry breaking of the EW symmetry, triggered by the VEV of the Higgs, leaves invariant the $U(1)$ symmetry responsible for electromagnetism. The relation between quantum numbers is $Q = Y + t_3$, where Q is the electromagnetic charge, Y the hypercharge, and t_3 is the eigenvalue of $\sigma_3/2$, the third generator of $SU(2)_L$.

Chapter 2

A composite Higgs

Attempting to explain certain limitations of the SM leads to the idea that the Higgs could be a composite state. While this intuition can find many realisations, this work focuses on a pNGB interpretation of the Higgs particle. This Chapter is structured as follows. Section 2.1 introduces the Naturalness problem of the SM, together with the idea of composite Higgs. The example of QCD, one of the best-known composite theories, is also reviewed. Section 2.2 introduces, following [19], the gauge theories that give rise, in the IR, to a composite Higgs. Among these we describe, in Sections 2.3 and 2.4, a promising candidate that will be the focus of the lattice studies in the next chapters. The last Section, 2.5, describes theories based on the gauge group $Sp(2N)$, whose physical properties are relevant for composite Higgs models and the study of the conformal window. Part of the content of this Chapter is contained in Refs [1, 2].

2.1 Naturalness, Nambu-Goldstone Higgs and the example of QCD

The Standard Model (SM) of particle physics describes the strong and electroweak (EW) interactions with remarkable accuracy, and no clear deviation from its predictions has been observed. There are however open problems pointing towards the idea that the SM effectively describes Nature only up to a cutoff energy scale Λ_{SM} located at least in the TeV range. One of these issues, known as "Naturalness problem", lies in the Higgs sector, where quantum corrections are expected to push the mass of the Higgs boson towards Λ_{SM}. The experimental value of approximatively 125 GeV [38, 39], however, lies well within the EW range. This value could only be understood within the SM by relying on fine-tuned cancellations [40], which are considered unsatisfactory from a theoretical perspective. The solutions that have been proposed to tackle this fine-tuning issue have been generating a vast and fertile literature, including ideas such as supersymmetry and technicolor. Another popular solution, and focus of this work, is the "composite Higgs" scenario, where the Higgs boson's mass is explained in terms of Goldstone dynamics [41]. In this scenario, a gauge theory is postulated to describe a new strongly-interacting sector and its dynamics. Depending on the fermionic content of the theory, a global flavor symmetry is realised: if the fermions condensate, the spontaneous breaking of such symmetry generates Goldstone bosons, among which there would be the Higgs doublet. At this stage, with the new sector in isolation, the Higgs would be massless. The couplings to the SM are supposed to break such symmetry explicitly. As a consequence, the Higgs is a pseudo NGB: its mass is non-zero, but still (comparatively) small due to the presence of an approximate symmetry that is only broken by the coupling between the new sector and the SM. This machinery is already present in the SM. QCD is, in fact, a composite theory whose spectrum exhibits a lighter state, the pion, as shown in Figure 2.1. The light mass of the pion can be understood with the same mechanism described above, which we now work out for the example of QCD, along the lines of Section 1.5.

Consider two-flavor QCD, the approximation of QCD where only the lightest quarks, the Dirac fermions u and d, are present. In the chiral limit, in which

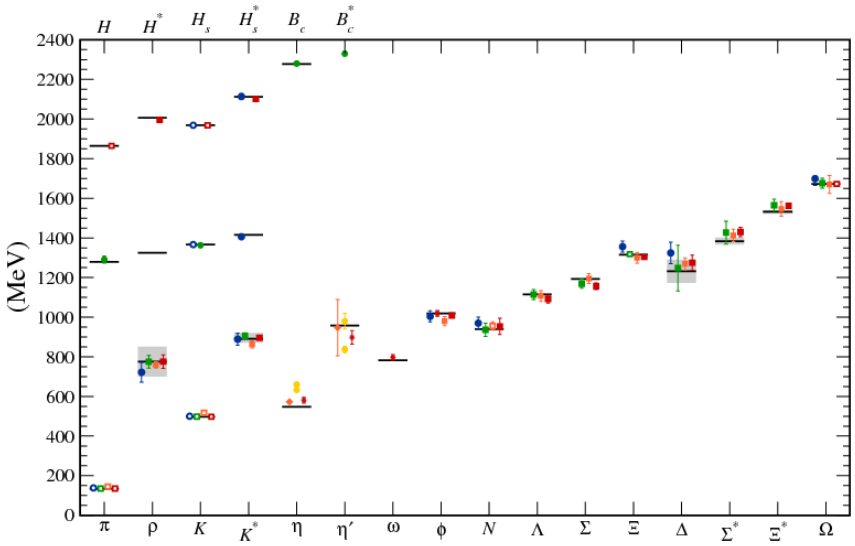

Figure 2.1 *A summary of lattice (points) and experimental (lines) results for the QCD spectrum taken from Ref. [3]. Different shapes correspond to different discretisation of the QCD action, while different colours correspond to increasing numbers of ensembles. b-flavored mesons are shifted down by 4000 MeV. See Ref. [3] and references therein for further details.*

the masses of these quarks are zero, the chiralities are decoupled

$$u_{L/R} = \frac{1 \pm \gamma_5}{2} u \ , \quad d_{L/R} = \frac{1 \pm \gamma_5}{2} u \ , \tag{2.1}$$

$$\mathcal{L} = i\bar{u}_L \not{\partial} u_L + i\bar{u}_R \not{\partial} u_R + i\bar{d}_L \not{\partial} u_L + i\bar{d}_R \not{\partial} u_R = i\bar{\psi}_L \not{\partial} \psi_L + i\bar{\psi}_R \not{\partial} \psi_R \ , \tag{2.2}$$

where, motivated by the symmetry between u and d, the two quarks have been grouped in the doublets $\psi_{L/R} = (u_{L/R}, d_{L/R})$. It is manifest that the chiral limit of two-flavor QCD has a global $SU(2)_L \times SU(2)_R$ symmetry which rotates independently the two chiralities

$$\psi_{L/R} \mapsto \exp(i\omega^a_{L/R} T^a)\psi_{L/R} \ , \qquad a = 1, 2, 3 \ , \tag{2.3}$$

where T^a are $SU(2)$ generators in the fundamental representation. Equivalently, on $\psi = \psi_L + \psi_R$

$$\psi \mapsto \exp(i\omega^a_V T^a)\psi \ , \qquad \psi \mapsto \exp(i\gamma_5 \omega^a_A T^a)\psi \ , \tag{2.4}$$

with $\omega_V = (\omega_L + \omega_R)/2$, $\omega_A = (\omega_L - \omega_R)/2$. The Noether currents associated

to these symmetry transformations are

$$J^a_{V\,\mu} = \bar{\psi}\gamma_\mu T^a \psi \ , \qquad J^a_{A\,\mu} = \bar{\psi}\gamma_\mu\gamma_5 T^a \psi \tag{2.5}$$

As pointed out in Section 1.5, when the fermions condensate, a VEV for the fermionic bilinear breaks the symmetry by mixing chiralities,

$$\langle \bar{\psi}_L \psi_R \rangle + h.c. \ , . \tag{2.6}$$

The broken group depends on the representation of the fermion, and in this case ψ belongs to the fundamental representation of $SU(2)$, which is pseudoreal. The invariant subgroup is then $Sp(2) = SU(2)_V$. According to the Goldstone theorem, a Goldstone boson appears in the spectrum for each broken generator. The annihilation operators for such states are given by the currents

$$J^a_{A,0}(x) = \bar{\psi}(x)\gamma_0\gamma_5\tau^a\psi(x) \ , \tag{2.7}$$

By using $\psi = (u\, d)^T$ we can write the three NGB operators

$$\begin{aligned} J^1_{A,0} \equiv \pi_1 &= \frac{1}{\sqrt{2}}\left(\bar{u}\gamma_0\gamma_5 d + \bar{d}\gamma_0\gamma_5 u\right) \ , \\ J^2_{A,0} \equiv \pi_2 &= \frac{1}{\sqrt{2}}\left(-i\bar{u}\gamma_0\gamma_5 d + i\bar{d}\gamma_0\gamma_5 u\right) \ , \\ J^3_{A,0} \equiv \pi_3 &= \frac{1}{\sqrt{2}}\left(\bar{u}\gamma_0\gamma_5 u - \bar{d}\gamma_0\gamma_5 d\right) \ . \end{aligned} \tag{2.8}$$

Since there is a leftover $SU(2)$ symmetry, called isospin, it is useful to express the NGB degrees of freedom in terms of the eigenvalues $+1, 0, -1$ of the third generator of isospin, T^3,

$$\pi_+ = \frac{\pi_1 + i\pi_2}{\sqrt{2}} \ , \qquad \pi_- = \frac{-\pi_1 + i\pi_2}{\sqrt{2}} \ , \qquad \pi_0 = -\pi_3 \ . \tag{2.9}$$

Away of the chiral limit, the u and d quark are massive, but light compared to the hadronic scale $\Lambda_{\rm QCD}$. The $SU(2)_L \times SU(2)_R$ symmetry is indeed broken explicitly, but softly. It is therefore reasonable to still expect the pions to behave as approximate NGB. Within this framework, the light value of the pion's masses are explained. In real life, the remaining isospin $SU(2)_V$ symmetry is also broken by the mass difference between u and d and by electromagnetism. These effects, however, are only important if the theory is supposed to provide predictions at the subpercent level.

The idea behind pNGB Higgs models stems from the speculation that the Higgs boson is the lightest composite state of a strongly interacting sector, and its mass is protected by an approximate symmetry, similarly to how the pions are the lightest states of QCD.

2.2 UV completions for composite Higgs models

In this Section we analyse the gauge theories that can give rise to a pNGB Higgs. Indeed, on top of the existence of a light composite state in the IR, a number of other features can be required to discern between viable theories. An important step forward in this direction was made in Ref. [19], where possible UV completions for a composite Higgs scenario have been analysed, based on symmetry arguments and phenomenological requirements. In this Section, we review such a classification, in order to clarify the choices made in this work.

Following Ref [19], we consider a gauge theory $\mathcal{G}$ which describes the new strongly-interacting sector, coupled to fermions transforming in arbitrary representations of $\mathcal{G}$. We denote by H the group left unbroken after the fermions condensate. It is sensible, both from the point of view of phenomenology and for the sake of simplicity, to ask the following requirements.

2.2.1 Model requirements

Asymptotic freedom

We require the theory to be confining. Since this generally happens for asymptotically free theories, we constrain the numbers of fermions to satisfy the bound provided in Section 1.4, which ensures asymptotic freedom.

Minimality

We limit our attention to simple Lie Groups for $\mathcal{G}$. While more complicated scenarios can be considered, the characteristic features of composite theories are already appreciated at this level. In order to account for the matter content coupled to $\mathcal{G}$ we consider, this time without loss of generality, left-handed Weyl fermions only: n_i of them in the representation R_i, with $i = 1, \dots p$. We already appreciate a great simplification in the model landscape, since the corresponding symmetry G without chiral anomaly is

$$G = SU(n_1) \times SU(n_2) \times \dots SU(n_p) \times U(1)^{p-1} \ . \tag{2.10}$$

QCD at the chiral limit falls into this example. As discussed in Section 1.5, assuming that the symmetry is broken spontaneously[1], the unbroken group H will depend on the representations R_i.

Custodial $SU(2)$ Symmetry

In the SM, the W and Z-bosons masses are related to the gauge charges by a residual "custodial" $SU(2)$ symmetry that survives in the Higgs sector after EW symmetry breaking. A parametrisation of its effect is given by the ρ parameter,

$$\rho = \frac{m_W^2}{m_Z^2 \cos^2 \theta_{\rm W}} \ , \tag{2.11}$$

where $\theta_{\rm W}$ is the Weinberg angle. In the SM, $\rho_{\rm SM} = 1$ at tree-level, and the custodial $SU(2)$ prevents large loop corrections. Since the experimental value [42]of ρ is approximatively 1, care is required while extending the SM to theories with a larger field content, in order to ensure that the custodial $SU(2)$ justifying $\rho \simeq 1$ is still present. A "safe" symmetry breaking pattern, in this regard, should therefore lead to an invariant subgroup H that not only contains $G_{\rm SM}$ (which would then be gauged), but an addition custodial $SU(2)_R$

$$G \longrightarrow H \supset G_{\rm cust.} \supset G_{\rm SM} \ , \tag{2.12}$$

$$G_{\rm cust.} = SU(3) \times SU(2)_L \times SU(2)_R \times U(1)_X \ . \tag{2.13}$$

[1] As long as we account for the new sector in isolation, as pointed out before.

One of the NGB is to transform into the $(\mathbf{1}, \mathbf{2}, \mathbf{2}, 0)$ of $G_{\text{cust.}}$ in order to reproduce the Higgs.

Top partial compositeness

While not a strict requirement, it is tempting to chase models that yield a composite state with the same SM quantum numbers as the heavy quarks. This property could clarify the hierarchical structure of the quark masses: if the composite partner of the top quark has a large enough anomalous dimension, the mass hierarchy arises naturally. This idea goes under the name of partial compositeness [43] and it has been the subject of several lattice studies in recent years [1, 10, 13, 16, 44–50]. We briefly recall the idea. For a review on the topic, we refer to e.g. Ref. [40].

Let Λ_{UV} be a high scale and Λ_{HC} the dynamically generated scale of the new sector. In the effective field theory formalism, the coupling between the SM fermions and composite states, at the high scale Λ_{UV}, is parametrised by

$$\mathcal{L} = \frac{\lambda_{t_L}}{\Lambda_{UV}^{d_L-5/2}} \bar{q}_L \mathcal{O}^L + \frac{\lambda_{t_R}}{\Lambda_{UV}^{d_R-5/2}} \bar{q}_R \mathcal{O}^R + \dots \tag{2.14}$$

for fermionic operators $\mathcal{O}^{L/R}$, with similar terms for each quark. The emergence of Yukawa interactions is determined by the couplings $\lambda_{t_{L/R}}$. At lower energy, assuming $d_{L/R} > 5/2$ [40], these couplings evolve to

$$\lambda_{t_{L/R}}[\Lambda_{HC}] \simeq \lambda_{t_{L/R}} \left(\frac{\Lambda_{HC}}{\Lambda_{UV}} \right)^{d_{L/R}-5/2} . \tag{2.15}$$

If only the dimension of the heavy quark partners, in particular the top, are close 5/2, even with a large separation between $\Lambda_{UV}/\Lambda_{HC}$, a large Yukawa coupling is possible for the heavy quarks. This mechanism could explain the fermionic hierarchy.

2.2.2 Allowed models

In Ref. [19] these constraints are extensively analysed. The solutions are shown in Tables 2.1 and 2.2 for $p = 2$ and $p = 3$ fermionic representations, respectively. These constitute a pool of reasonable models for the composite

Higgs scenario. In order to further understand the phenomenological viability of these theories, their non-perturbative dynamics has to be probed. Lattice gauge theories are a strong option for this task. From the point of view of lattice simulations, these models certainly pose many challenges. State-of-the-art lattice simulations contain up to four dynamical flavors [51] and probing the models with the large flavor content described in Tables 2.1 and 2.2 can be difficult. On the other hand, simplified models with reduced flavor content can provide first insights on the non-perturbative dynamics of multi-representation theories, at a reduced computational cost. Another challenge is posed by the very high dimensionality of many of the gauge groups appearing in Tables 2.1 and 2.2, which are unrealistic for modern HPC architectures. Finally, while the simulation of $SU(3)$ with fundamental fermions are well-established, numerical simulations of different gauge groups, and in particular with multiple and/or higher representations are still developing [1, 13, 16, 44–50, 52–54].

As in Ref. [19], we notice that two cases arise due to the low dimensionality of the gauge group. One is $SU(4)$ with three (anti)fundamental fermions and five two-index antisymmetric (2AS) fermions. The other is $Sp(4)$ with four fundamental and six 2AS flavors. The former will be the subject of the lattice investigation of Chapter 4. One of the objectives of this work is to set a framework that allows to efficiently investigate composite Higgs models on the lattice. For this reason, we developed new code within the lattice software Grid [55] that allows simulations of $Sp(2N)$: this will be discussed in Chapters 3 and 5. As a result Grid allows, with a single source-code, to perform simulations of both SU and Sp gauge theories, with arbitrary numbers of colors, and different fermionic representations (adjoint, two-indices and fundamental). A great advantage of Grid lies in its portability across many CPU and GPU architectures, which can be then exploited for numerical studies of composite Higgs at the cost of maintaining a single source-code.

$\mathcal{G}$	$n_1\, R_1$	$n_2\, R_2$	Constraints
$Sp(2N)$	5 Adj	6 F	$2N \geq 12$
$Sp(2N)$	5 2AS	6 F	$2N \geq 4$
$Sp(2N)$	4 F	6 2AS	$2N \leq 36$
$SO(N)$	5 2S	6 F	$N \geq 55$
$SO(N)$	5 Adj	6 F	$N \geq 15$
$SO(N)$	5 F	6 Spin	$N = 7, 9, 10, 11, 13, 14$
$SO(N)$	5 Spin	6 F	$N = 7,\ 9$
$SO(N)$	4 Spin	6 F	$N = 11,\ 13$

Table 2.1 *Table from Ref. [19] containing the gauge theories with two representations that are compatible with the requirements listed in this section.*

$\mathcal{G}$	$n_1\, R_1$	$n_2\, R_2$	R_3	Constraints
$SU(N)$	5 2AS	3 F	3 F*	$N = 4$
$SO(N)$	5 F	3 Spin	3 Spin$'$	$N = 8, 10, 12, 14$

Table 2.2 *Table from Ref. [19] containing the gauge theories with three representations that are compatible with the requirements listed in this section.*

2.3 Ferretti Model

We briefly recall the features of the model introduced by Ferretti in Ref. [56] following the conventions of Ref. [13]. Its UV completion is described by the gauge group $\mathcal{G} = SU(4)$. The gauge field is coupled to three Dirac fermions that we express in terms of Weyl doublets χ^a_m, $\bar{\chi}^a_m$ respectively in the fundamental and antifundamental representation of the gauge group, together with five Majorana fermions ψ^I_{mn} in the 2AS representation, which is real and dimension 6. The indices $a = 1, 2, 3$ and $I = 1, \ldots 5$ are flavor indices, while $m, n = 1, 2, 3, 4$ denote the color. This matter content induces a global symmetry described by the group G

$$G = SU(5) \times SU(3) \times SU(3)' \times U(1)_X \times U(1)' \,. \tag{2.16}$$

The charges of the fermions with respect to the flavor group are described in Table 2.3. Neglecting couplings with the SM fermions, G is an exact symmetry. Spontaneous symmetry breaking happens once the bilinears for both representations acquire a non-vanishing expectation value, leaving the unbroken subgroup H. The quotient group determining the low-energy

	$SU(5)$	$SU(3)$	$SU(3)'$	$U(1)_X$	$U(1)'$
ψ	**5**	**1**	**1**	0	-1
χ	**1**	**3**	**1**	-1/3	5/3
$\tilde{\chi}$	**1**	**1**	$\bar{\mathbf{3}}$	1/3	5/3

Table 2.3 *Flavor charges of the fermions in the Ferretti model.*

dynamics is

$$\frac{G}{H} = \frac{SU(5) \times SU(3) \times SU(3)' \times U(1)_X \times U(1)'}{SO(5) \times SU(3)_c \times U(1)_X} \,. \tag{2.17}$$

This symmetry breaking pattern is interesting for several reasons. Given that $SO(5) \supset SU(2) \times SU(2)$, the pattern is compatible with the requirement of custodial symmetry $H \supset G_{\text{cust}} \supset G_{\text{SM}}$, with $G_{\text{cust}} = SU(3)_c \times SU(2)_L \times SU(2)_R \times U(1)_X$ and G_{SM} being the SM gauge group $SU(3)_c \times SU(2)_L \times U(1)_Y$. The unbroken group $SU(3)_c$, related to the fundamental sector, is responsible for the strong interaction of QCD once it is gauged. The unbroken group related to the 2AS fermions, $SO(5)$, contains the EW group $SU(2)_L \times U(1)_Y$. In fact, $SO(5) \supset SO(4) \simeq SU(2)_L \times SU(2)_R$. We then define an $U(1)_R$ as the subgroup of $SU(2)_R$ generated by the generator of isospin rotation $T_R^{(3)}$: the correct hypercharges Y are then obtained by $Y = T_R^{(3)} + X$, X being the charge under $U(1)_X$. The quotient $SU(5)/SO(5)$ is therefore the relevant one for EW symmetry breaking: by writing its 14 Goldstone bosons in terms of SM charges,

$$\mathbf{14} \to \mathbf{1}_0 + \mathbf{2}_{\pm 1/2} + \mathbf{3}_0 \pm \mathbf{3}_{\pm 1} \equiv (\eta, h, \phi_0, \phi_\pm) \,, \tag{2.18}$$

we identify an $SU(2)$ doublet $\mathbf{2}_{\pm 1/2}$, h, that is compatible with the Higgs boson.

Turning to the composite partner for the top quark, this is introduced as a Dirac fermion Ψ [56] in the low energy theory that has charges $(\mathbf{5}, \mathbf{3})_{2/3}$ with respect to the unbroken subgroup H. States with these quantum numbers, relevant for partial compositeness, are obtained in this theory by color singlet combinations of fermions in different representations. Such baryonic content is typical of theories with multi-representation matter.

2.4 Two-flavor Ferretti Model

In this work we will focus on a simplified version of the Ferretti model, which allows to explore the dynamics of multiple representation theories at a reasonable computational cost. We will consider two Dirac fermions in the fundamental and two Dirac fermions in the 2AS representation of the gauge group $SU(4)$, a model that has been already studied in [13, 48–50]. While retaining the multi-representation dynamics and some non-perturbative features, this choice changes the global symmetries of the theory, thar we now review.

It is important to understand the discrete symmetries of each sector in order to give the correct interpretation to the lattice data. Isospin, in particular, is useful in classifying scattering processes. The isospin group in the fundamental sector is the well known $SU(2)$. The symmetry breaking pattern is the same as in massless two-flavor QCD, characterised by the quotient group

$$\frac{SU(2)_{\mathrm{L}} \times SU(2)_{\mathrm{R}}}{SU(2)_{\mathrm{V}}} \ , \tag{2.19}$$

which has been discussed in Section 2.1. For completeness, we only mention that the three Goldstone bosons π_1, π_2, π_3 arising from these cosets can be labelled with eigenvalues of the azimuthal component of the isospin, $\pm 1, 0$:

$$\begin{aligned} \pi_+ &= \frac{\pi_1 + i\pi_2}{\sqrt{2}} \ , \\ \pi_- &= \frac{-\pi_1 + i\pi_2}{\sqrt{2}} \ , \\ \pi_0 &= -\pi_3 \ . \end{aligned} \tag{2.20}$$

The multiplet (π_+, π_0, π_-) has eigenvalue -1 under the G-parity defined by combining charge conjugation $\mathcal{C}$ with an SU(2)-isospin rotation,

$$G = \exp\left(i\pi\tau_2\right) \ \mathcal{C} \ , \tag{2.21}$$

τ_i being $SU(2)$ generators. In the 2AS sector, instead, the symmetry breaking pattern yields the cosets

$$\frac{SU(4)}{SO(4)} \ . \tag{2.22}$$

Let T_A be the generators of $SU(4)$, with $A = 1 \dots 15$, which can be found

in A. Let $\hat{T}_{\hat{a}}$ be the broken generators, with $\hat{a} = 1 \dots 9$ and T_a the remaining unbroken generators, with $a = 1 \dots 6$. These cosets are characterised by 9 Goldstone bosons $\Pi_{\hat{a}}$, $\hat{a} = 1 \dots 9$, that we represent exponentially as

$$U = \exp(i\hat{T}_{\hat{a}}\Pi_{\hat{a}}) \ , \tag{2.23}$$

We wish to infer how the multiplet Π transforms under an isospin, $SO(4)$ transformation. The field U transforms as

$$U \to hUh^\dagger \ , \qquad h = \exp(i\omega_a T_a) \ , \qquad a = 1 \dots 6 \ . \tag{2.24}$$

By considering an infinitesimal transformation of this type, we infer that the transformation of Π is generated by

$$(X^a)_{\hat{b}\hat{c}} = -if_{a\hat{b}\hat{c}} \ . \tag{2.25}$$

X^a are the unbroken generators of $SU(4)$ generating $SO(4)$, represented as 9×9 matrices. This is the two-index antisymmetric representation of $SO(4)$, for which explicit expressions for the generators are given in Appendix A.3. The maximum set of commuting generators here is two, therefore we choose to diagonalise X_1 and X_6. The Goldstone bosons in the isospin basis can be then labelled as Π_{a_1,a_6}, where a_n are eigenvalues of the generators X_n

$$\begin{aligned}
\Pi_{-1,0} &= -i\Pi_1 + \Pi_2 \ , \\
\Pi_{1,0} &= i\Pi_1 + \Pi_2 \ , \\
\Pi_{-\frac{1}{2},-\frac{1}{2}} &= \frac{-\Pi_3 + i\Pi_4 + i\Pi_6 + \Pi_7}{2} \ , \\
\Pi_{\frac{1}{2},-\frac{1}{2}} &= \frac{\Pi_3 + i\Pi_4 - i\Pi_6 + \Pi_7}{2} \ , \\
\Pi_{-\frac{1}{2},\frac{1}{2}} &= \frac{\Pi_3 - i\Pi_4 + i\Pi_6 + \Pi_7}{2} \ , \\
\Pi_{\frac{1}{2},\frac{1}{2}} &= \frac{-\Pi_3 - i\Pi_4 - i\Pi_6 + \Pi_7}{2} \ , \\
\Pi_{0,-1} &= -\frac{1}{\sqrt{2}}\Pi_5 - i\sqrt{\frac{3}{2}}\Pi_8 + \Pi_9 \ , \\
\Pi_{0,1} &= -\frac{1}{\sqrt{2}}\Pi_5 + i\sqrt{\frac{3}{2}}\Pi_8 + \Pi_9 \ , \\
\Pi_{0,0} &= \sqrt{2}\Pi_5 + \Pi_9 \ .
\end{aligned} \tag{2.26}$$

From these expressions it can be shown that the operation of charge conju-

gation acts on this multiplet as a transformation of $SO(4)$. Under a charge conjugation, in fact,

$$\begin{aligned}
&\Pi_{1,0} \longleftrightarrow \Pi_{-1,0} \\
&\Pi_{\frac{1}{2},\frac{1}{2}} \longleftrightarrow \Pi_{-\frac{1}{2},-\frac{1}{2}} \\
&\Pi_{\frac{1}{2},-\frac{1}{2}} \longleftrightarrow \Pi_{-\frac{1}{2},\frac{1}{2}} \\
&\Pi_{0,-1} \longleftrightarrow \Pi_{0,1} \\
&\Pi_{0,0} \longleftrightarrow \Pi_{0,0}
\end{aligned} \tag{2.27}$$

The matrix representing this transformation, in the isospin basis, is given by

$$\mathcal{C} = \begin{pmatrix}
0 & 1 & 0 & 0 & 0 & 0 & 0 & 0 & 0 \\
1 & 0 & 0 & 0 & 0 & 0 & 0 & 0 & 0 \\
0 & 0 & 0 & 0 & 0 & 1 & 0 & 0 & 0 \\
0 & 0 & 0 & 0 & 1 & 0 & 0 & 0 & 0 \\
0 & 0 & 0 & 1 & 0 & 0 & 0 & 0 & 0 \\
0 & 0 & 1 & 0 & 0 & 0 & 0 & 0 & 0 \\
0 & 0 & 0 & 0 & 0 & 0 & 0 & 1 & 0 \\
0 & 0 & 0 & 0 & 0 & 0 & 1 & 0 & 0 \\
0 & 0 & 0 & 0 & 0 & 0 & 0 & 0 & 1
\end{pmatrix}, \tag{2.28}$$

which belongs to $SO(4)$, the isospin group itself. As a consequence, any G-parity is equivalent to an isospin rotation and does not provide selection rules for transition amplitudes. Implications of this feature will be discussed in Chapter 4.

2.5 Beyond a composite Higgs: $Sp(2N)$ and conformality

We have seen in Section 2.2.2 that reasonable composite models rely on gauge theories based on the gauge group $Sp(N_c)$ with $N_c = 2N$, which is introduced in Appendix A. The theory described by $Sp(4)$ with $N_{\rm f} = 2$ and $N_{\rm as} = 3$ Dirac fermions provides a simple example of partial compositeness, granting an explanation to the microscopic origin of two of the heavier particles of the SM, the top quark and the Higgs, identifying them as portals to new physics.

Higgs compositeness alone motivates the development of tools that allow to probe the non-perturbative dynamics of $Sp(2N)$ gauge theories. Adding to that, we mention that these theories have been proposed in many other contexts. The theory with $N_{\rm f} = 2$ and $N_{\rm as} = 0$ Dirac fermions finds applications in the simplest realisation of the strongly interacting massive particle scenario for dark matter (see e.g. [57–59] or even more recently [53, 60, 61]). In addition, $Sp(2N)$ gauge theories might have implications in the physics of the early universe, which can be tested in present and future gravitational waves experiments[62–67]. This is because they give rise to a relic stochastic background of gravitational waves [68–72]. $Sp(2N)$ gauge theories also offer an additional environment in which features of strongly-interacting quantum field theories can be studied, from confinement [11] to conformality.

The concept of the conformal window has been introduced in Section1.4. The determination of its boundaries in strongly-interacting gauge theories coupled to matter remain an open problem of great importance, with implications for technicolor, Higgs and partial compositeness, dark matter, see [40, 73–77] and references therein.

Lattice studies of the extent of the conformal window have mostly focused on $SU(N_c)$ gauge theories. Results for $SU(3)$ coupled to eight fundamental Dirac fermions [78–83] and $SU(3)$ coupled to two two-index symmetric (sextet) Dirac fermions show some evidence of a light scalar state, which could be identified as a dilaton [84, 85], whose existence could have important phenomenological implications [86].

The idea of carrying similar studies in order to identify the extent of the conformal window in $Sp(2N)$ gauge theories is very tempting. Conformal theories, however, are a challenging subject for lattice studies, since their dynamics needs to be probed at very small masses, as well as at very large volumes, in order to reproduce scale invariance.

With these many motivations, this work will also cover the effort of implementing $Sp(2N)$ gauge theories in Grid [55, 87], a high level, architecture-independent, C++ library for lattice gauge theories. The portability of Grid's single source-code across many architectures that characterise the exascale platform landscape makes it an ideal tool for a long-term computational strategy. The goal is to extensively study composite Higgs models and determine the extent of the conformal window.

2.5.1 Symplectic gauge theories

Since symplectic gauge theories are less common, in the literature, compared to theories based on $SU(N_c)$, we spend some lines writing down their features. The $Sp(2N)$ continuum field theories of interest (with $N > 1$), written in Minkowski space with signature mostly '$-$', have the following Lagrangian density (we borrow notation and conventions from Ref. [45]):

$$\begin{aligned}\mathcal{L} \;=\; & -\frac{1}{2}\mathrm{Tr}\; G_{\mu\nu}G^{\mu\nu} \;+\; \frac{1}{2}\sum_{i}^{N_{\rm f}}\left(i\overline{Q^i}_a\gamma^\mu\left(D_\mu Q^i\right)^a \;-\; i\overline{D_\mu Q^i}_a\gamma^\mu Q^{i\,a}\right) \\ & - m^{\rm f}\sum_{i}^{N_{\rm f}}\overline{Q^i}_a Q^{i\,a} + \frac{1}{2}\sum_{k}^{N_{\rm as}}\left(i\overline{\Psi^k}_{ab}\gamma^\mu\left(D_\mu\Psi^k\right)^{ab} \;-\; i\overline{D_\mu\Psi^k}_{ab}\gamma^\mu\Psi^{k\,ab}\right) \\ & - m^{\rm as}\sum_{k}^{N_{\rm as}}\overline{\Psi^k}_{ab}\Psi^{k\,ab}\,. \end{aligned} \tag{2.29}$$

The fields $Q^{i\,a}$, with $i = 1, \cdots, N_{\rm f}$, are Dirac fermions that transform in the fundamental representation of $Sp(2N)$, as indicated by the index $a = 1, \cdots, 2N$, while the $\Psi^{k\,ab}$ ones, with $k = 1, \cdots, N_{\rm as}$, transform in the 2-index antisymmetric representation of the gauge group, (ab) being the color multi-index. More details about higher representations are provided in Section 3.2.6. The covariant derivatives are defined by making use of the transformation properties under the action of an element U of the $Sp(2N)$ gauge group,

$$Q \to UQ\,, \quad \text{and} \quad \Psi \to U\Psi U^{\rm T}\,. \tag{2.30}$$

They can be written in terms of the gauge field $A_\mu \equiv A_\mu^a T^a$, where T^a are the generators of $Sp(2N)$ (see Appendix A) to read as follows:

$$D_\mu Q^i \;=\; \partial_\mu Q^i \;+\; igA_\mu Q^i\,, \tag{2.31}$$

$$D_\mu\Psi^j \;=\; \partial_\mu\Psi^j \;+\; igA_\mu\Psi^j \;+\; ig\Psi^j A_\mu^{\rm T}\,, \tag{2.32}$$

where g is the gauge coupling. The field-strength tensor is given by

$$G_{\mu\nu} \;\equiv\; \partial_\mu A_\nu - \partial_\nu A_\mu + ig\left[A_\mu\,,\,A_\nu\right]\,, \tag{2.33}$$

where $[\cdot\,,\cdot]$ is the commutator.

The $SU(N_{\rm f})_L \times SU(N_{\rm f})_R$ and $SU(N_{\rm as})_L \times SU(N_{\rm as})_R$ global symmetries acting

on the flavor indexes of Q^i and Ψ^k of Eq. (2.29), respectively, are enhanced to $SU(2N_{\rm f})$ and $SU(2N_{\rm as})$ once the Lagrangian is expressed in terms of two-component spinors, which brings us into the context of Section 1.5 The mass terms break the symmetries to the maximal $Sp(2N_{\rm f})$ and $SO(2N_{\rm as})$ subgroups. Bilinear fermion condensates arise non-perturbatively, breaking the symmetries according to the same pattern, and hence one expects the presence of $N_{\rm f}(2N_{\rm f}-1)-1$ PNGBs in the (f) sector (for $N_f > 1$), and $N_{\rm as}(2N_{\rm as}+1)-1$ in the (as) sector.

The main parameters governing the system are hence N, $N_{\rm f}$, and $N_{\rm as}$, and in most of this work we refer to the theory with $N = 2$, $N_{\rm f} = 0$, and $N_{\rm as} = 4$ as a case study. The running coupling, g, obeys a renormalisation group equation (RGE) in which the beta function at the 1-loop order is scheme-independent,

$$\beta \;=\; -\frac{g^3}{(4\pi)^2} b_1, \tag{2.34}$$

and is governed by the coefficient b_1, which for a non-Abelian theory coupled to Dirac fermions can recall the expression:

$$b_1 = \frac{11}{3} C_2(G) - \frac{4}{3} N_{\rm f} \frac{\dim_{\rm f}}{\dim_G} C_2({\rm f}) - \frac{4}{3} N_{\rm as} \frac{\dim_{\rm as}}{\dim_G} C_2({\rm as}) \tag{2.35}$$

$$\tag{2.36}$$

and, specifically for $Sp(2N)$ groups, becomes

$$b_1 = \frac{11}{3}(N+1) - \frac{2}{3} N_{\rm f} - \frac{4}{3} N_{\rm as} \frac{N(2N-1)-1}{N(2N+1)} N \,. \tag{2.37}$$

The coefficients $C_2(G)$, $C_2({\rm f})$, $C_2({\rm as})$ are quadratic Casimir operators in the adjoint, fundamental and antisymmetric representations, while $\dim_G$, $\dim_{\rm f}$, $\dim_{\rm as}$ are the dimensions of these representations, respectively. As for $SU(N_c)$ theories, here we also restrict our attention to asymptotically free theories, for which b_1 is positive. For $Sp(2N)$ theories with $N_{\rm f} = 0$, this requirement sets the upper bound $N_{\rm as} < \frac{11(N+1)}{4(N-1)}$, which for $N = 2$ yields $N_{\rm as} < 33/4$—perturbatively. The spectrum of mesons depends on the mass, $m^{\rm f,as}$, of the fermions, by varying which we can test the IR behaviour, as described in Section 1.4.

Before embarking in a lattice study, it can be useful to check the determinations on the bounds of the conformal window available from various

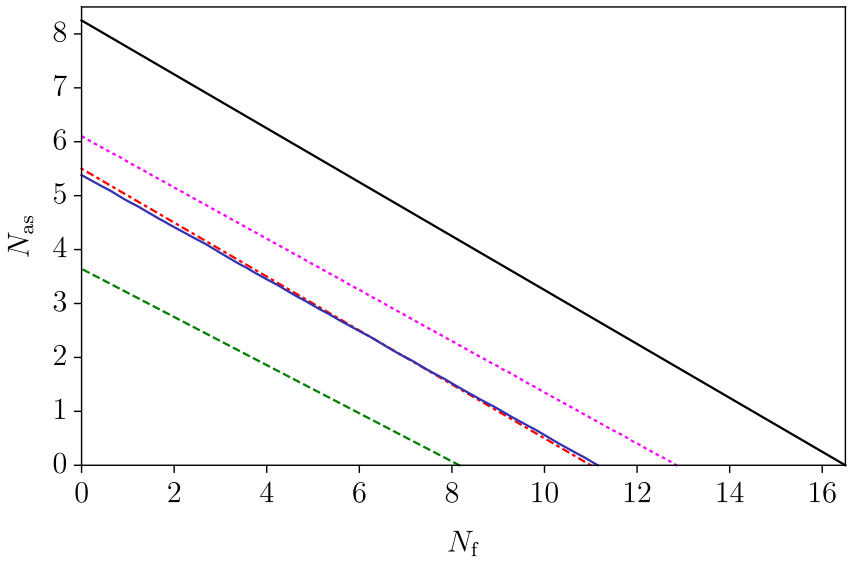

Figure 2.2 *From Ref. [2]: estimates of the extent of the conformal window in $Sp(4)$ theories coupled to $N_{\rm f}$ Dirac fermions transforming in the fundamental and $N_{\rm as}$ in the 2-index antisymmetric representation. The black solid line denotes the upper bound of the conformal window, while different coloured and shaped lines denote alternative analytical estimates of the lower bound, obtained with different approximations. The dashed line is obtained by imposing the constraint $b_2(N_{\rm f}, N_{\rm as}) = 0$. The dot-dashed line is the result of the all-order beta function with the assumption that the anomalous dimensions of the fermion bilinears are $\gamma_{\bar{\Psi}\Psi} = \gamma_{\bar{Q}Q} = 1$. The dotted line is the result of the Schwinger-Dyson analysis. The Banks–Zaks expansion leads to the lower (blue) solid line [4]. Details about these approximations can be found in [2, 5] and individual results are found in [4–9].*

approximations[4–9]. The idea is to identify candidates in the $(N, N_{\rm f}, N_{\rm as})$ space. Indeed, this is only a guide, since the various approximations do not allow to control the systematics of the predictions. For this reason, here we do not go into any detail, but we show a summary of such results in Fig. 2.2, referring to [2, 4–9] and references therein for additional details.

The theory with $N_{\rm f} = 0$ and $N_{\rm as} = 4$ appears to be a reasonable candidate: it is close to estimates of lower bound for the conformal windows, and it contains a minimal number of flavors, making it possible to explore the dynamics of these theories at a reasonable computational cost. For this reason, $Sp(4)$ with $N_{\rm as} = 4$ will be the main focus in the validating tests we performed in our implementation of symplectic gauge theories in Grid.

Chapter 3

Lattice Gauge Theories

The previous chapters identified the gauge theories that we intend to study, with motivations including the phenomenology of the Higgs sector and the determination of the conformal window. We narrowed the focus of this work down to the Ferretti model and its two-flavors simplification, which provide a non-trivial yet accessible environment to develop theoretical and computational tools for composite Higgs models, and $Sp(4)$ with four flavors in the two-index antisymmetric. In order to probe the confining regime of these models, where perturbation theory is not reliable, lattice simulations must be used. With this motivation we briefly introduce, in this Chapter, lattice methods to study gauge theories. The final goal is the evaluation of expectation values of the type

$$\langle O \rangle = \frac{\int \mathcal{D}\phi \, O[\phi] \, e^{-S[\phi]}}{\int \mathcal{D}\phi \, e^{-S[\phi]}} \, , \tag{3.1}$$

where ϕ are the degrees of freedom of the system, and S its action.

In this work, we adopt the Hybrid Monte Carlo (HCM) algorithm [88]. After some introductory sections, this chapter will develop around the Hybrid Monte

Carlo (HCM) algorithm [88] as it was implemented in order to study $SU(N_c)$ and $Sp(N_c)$ gauge theories in Refs. [1, 2].

3.1 The Lattice Regularisation

We define a gauge theory on a Euclidean four-dimensional lattice with spacing a, L/a sites in the space directions and T/a sites in the time direction. Field variables are analytically continued to Euclidean space by performing a Wick rotation, for which we refer to Appendix B. Formulating the theory on a lattice is by all means a regularisation, since $\frac{2\pi}{a}$ is an ultraviolet cutoff for the absolute value of the momentum, in any direction. Additionally, $2\pi/L$ and $2\pi/T$ regulates the IR.

Derivatives are replaced by discrete differences. We introduce

$$\partial_\mu f(x) = \frac{f(x + a\hat{\mu}) - f(x)}{a} \,, \tag{3.2}$$

$$\partial^*_\mu f(x) = \frac{f(x) - f(x - a\hat{\mu})}{a} \,, \tag{3.3}$$

$$\partial_\mu \partial^*_\mu f(x) = \frac{f(x + a\hat{\mu}) - 2f(x) + f(x - a\hat{\mu})}{a^2} \,. \tag{3.4}$$

As a goes to zero, both ∂_μ and ∂^*_μ reproduce the derivative in the continuum up to $\mathrm{O}(a)$. The symmetric derivative $(\partial_\mu + \partial^*_\mu)/2$ is preferred, since the continuum limit is reached faster, as $\mathrm{O}(a^2)$. For an irreducible representation R of the gauge group, fermionic fields ψ^R are defined on lattice sites, which we denote by x, while gauge fields are defined from links variables between sites, denoted as $U^R_\mu(x)$: these are an analogue of the continuum Wilson line W

$$W(x, y) = P \exp\left(ig \int_x^y A^a_\mu(z) T^a dz^\mu \right) \,. \tag{3.5}$$

P being the path-ordering operator. Link variables where the representation is not specified will be assumed to be in the fundamental representation.

Let $\mathcal{G}$ be the gauge group, and $V \in \mathcal{G}$. The transformation property of the

fermion field and the link variable under $\mathcal{G}$ are

$$\psi^{\mathrm{R}}(x) \mapsto V(x)\psi^{\mathrm{R}}(x), \qquad \bar{\psi}^{\mathrm{R}}(x) \mapsto \bar{\psi}^{\mathrm{R}}(x)V(x)^{\dagger}, \tag{3.6}$$

$$U_{\mu}^{\mathrm{R}}(x) \mapsto V(x)U_{\mu}^{\mathrm{R}}(x)V(x+a\hat{\mu})^{\dagger} , \tag{3.7}$$

$$U_{-\mu}^{\mathrm{R}}(x) \mapsto V(x)U_{-\mu}^{\mathrm{R}}(x)V(x-a\hat{\mu})^{\dagger} . \tag{3.8}$$

Notice that, for consistency,

$$U_{-\mu}^{\mathrm{R}}(x) = U_{\mu}^{\mathrm{R}}(x-\hat{\mu})^{\dagger} . \tag{3.9}$$

With these definitions a naive discretisation of the Dirac action,

$$S_F^{\text{naive}} = a^4 \sum_x \bar{\psi}^{\mathrm{R}}(x) \left(\gamma_\mu \frac{U_{\mu}^{\mathrm{R}}(x)\psi^{\mathrm{R}}(x+\hat{\mu}) - U_{-\mu}^{\mathrm{R}}(x)\psi^{\mathrm{R}}(x-\hat{\mu})}{2a} + m\psi^{\mathrm{R}}(x) \right) , \tag{3.10}$$

is gauge invariant. The interpretation of the gauge links in terms of continuum gauge fields is clarified by the relation

$$U_{\mu}^{\mathrm{R}}(x) = \exp(iaA_{\mu}^{\mathrm{R}}(x)) , \tag{3.11}$$

where $A_{\mu}^{\mathrm{R}}(x) = A_{\mu}^{a}(x)T_{\mathrm{R}}^{a}$ is now a member of the Lie algebra of $\mathcal{G}$, with generators T_{R}^{a}. In this work we consider $SU(N)$ or its subgroups, so we will always assume that $A_{\mu}^{\mathrm{R}}(x) = A_{\mu}^{\mathrm{R}}(x)^{\dagger}$. By expanding all fields around x in powers of the lattice spacing into Eq. (3.10), we recover a continuum fermionic action compatible with the one defined in Chapter 1, plus $\mathrm{O}(a^2)$ due to the symmetric derivative.

In order to define the gauge action, gauge invariant operators of link variables are needed. The trace of any close loop of such variables is indeed gauge invariant. With this motivation, the minimal non-trivial closed loop of link variables, called plaquette, is introduced:

$$U_{\mu\nu}(x) = U_{\mu}(x)U_{\nu}(x+\hat{\mu})U_{\mu}(x+\hat{\nu})^{\dagger}U_{\nu}(x)^{\dagger} . \tag{3.12}$$

The Wilson gauge action [89] is in fact a sum over plaquettes at all lattice sites, with an additional sum over Lorentz indices $1 \leq \mu < \nu \leq 4$.

$$S_{\mathrm{g}} = \frac{\beta}{N_c} \sum_x \sum_{\mu<\nu} \mathrm{Re\ Tr}\left\{1 - U_{\mu\nu}(x)\right\} , \tag{3.13}$$

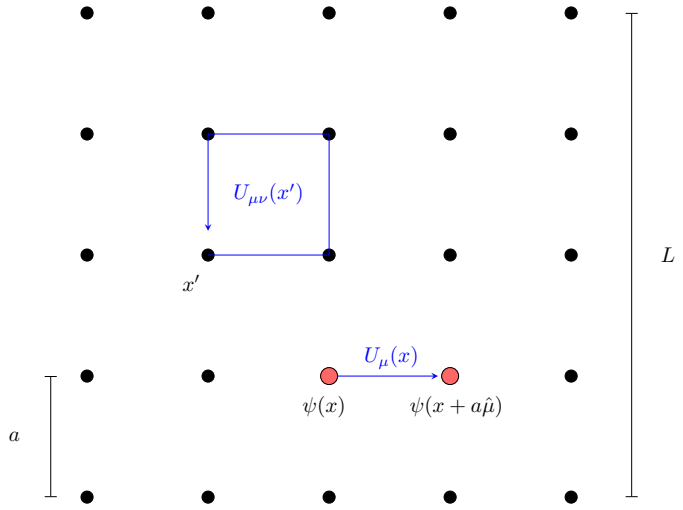

Figure 3.1 *Two-dimensional example of a lattice. The figure displays fermionic fields defined at points x and $x + a\hat{\mu}$, a gauge link connecting the sites, as well as a plaquette $U_{\mu\nu}$ at another lattice site x'.*

where $\beta = 2N_c/g^2$ is the lattice coupling, related to the gauge coupling g^2. Again, an expansion of the link variables provide the Yang-Mills action from Chapter 1 plus $O(a^2)$.

A plaquette, together with gauge link and fermionic variables, are depicted in Fig. 3.1 on a two-dimensional lattice.

3.1.1 Doubling problem and the Wilson action

We illustrate the doubling problem in the simple case of a free theory. Consider the Dirac operator introduced in Eq (3.10) by naively discretising the continuum fermionic action. In the free theory, with $U_\mu(x) = \mathbb{1}$,

$$D_m^{\text{naive}} = \gamma_\mu \frac{\partial_\mu + \partial_\mu^*}{2} + m \ , \tag{3.14}$$

where the differential operators are defined in Eq (3.2). Plane waves are eigenfunctions of the free D_m^{naive}, with eigenvalues given by

$$\tilde{D}_m^{\text{naive}}(p) = i\gamma_\mu \frac{\sin(ap_\mu)}{a} + m \ . \tag{3.15}$$

By defining $\hat{p}_\mu$ as

$$\hat{p}_\mu = \frac{\sin(ap_\mu)}{a} \ , \tag{3.16}$$

which satisfies

$$\lim_{a\to 0} \hat{p_\mu} = p_\mu \ , \tag{3.17}$$

the fermionic propagator obtained in this setup reads

$$S(\hat{p}) = \frac{-i\gamma_\mu \hat{p}_\mu + m}{\hat{p}^2 + m^2} \ . \tag{3.18}$$

The periodicity of $\hat{p}$ implies that, in four dimension, the physical pole is accompanied by 15 extra, unphysical poles which do not vanish in the continuum. This is a manifestation of the doubling problem. Under the condition for which the Nielsen Ninomiya theorem applies [90], a lattice regularisation for the fermionic action that does not break either chirality, translation invariance or analyticity comes with doublers.

One way to overcome the doublers is by breaking chirality explicitly. A popular way of doing so is by adding to the naive fermionic operator of Eq. (3.14) a so-called "Wilson term", which is proportional to the discretised Laplace operator $\partial_\mu \partial^*_\mu$. In order to compare with Eq. (3.18) we compute the propagator in the free theory, in which the Wilson operator reads

$$D_W = \gamma_\mu \frac{\partial_\mu + \partial^*_\mu}{2} - \frac{a}{2}\partial_\mu \partial^*_\mu + m \ , \tag{3.19}$$

which is again diagonal on plane waves, with the resulting eigenvalues

$$\tilde{D}_W(p) = \gamma_\mu \hat{p}^\mu + m + \frac{a}{2}\dot{p}_\mu \dot{p}^\mu \ , \tag{3.20}$$

where $\hat{p}$ is defined in Eq. (3.16), and

$$\dot{p}_\mu = \frac{2}{a}\sin\left(\frac{ap_\mu}{2}\right) \ . \tag{3.21}$$

While the physical pole is preserved, the doublers gain a mass proportional to $1/a$ and they decouple in the continuum. Moving away from the free theory,

the Wilson operator reads

$$(D_{\mathrm{W}})^R_{x,y}\psi^R(x) = (\frac{4}{a} + m)\psi^R(x)$$
$$- \frac{1}{2a}\sum_\mu \left\{(1-\gamma_\mu)\, U^R_\mu(x)\psi^R(x+a\hat{\mu}) + (1+\gamma_\mu)U^R_\mu(x-a\hat{\mu})^\dagger\psi^R(x-a\hat{\mu})\right\} \ . \tag{3.22}$$

While solving the issue posed by the doublers, the Wilson discretisation of the fermionic action comes with some disadvantages. By breaking chirality explicitly, the fermionic mass m renormalises no longer multiplicatively, but it comes with an additive term proportional to a^{-1}. Moreover, compared to the naive action, discretisation effects are here $\mathrm{O}(a)$ due to the Wilson term.

3.1.2 Symanzik improvement

The Symanzik improvement programme [91, 92] is a systematic procedure that allows the reduction of discretisation effects from a given lattice action. One considers an effective theory based on an expansion in powers of a. In proximity of the continuum, the theory on the lattice can be described by the effective action

$$S_{\mathrm{eff}} = S_0 + aS_1 + a^2S_2 + \dots \tag{3.23}$$

where each term is of the type

$$S_k = \int d^4x \mathcal{L}_k \ , \tag{3.24}$$

where $\mathcal{L}_k$ are local operators of dimension $4+k$ that are allowed by the symmetries of the theory, both local and global. The action term S_1 is tuned to exactly cancel the $\mathrm{O}(a)$ discretisation effects from S_0, and so on. In this work, S_0 will be the Wilson action, and we will not improve the gauge action, which is already $\mathrm{O}(a^2)$. The choices for the irrelevant operators composing S_1

are

$$O_1 = \bar{\psi}^R i\sigma_{\mu\nu} F^R_{\mu\nu} \psi^R \ , \tag{3.25}$$

$$O_2 = \bar{\psi}^R D_\mu D_\mu \psi^R + \bar{\psi}^R \overleftarrow{D}_\mu \overleftarrow{D}_\mu \psi^R \ , \tag{3.26}$$

$$O_3 = m \mathrm{Tr} F_{\mu\nu} F^{\mu\nu} \ , \tag{3.27}$$

$$O_4 = m\bar{\psi}^R \gamma_\mu D^\mu \psi^R - m\bar{\psi}^R \gamma_\mu \overleftarrow{D}_\mu \psi^R \ , \tag{3.28}$$

$$O_5 = m^2 \bar{\psi}^R \psi^R \ . \tag{3.29}$$

The operators O_3 and O_5 are already present in the Lagrangian, and their inclusion would amount to a redefinition of the bare coupling and the bare mass. Moreover, O_2 and O_4 can be eliminated by using the equations of motion. The Wilson action can be therefore improved by adding O_1. In terms of lattice variables, the Wilson action would take the contribution

$$S_{\mathrm{clover}}[U^R, \bar{\psi}^R, \psi^R] = a^5 \sum_x c^R_{\mathrm{sw}} \bar{\psi}^R(x) \frac{i}{4} \sigma_{\mu\nu} \hat{F}^R_{\mu\nu}(x) \psi^R(x) \ , \tag{3.30}$$

where $\hat{F}^R_{\mu\nu}(x)$ is a lattice representation of the gauge boson's field strength. Following [93], we use

$$\hat{F}^R_{\mu\nu}(x) = \frac{1}{8a^2} \left\{ Q^R_{\mu\nu}(x) - Q^R_{\nu\mu}(x) \right\} \ , \tag{3.31}$$

where Q^R is the clover combination of plaquettes given by the following expression, where we suppress the representation index for simplicity:

$$\begin{aligned} Q_{\mu\nu} = {} & U_\mu(x)\, U_\nu(x + a\hat{\mu})\, U_\mu^{-1}(x + a\hat{\nu})\, U_\nu^{-1}(x) \\ & + U_\nu(x)\, U_\mu^{-1}(x + a\hat{\mu} + a\hat{\nu})\, U_\nu^{-1}(x - a\hat{\mu})\, U_\mu(x - a\hat{\mu}) \\ & + U_\mu^{-1}(x - a\hat{\mu})\, U_\nu^{-1}(x - a\hat{\mu} - a\hat{\nu})\, U_\mu(x - a\hat{\mu} - a\hat{\nu})\, U_\nu(x - a\hat{\nu}) \\ & + U_\nu^{-1}(x - a\hat{\nu})\, U_\mu(x - a\hat{\nu})\, U_\nu(x + a\hat{\mu} - a\hat{\nu})\, U_\mu^{-1}(x) \ . \end{aligned} \tag{3.32}$$

The coefficient that has to be tuned, c^R_{cw}, is a function of the bare coupling and, more generally, of the fermionic representation. In perturbation theory $c^R_{\mathrm{cw}} = 1$ at lowest order.

3.1.3 Path Integral and the Monte Carlo evaluation

This Chapter has been building up towards the evaluation of expectation values such as the one in Eq. (3.1), to which we now turn our attention. In the cases of interest here, the degrees of freedom of the system are the gauge and fermionic fields (in any representation, which we do not specify in the following equations). The Euclidean partition function reads

$$\mathcal{Z} = \int \mathcal{D}U \mathcal{D}\psi \mathcal{D}\bar{\psi} e^{-S_g[U] - S_f[U,\psi,\bar{\psi}]} \,, \tag{3.33}$$

The path integral will be evaluated with Monte Carlo methods. As a first step, we integrate over the fermionic variables. Due to their spin statistics, these are Grassman variables in the path integral. Since their action is quadratic, they can be integrated exactly,

$$\int \mathcal{D}\psi \mathcal{D}\bar{\psi} e^{-\bar{\psi} D[U] \psi} = \det D[U] \,, \tag{3.34}$$

where D is the discretised Dirac operator. The partition function then reads

$$\mathcal{Z} = \int \mathcal{D}U e^{-S_g[U]} \det D[U] \,. \tag{3.35}$$

Similarly, in the evaluation of the expectation value of an operator $O[U, \psi, \bar{\psi}]$,

$$\langle O \rangle = \frac{1}{\mathcal{Z}} \int \mathcal{D}U \mathcal{D}\psi \mathcal{D}\bar{\psi}\, O[U, \psi, \bar{\psi}]\, e^{-S_g[U] - S_f[U,\psi,\bar{\psi}]} \,, \tag{3.36}$$

the integration over fermionic variables can be performed analytically by using Wick's theorem,

$$\begin{aligned} \langle \bar{\psi}(y_1) \dots \bar{\psi}(y_k) \psi(x_1) \dots \psi(x_k) \rangle_f &= \\ &= \frac{1}{\mathcal{Z}_{\mathrm{F}}} \int \mathcal{D}\psi \mathcal{D}\bar{\psi}\ \bar{\psi}(y_1) \dots \bar{\psi}(y_k) \psi(x_1) \dots \psi(x_k)\ e^{-\bar{\psi} D \psi} = \\ &= (-1)^k \sum_{\mathcal{P}} \mathrm{sign}(\mathcal{P})\ D^{-1}(x_1, y_{\mathcal{P}_1}) \dots D^{-1}(x_k, y_{\mathcal{P}_k}) \,. \end{aligned} \tag{3.37}$$

In the previous expression, $\langle \cdot \rangle_f$ represents the fermionic expectation value only, and $\mathcal{Z}_{\mathrm{F}}$ the fermionic partition function. $\mathcal{P}$ represents the set of all permutations of the integers $1 \dots k$. The integration of the fermionic variable then amounts to the evaluation of propagators, which depend on the gauge

fields. As a consequence, the expectation value of Eq. (3.36) amounts to an integration over the gauge degrees of freedom only

$$\langle O \rangle = \frac{1}{\mathcal{Z}} \int \mathcal{D}U \; O_{\text{Wick}}(D^{-1}[U]) \; \det(D) \; e^{-S_g[U]} \; , \tag{3.38}$$

the function O_{Wick} is condensing, for convenience, all the Wick contractions that result from integrating out the fermions.

The remaining integration over the gauge variables is performed by importance sampling. Suppose we are able to obtain N_{cnfg} independent random variables U_n, $n = 1 \dots N_{\text{cnfg}}$ describing the gauge field U. Suppose that such variables are distributed with the probability density induced by Eq. (3.38)

$$dP[U] = \frac{1}{\mathcal{Z}} \mathcal{D}U \; \det(D) \; e^{-S_g[U]} \; . \tag{3.39}$$

The expectation value of O can be then estimated statistically,

$$\langle O \rangle = \frac{1}{N_{\text{cnfg}}} \sum_n O_{\text{Wick}}[D^{-1}[U_n]] + \mathrm{O}(\frac{1}{\sqrt{N_{\text{cnfg}}}}) \; . \tag{3.40}$$

For non-fermionic observables the expectation value is simply

$$\langle O \rangle = \frac{1}{N_{\text{cnfg}}} \sum_n O[U_n] + \mathrm{O}(\frac{1}{\sqrt{N_{\text{cnfg}}}}) \; . \tag{3.41}$$

Such an evaluation is enabled by the possibility to interpret $\langle O \rangle$ as a statistical average over a probability density. Wick rotating into the Euclidean sector was crucial in this respect. For certain systems, such as theories at finite chemical potential, the Wick rotation is not enough to guarantee a statistical interpretation of the path integral; a problem that is beyond the interest of this work.

We are missing a prescription for drawing the gauge configurations U_n needed to evaluate Eq. (3.40). We use the Hybrid Monte Carlo (HMC), a well established algorithm for generating field configurations for systems that include fermions. The algorithm is described in the next Section.

3.2 The HMC

3.2.1 Preliminaries

The (R)HMC algorithm generates ergodic Markov chains of gauge fields that have equilibrium distribution given by $dP[U]$ of Eq. (3.39). Let us first discuss how to handle the determinant of the fermionic operator D^R, where R denotes the fermionic representation.

It is convenient to introduce an associated Hermitian operator, Q^R,

$$Q^R = \gamma_5 D^R \ . \tag{3.42}$$

When the number of fermions $n_f(R)$ in the representation R is even, the determinant can be expressed in terms of bosonic degrees of freedom, called pseudofermions, defined by

$$(\det D^R)^{n_f(R)} = (\det Q^R)^{n_f(R)} = \int \mathcal{D}\phi\mathcal{D}\phi^\dagger e^{-S_{\rm pf}} \ , \tag{3.43}$$

where

$$S_{\rm pf} = a^4 \sum_x \phi^\dagger(x)({Q^R}^2)^{\frac{n_f(R)}{2}}\phi(x) \ . \tag{3.44}$$

For odd values of n_f, the rational approximation is used to compute odd powers of the determinant above, resulting in a variation of the algorithm known as RHMC.

3.2.2 Molecular Dynamics

The main body of the HMC consists in the molecular dynamics, which we now describe. A fictitious classical system is introduced. Its generalised coordinates are the angular parameters of link variables U,

$$U_\mu(x) = \exp\left(i\omega^a T_F^a\right) \ , \tag{3.45}$$

with conjugated momenta π living in the Lie Algebra of the gauge group

$$\pi_\mu(x) = \pi_\mu^a(x) T_F^a \ . \tag{3.46}$$

The associated classical Hamiltonian is

$$H = \frac{1}{2}\sum_{x,\mu,a} \pi_\mu^a(x)\pi_\mu^a(x) + S_g + \sum_R S_{\rm pf}^R \,. \tag{3.47}$$

Let τ be the fictitious time of the classical system. The equations of motions are

$$\frac{d}{d\tau}U_\mu(x) = \pi_\mu(x)U_\mu(x) \tag{3.48}$$

$$\frac{d}{d\tau}\pi_\mu(x) = -\frac{dH}{dU_\mu} \equiv F_\mu(x) \;, \tag{3.49}$$

where the classical force $F_\mu(x)$, drives the evolution of the momenta. From the previous equation, it is clear that the force, like the momenta, is defined in the Lie Algebra of the gauge group. Since the Hamiltonian is the sum of the different actions, the force takes factorised contributions from the gauge and the fermionic parts, i.e. $F^a = (F_g)^a + \sum_R (F_f^R)^a$. Each part of the fermionic force, $(F_f^R)^a$, depends on the fermionic representation though the fields

$$U_\mu^R(x) = \exp\left(i\omega^a T_R^a\right) \;, \tag{3.50}$$

that appear in the fermionic operators (for instance the Wilson operator of Eq. (3.22)). Expressions for the gauge and fermionic forces, including the clover term, can be found in Refs. [13, 94]: we stress, however, that the evaluation of the fermionic force relies on the inversion of the fermionic operator. As a consequence, the evaluation of the fermionic force is much more expensive, in terms of computing time, than the evaluation of the gauge force.

The Molecular Dynamics (MD) consists in the numerical integration of the Hamilton equations (3.48). At the end of the integration, a Metropolis step is performed. This consists in accepting the resulting configuration U' with probability

$$P = \min\left\{1, e^{-\Delta H}\right\} \;, \qquad \Delta H = H[U'] - H[U] \;, \tag{3.51}$$

U being the configuration of the gauge fields at the beginning of the trajectory.

3.2.3 The Algorithm

The HMC [88] algorithm consists of the following steps:

- A starting configuration U_i is selected. For each link, a canonically conjugated momentum is extracted from a Gaussian distribution. Pseudofermions distributed according to the integrand in Eq. (3.43) are generated with the Heat Bath algorithm.
- The gauge fields are evolved by integrating, numerically, the equations of motion of a fictitious classical system. This step is referred to as Molecular Dynamic (MD) evolution, and an iteration of these steps is called "trajectory".
- A Metropolis test accepts or rejects the resulting field configurations, eliminating systematic effects due to the finite step of the numerical integration of the MD.

Iterating this procedure for N_{cnfg} trajectories, one ends with N_{cnfg} configurations of gauge fields distributed according to the chosen probability distribution.

3.2.4 Tuning and parameters

We briefly discuss the parameters entering the HMC. The theory is defined by the lattice coupling β, and the numbers of fermions in the various representations R_i. These come with bare masses m_0^R, which in our case will have to be tuned due to the additive renormalisation induced by the Wilson term. Particularly important is the value of the critical mass m_c^R, i.e. the bare mass at which the renormalised mass vanishes. While its value has to be found by extrapolating the fermionic masses to zero, a first guess can be provided by the perturbative prediction for m_c^R. This can make the exploration in parameter space quicker. As shown in Chapter 4, perturbative predictions for m_c^R can lie surprisingly close to their non-perturbative counterparts.

In the molecular dynamics, the integration step for the classical equations of motions, as well as the length of the trajectory, have to be chosen. A shorter trajectory will result in a slower exploration of the phase space,

and it potentially leads to high correlation between observables evaluated at subsequent trajectories (autocorrelation). The integration step is also crucial. The continuous equations of motions preserve the Hamiltonian, and within the molecular dynamics the energy violations, i.e. differences in the Hamiltonian at the beginning and at the end of the trajectory, are induced by the finite integration step. This has to be tuned so that violations in the Hamiltonian are small enough to guarantee a good acceptance rate for the Metropolis test. In this work, we tuned the acceptance rate to be roughly 80%. One should be wary of a higher rate, which can be accompanied by a strong autocorrelation.

3.2.5 Implementation details

In order to simulate SU and Sp gauge theories, we used the lattice library Grid [55]. While the simulation of $SU(N_c)$ was already established within the Grid framework, the necessary software for the simulation of $Sp(2N)$ was added and tested as part of this work. Adding to the fact that simulations of the symplectic group are far less common, it is worth to spend some lines discussing salient differences between more familiar functions used to simulate QCD.

In the numerical integration of Eq. (3.48), it is required to project the HMC force on the Lie algebra of the gauge group. In Grid, the embedding of the force-projection within the integrator requires the forces to be anti-hermitian. Hence, a projection operation to the matrices of the algebra $\mathfrak{sp}(2N)$ must be defined. This can be done in analogy with the projection to $\mathfrak{su}(N_c)$, defined for a generic matrix M as

$$P_{\mathrm{tr}} P_{\mathrm{aH}} M \ , \tag{3.52}$$

where

$$P_{\mathrm{tr}} M \equiv M - \mathbb{1}_{N_c} \mathrm{Tr}(M)/N_c \ , \tag{3.53}$$

and

$$P_{\mathrm{aH}} M \equiv (M - M^\dagger)/2 \ , \tag{3.54}$$

are the projectors to its traceless and to its anti-hermitian parts, respectively. For $\mathfrak{sp}(2N)$, the projection is instead defined as,

$$P_{\mathrm{aH}} P^{-}_{\mathrm{Sp}} P_{\mathrm{tr}} \, M \ , \tag{3.55}$$

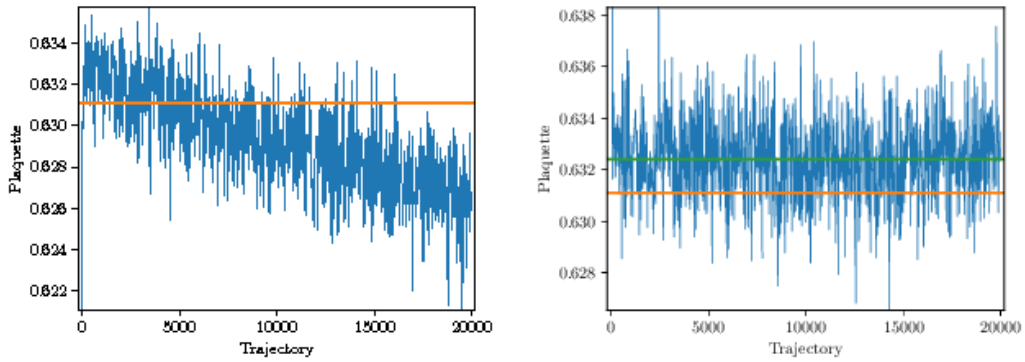

Figure 3.2 *Figure taken from Ref. [10]: average plaquette computed with (right panel) and without (left panel) applying the re-sympletification procedure at each update. The orange line represents the corresponding value for the plaquette obtained in Ref. [11]. The green line is the fit of the plaquette to a constant.*

where

$$P_{\mathrm{Sp}}^{\pm} M \equiv \frac{M \pm \Omega M^{*} \Omega}{2} \,. \tag{3.56}$$

Notice that P_{Sp}^{-} returns an anti-hermitian matrix, while P_{Sp}^{+} projects on a space of hermitian matrices.

The re-sympletification of gauge links to the $Sp(2N)$ group manifold has also been implemented in Grid. By re-sympletification, named in analogy with the re-unitarisation process of $SU(N_c)$ simulations, we refer to the projection of gauge links on the Sp group manifold that is performed at every update. The necessity for such procedure can be appreciated from Fig. 3.2, which we borrow from Ref. [10]. On the left panel, the simulation is done without re-sympletification: due to the finite machine precision of the simulation, the average Plaquette drifts as the gauge links are driven away from the group manifold. Conversely on the right panel, where the projection is performed, the Plaquette fluctuates around a stable value along the trajectories.

The algorithm, described in Ref. [10], is a modification of the Gram-Schmidt process designed to take into account the condition in Eq. (A.13). After normalising the first column of the matrix U, the $(N+1)$-th column is set to

$$\mathrm{col}(U)_{j+N} = -\Omega\, \mathrm{col}(U)_{j}^{*} \,. \tag{3.57}$$

The second column is then obtained by orthonormalisation with respect to both the first and the $N+1$-th column. An iteration of this process leads to a symplectic matrix. At the end, the matrix can be normalised to have unit

determinant.

3.2.6 More on Higher Representations

In this Section we discuss some aspects of higher representations that have been useful to develop and understand the HMC in the context of BSM theories. It is known that any irreducible group representation can be obtained from the defining, fundamental representation (F). For most phenomenological applications, the fermionic representations of interest are the adjoint (Adj), the two-index symmetric (2S) and antisymmetric (2AS). The adjoint is obtained by the product of the fundamental with the anti-fundamental, which also contains a singlet. For $SU(N_c)$,

$$N_c \otimes N_c^* = \underbrace{N_c^2 - 1}_{\text{Adj}} \oplus 1 \ . \tag{3.58}$$

The two-indices are instead obtained from the product of two fundamental representations

$$N_c \otimes N_c = \underbrace{N_c(N_c+1)/2}_{\text{2S}} \oplus \underbrace{N_c(N_c-1)/2}_{\text{2AS}} \ . \tag{3.59}$$

For $Sp(2N) = Sp(N_c)$ the composition is slightly different. N_c^* is not independent of N_c: the adjoint will be then equal to one of the two-indices. In fact, the invariant tensor of $Sp(2N)$ is the antisymmetric tensor ϵ_{ij}, which causes the singlet to separate from the 2AS representation

$$N_c \otimes N_c = \underbrace{N_c(N_c-1)/2 - 1}_{\text{2AS}} \oplus 1 \oplus \underbrace{N_c(N_c+1)/2}_{\text{2S=Adj}} \ . \tag{3.60}$$

For completeness we mention that $SO(2N)$ has a similar decomposition. The invariant tensor is now the symmetric δ_{ij}, causing the singlet to separate from the 2S

$$N_c \otimes N_c = \underbrace{N_c(N_c-1)/2}_{\text{2AS=Adj}} \oplus 1 \oplus \underbrace{N_c(N_c+1)/2 - 1}_{\text{2S}} \tag{3.61}$$

Numerically, the upgrade from fundamental to higher representation is done as described in Ref. [94]. In this work we use, for both gauge groups, fundamental and 2AS fermions. We therefore recall the procedure for the

case of interest. Link variables $U_\mu^{(\mathrm{as})}(x)$ are obtained from the links in the fundamental according to

$$U^{(\mathrm{as})}_{\mu,\,(ab)(cd)} = \mathrm{Tr}\left(e^{(ab)\,T} U^{(\mathrm{f})}_\mu e^{(cd)} U^{(\mathrm{f})\,\mathrm{T}}_\mu\right) \,, \tag{3.62}$$

where $e^{(ab)}$ are the elements of an orthonormal basis in the $\dim_{\mathrm{AS}}$-dimensional space of $N_c \times N_c$ antisymmetric matrices. For $SU(N_c)$, the multi-index is (ab) with $1 \le a < b \le N_c$, and the entry ij of the base is

$$(e^{ab}_{\mathrm{AS}})_{ij} = \frac{1}{\sqrt{2}} \left(\delta_{ai}\delta_{bj} - \delta_{aj}\delta_{bi}\right) \,. \tag{3.63}$$

For $SU(4)$ the representation is dimension six and the multi-index takes value $(ab) = (12), (13), (14), (23), (24), (34)$.

For $Sp(2N)$, the basis is additionally Ω-traceless, and the multi-indices (ab) run over the values $1 \le a < b \le 2N$. The entry ij of each element of the basis is defined as follows. For $b \neq N + a$,

$$e^{(ab)}_{ij} \equiv \frac{1}{\sqrt{2}} \left(\delta_{aj}\delta_{bi} - \delta_{ai}\delta_{bj}\right) \,, \tag{3.64}$$

while for $b = N + a$ and $2 \le a \le N$,

$$e^{(ab)}_{i,i+N} = -e^{(ab)}_{i+N,i} \equiv \begin{cases} \frac{1}{\sqrt{2a(a-1)}} \,, & \text{for } \; i < a \,, \\ \frac{1-a}{\sqrt{2a(a-1)}} \,, & \text{for } \; i = a \,, \end{cases} \tag{3.65}$$

and zero otherwise. It is easy to verify that each element of this basis satisfies the Ω-traceless condition $\mathrm{Tr}(e^{(ab)}\Omega) = 0$, where the symplectic matrix Ω is defined in Eq. (A.11). For $Sp(4)$ the representation is dimension five, and the multi-index takes the values $(ab) = (12), (14), (23), (24), (34)$.

Expression for the generators can be easily obtained by expanding the gauge links:

$$(T^a_{\mathrm{as}})_{(ab)(cd)} = \mathrm{Tr}\left(e^{(ab)\,T} T^a_{\mathrm{f}} e^{(cd)} + e^{(ab)\,T} e^{(cd)} T^{a\,T}_{\mathrm{f}}\right) \,. \tag{3.66}$$

These equations correspond to the one adopted in the code.

Chapter 4

Results for $SU(4)$

This Chapter presents a lattice study of the $SU(4)$ gauge theory with two Dirac fermions in the fundamental and two in the two-index antisymmetric representation, which has been introduced in Section 2.4 as a prototype for the model of partial compositeness proposed by Ferretti [56] which we briefly described in Section 2.3. The focus of this work has been the methodologies behind the computation of the spectrum and the extrapolation to the chiral point for a theory with matter in multiple representations. While being still technical, this study provides important steps towards a non-perturbative understanding of the spectrum of theories of partial compositeness, which present a richer dynamics compared to single-representation theories. The multi-representation features are studied first in perturbation theory, and then non-perturbatively by adopting a dual outlook on lattice data through a joint analysis of time-momentum correlation functions and smeared spectral densities.

4.1 Perturbative Results

In this work we adopt a Wilson-type discretisation of the Dirac action with a clover term, the details of which will be given in Sec. 4.2. This choice for the action breaks chiral symmetry. The critical mass, i.e. the value of the bare mass of a fermion corresponding to a vanishing renormalised mass can be first estimated in perturbation theory, suggesting values for the numerical simulations, and providing first insights on the multi-representation dynamics. The perturbative expansion of the Wilson action generates, for each representation, the same vertices that appear in lattice QCD up to group theoretical factors, making it easy to generalise the existing result. To this end, we will refer to the calculation of the critical mass of Wilson fermions at two loops [12] in lattice QCD, the cactus resummation at one loop [95] and their generalisation to a generic representation of $SU(N)$ [52]. These results will be extended to the case of multiple representations in the reminder of this section.

4.1.1 Multiple representations

In this section we analyse the effect of multiple representations in the computation of the fermionic self-energy. The motivation is to gain insights about the way a representation can affect the other. For simplicity we use, for this task, Wilson-type fermions, delegating the discussion of the clover term and cactus improvement to the next section where we estimate critical masses.

For a given representation R, we write the perturbative expansion of the one-particle irreducible two-point function as

$$\Sigma_R\left(p, g_0, m_0^R\right) = g_0^2 \Sigma_R^{(1)}\left(p, m_0^R\right) + g_0^4 \Sigma_R^{(2)}\left(p, m_0^R\right) + \mathcal{O}(g_0^6)\,. \tag{4.1}$$

In evaluating the Feynman diagrams contributing to the elements of the perturbative expansion, we set the fermion masses to their tree level values, $m_0^R = 0$. The one-loop contribution Σ_R^1, for instance, comes from two diagrams, a tadpole and a sunset. It is useful to parametrise Σ_R^1 in terms of powers of the lattice spacing,

$$\Sigma_R^{(1)}(p,0) = \frac{\Sigma_{R,\,\mathrm{a}}^{(1)}}{a} + i\not{p}\Sigma_{R,\,\mathrm{b}}^{(1)}\,. \tag{4.2}$$

Imposing the vanishing of the renormalised mass for the fermion yields an expression for the critical mass at one loop

$$m_{\mathrm{c},\,R}^{(1)} = \frac{g_0^2 \Sigma_R^{(1)}(0,0)}{a} = \frac{g_0^2 \Sigma_{R,\,\mathrm{a}}^{(1)}}{\mathrm{a}} \; . \tag{4.3}$$

The same can be done order by order in powers of the coupling g_0^2, which is related to the usual lattice coupling by

$$\beta = \frac{2N}{g_0^2} \; . \tag{4.4}$$

The result for $\Sigma_R^{(1)}$ can be written in terms of the contribution of each diagram [12]

$$\Sigma_R^{(1)}(0,0) = 2C_2(R) \left[c_1^{(1)} + c_2^{(1)} \right] \; , \tag{4.5}$$

where $C_2(R)$ is the quadratic Casimir defined in Eq. (A.3), and

$$c_1^{(1)} + c_2^{(1)} = -0.162857058711(2) \; . \tag{4.6}$$

In the following we omit, in the expansion terms of the self energy, the dependence from p and m_0 which are set to zero. The result of Eq. (4.5), plugged into Eq. (4.3), provides the one-loop estimate of the critical mass. However, it contains no information about the multi-representation dynamics, for which we need at least the $\mathcal{O}(g_0^4)$ result. In Wilson lattice QCD, $\Sigma^{(2)}$ takes contribution from 26 diagram [12]. If the theory has fermions in two different representation R and R', there are four additional diagrams contributing to

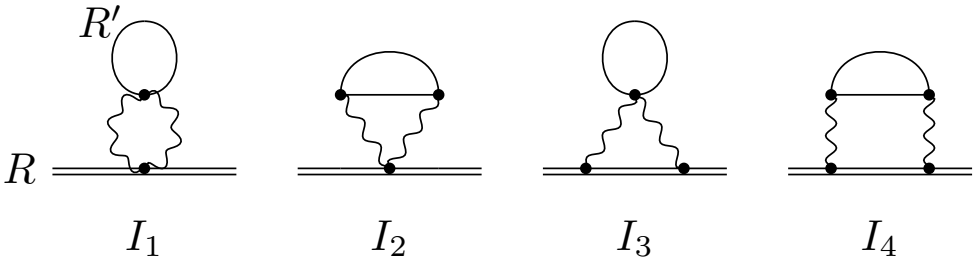

Figure 4.1 *Two-loop diagrams in which the representation R' (solid line) can contribute to the self energy, and therefore the critical mass, of the fermion in the representation R (double solid line). These diagrams, apart from group theoretical invariants, depend on factors that have been computed in Ref. [12].*

the self-energy of R due to loops of R'. These are shown in Fig. 4.1 and their contribution is the same as their single-representation counterparts [12] up to some group theory factors. The diagrams I_1 and I_2 in Fig. 4.1 must be evaluated together in order to be infrared finite. Their value is

$$I_1^R + I_2^R = n_f(R')4C_2(R)T_{R'}\, c_1^{(2)}, \tag{4.7}$$

where $c_1^{(2)} = 0.00079263(8)$ [95] is representation independent, and $n_f(R)$ is the number of fermions in the representation R. Similarly, $I_3 + I_4$ gives the infrared-finite result

$$I_3^R + I_4^R = n_f(R')4C_2(R)T_{R'}\, c_2^{(2)}\,, \tag{4.8}$$

where $c_2^{(2)} = 0.000393556(7)$. The two-loop part of the self energy for the representation R due to the presence of R' is then

$$\Sigma_{R'\to R}^{(2),\,\text{multi-rep}} = n_f(R')4C_2(R)T_{R'}\; 0.00118619(9)\;. \tag{4.9}$$

We then add to this contribution the 26 single-representation diagrams $\Sigma_{R\to R}^{(2),\,\text{one-rep}}$ [52]

$$\begin{aligned}\Sigma_{R\to R}^{(2),\,\text{one-rep}} = {} & C_2(R)N\,k_1 + 2C_2(R)T_R n_f(R)\,k_2 \\ & + C_2(R)C_2(\text{Fund})\,k_3 + C_2(R)^2\,k_4\;,\end{aligned} \tag{4.10}$$

with

$$\begin{aligned} k_1 &= -0.001940(6)\,, \qquad k_2 = 0.00237236(16)\,, \\ k_3 &= -0.081429(8)\;, \qquad k_4 = 0.01516325(12)\;. \end{aligned} \tag{4.11}$$

The total two-loop self energy is given by the sum of Eqs. (4.9) and (4.10)

$$\begin{aligned}\Sigma_R^{(2)} = {} & C_2(R)N\,k_1 + 2C_2(R)\left[T_R n_f(R) + T_{R'} n_f(R')\right]\,k_2 \\ & + C_2(R)C_2(\text{Fund})\,k_3 + C_2(R)^2\,k_4\;.\end{aligned} \tag{4.12}$$

Unsurprisingly if $R = R'$ the extra term is equivalent to the addition of extra flavor content.

We can now list results for $N = 4$, $n_f(\text{Fund}) = n_f(\text{2AS}) = 2$. One loop values,

$$\begin{aligned} \Sigma^{(1)}_{\text{Fund}} &= -0.610713970166(8)\,, \\ \Sigma^{(1)}_{\text{2AS}} &= -0.814285293555(10)\,, \end{aligned} \tag{4.13}$$

and two-loop values,

$$\begin{aligned} \Sigma^{(2)}_{\text{Fund}} &= -0.220826(53)\,, \\ \Sigma^{(2)}_{\text{2AS}} &= -0.270743(71)\,. \end{aligned} \tag{4.14}$$

We are interested, in particular, in the contributions from one representation to the other. These are

$$\begin{aligned} \Sigma^{(2),\,\text{multi-rep}}_{\text{2AS}\to\text{Fund}} &= 0.0213512(14)\,, \\ \Sigma^{(2),\,\text{multi-rep}}_{\text{Fund}\to\text{2AS}} &= 0.0355854(24)\,. \end{aligned} \tag{4.15}$$

The multi-rep contributions alone are small compared to the rest of the terms, providing about $10 - 13\%$ of the two-loop part. Although these results are only perturbative, they will find a non-perturbative counterpart in Sec. 4.4.

4.1.2 Critical mass

A perturbative prediction that compares to our numerical results can be obtained by including the clover term into the action, resulting into an additional interaction vertex. The prediction can be further improved by resumming an infinite series of a specific type of gauge invariant (*cactus*) diagrams [95]. For this analysis, we consider one-loop results.

The critical mass $m^{(1)}_{\text{c, R}}$ of Wilson fermions can be computed from Eq. (4.5). Considering the clover term yields new contributions in powers of c^R_{sw} [96],

$$m_{\text{c},\,R} = \frac{g_0^2 C_2(R)}{16\pi^2}\left(\epsilon_0 + \epsilon_1 c^R_{\text{sw}} + \epsilon_2 (c^R_{\text{sw}})^2\right)\,, \tag{4.16}$$

where the coefficients ϵ_i can be read from Table 2 of Ref. [96]. Concerning the Wilson term, the cactus resummation is performed by rescaling the self-energy $\Sigma \to \Sigma/\tilde{c}_0$, where $\tilde{c}_0$ is a function of N and g_0^2 but not of the representation.

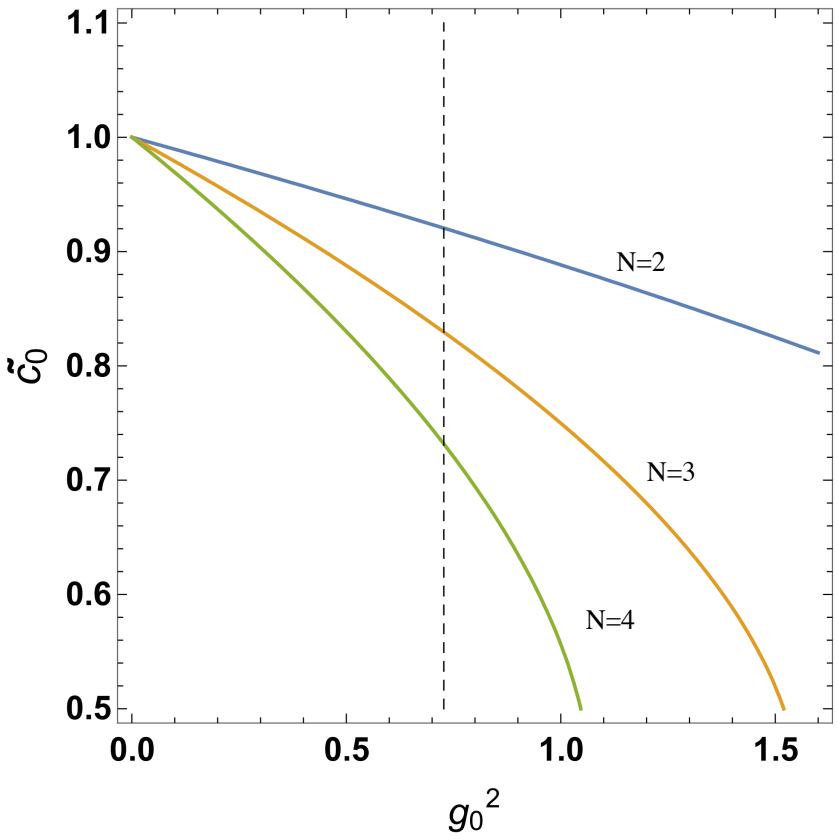

Figure 4.2 *The solution of Eq.* (4.17) *for different number of colors* $N = 2, 3, 4$ *and* $\beta = 11$*, the value used in the numerical simulations, as will be described in Sec. 4.2.*

$\tilde{c}_0$ can be found by solving the following equation,

$$\begin{aligned} & u e^{-u(N-1)/(2N)} \left[\frac{N-1}{N} L_{N-1}^{1}(u) + 2 L_{N-2}^{2}(u) \right] = \frac{g_0^2 (N^2-1)}{4} \, , \\ & \tilde{c}_0 \equiv \frac{g_0^2}{4u} \, , \end{aligned} \tag{4.17}$$

where L_N^α are generalised Laguerre polynomials of degree N. The solution for $\beta = 11$ and $N = 2, 3, 4$ is shown in Fig. 4.2 as the intersection between the various curves and the vertical line. For $SU(4)$ we find

$$\tilde{c}_0 = 0.731607 \, . \tag{4.18}$$

The resummation with the clover improvement term corresponds to rescaling $g_0^2 \to g_0^2/\tilde{c}_0$ and $c_{\rm sw}^R \to c_{\rm sw}^R \tilde{c}_0$ [97]. The prediction for the critical mass is then

$$m_{c,\,R}^{1-\text{loop+cactus}} = \frac{g_0^2}{\tilde{c}_0} \frac{C_2(R)}{16\pi^2} \left(\epsilon_0 + \epsilon_1 c_{\rm sw}^R \tilde{c}_0 + \epsilon_2 (c_{\rm sw}^R)^2 \tilde{c}_0^2 \right) \, . \tag{4.19}$$

The numerical values for $SU(4)$ with two fundamental and two antisymmetric fermions are listed in Table 4.1. We find the one-loop result with cactus resummation to be the closest one to non-perturbative results.

	Wilson (W)	W 2 loops	W clover	W+cactus	W clover+cactus
$am_c^{(\mathrm{Fund})}$	-0.4442	-0.5609	-0.2762	-0.6063	-0.4524
$am_c^{(\mathrm{2AS})}$	-0.5922	-0.8027	-0.3683	-0.8089	-0.6032

Table 4.1 *Critical masses for different lattice actions and improvements. When not specified, the results are obtained at 1 loop. These values are to be compared with the non-perturbative results of Sec. 4.4.*

4.2 Lattice Setup

The lattice setup has already been discussed in Ref. [13], and here we only recall the main ideas. We generate gauge configurations by using the HMC algorithm [88] with a second order integrator [98]. The integration scheme has two levels, one updating the gauge force and one updating the fermionic force. The lattice action can be decomposed into gauge and fermionic part. The latter is further decomposed into contributions from each representation [94]

$$S = S_{\mathrm{g}} + S_{\mathrm{f}} \ , \qquad S_{\mathrm{f}} = S^{(\mathrm{Fund})} + S^{(\mathrm{2AS})} \ . \tag{4.20}$$

For the gauge part we use the Wilson plaquette action

$$S_{\mathrm{g}} = \frac{\beta}{N_c} \sum_x \sum_{\mu<\nu} \mathrm{Re\ Tr} \left\{ 1 - \mathcal{P}_{\mu\nu}(x) \right\} \ . \tag{4.21}$$

The fermionic action for the representation R is

$$S_{\mathrm{f}}^R = \sum_x \bar{\psi}^R(x)\, D^R_{x,y}\, \psi(x)^R \ , \tag{4.22}$$

where, for both representations, we collect the fermionic degrees of freedom into a doublet of Dirac fermions ψ^R. We adopt a Wilson discretisation for the Dirac action D^R in each representation R, plus a clover improvement term

$$D^R = D^R_{\mathrm{Wilson}} + D^R_{\mathrm{clover}} \ . \tag{4.23}$$

The Wilson term in position space is

$$D^R_{x,y} = \delta_{x,y} - \kappa^R \sum_{\mu=1}^{4} \big[(\mathbb{1} - \gamma_\mu)\, U^R_\mu(x) \delta_{x+a\hat{\mu},y} + (\mathbb{1} + \gamma_\mu)\, U^{R\,\dagger}_\mu(y) \delta_{x-a\hat{\mu},y} \big] \ , \quad (4.24)$$

where

$$U^R_\mu(x) = \exp(i\, \omega^a_\mu(x)\, T^R_a) \ , \quad (4.25)$$

and κ^R is related to the bare mass m^R_0 of the fermion in the representation R,

$$\kappa^R = \frac{1}{2(am^R_0 + 4)} \ . \quad (4.26)$$

The order a clover improvement term is

$$\left(D^R_{\text{clover}}\right)_{x,y} = \frac{ia}{2}\, c^R_{\text{sw}}(g_0^2)\, \kappa^R \sum_{\mu\nu} \tilde{F}^R_{\mu\nu}(x)\, \sigma_{\mu\nu} \delta_{x,y} \ , \quad (4.27)$$

where $\sigma_{\mu\nu} = \frac{i}{2}[\gamma_\mu, \gamma_\nu]$ and

$$\tilde{F}_{\mu\nu}(x) = \frac{1}{8} \left[Q_{\mu\nu}(x) - Q_{\nu\mu}(x) \right] \ , \qquad Q_{\mu\nu}(x) = Q^\dagger_{\nu\mu}(x) \ , \quad (4.28)$$

$Q_{\mu\nu}(x)$ being the clover combination of plaquettes around the point x [17]. The improvement coefficient c^R_{sw} can be computed in powers of the coupling,

$$c^R_{\text{sw}}(g_0^2) = 1 + c^{R\,(1)}_{\text{sw}}\, g_0^2 + \mathcal{O}(g_0^4) \ . \quad (4.29)$$

A discussion on the $O(g_0^2)$ coefficient can be found in [99]. In this work, we set the coefficient to its tree level value, $c^R_{\text{sw}} = 1$, for both representations. This choice for the discretisation action breaks explicitly chiral symmetry, resulting in an additive term to the renormalisation of the fermion masses. Simulations at the chiral point are performed indirectly by extrapolating the observables. The critical masses m^R_{c}, i.e. the value of the bare masses at which each fermion has a renormalised vanishing mass

$$am^R = am^R_0 - am^R_{\text{c}} = \frac{1}{2} \left(\frac{1}{\kappa^R} - \frac{1}{\kappa^R_{\text{c}}} \right) \ . \quad (4.30)$$

Direct simulations at the chiral point are in fact impossible in our setup due to the spectral properties of the Dirac operator. The lowest eigenvalue of

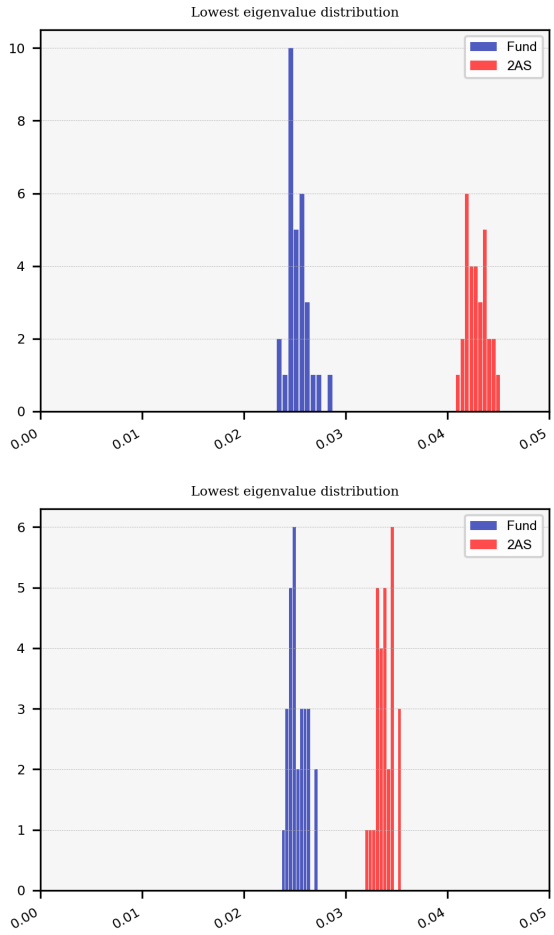

Figure 4.3 *Distribution of the lowest eigenvalue of the Wilson-clover operator for bare parameters* $am_0^{(\mathrm{Fund})} = -0.45$, $\beta = 11$ *and different masses for the 2AS fermions:* $am_0^{(\mathrm{2AS})} = -0.59$ *on the top and* $am_0^{(\mathrm{2AS})} = -0.60$ *on the bottom. Both distributions are far enough from the origin to ensure no exceptional configurations enter the ensemble.*

the Dirac operator approaches zero in the chiral limit, meaning its inverse becomes increasingly ill-conditioned. When extrapolating to the critical point (see Eq. (4.30)) one needs to care that exceptional configurations do not occur in the gauge average [100]. These are configurations with exceptionally small eigenvalues that can jeopardise the inversion of the fermionic operator. For this reason, we monitor the gauge distribution of the lowest eigenvalues of the Wilson-clover operators in both representations as in Fig. 4.3, making sure that they remain sufficiently far from the origin. In order to parametrise the breaking of chiral symmetry, we compute the PCAC mass, which yields a definition of the quark mass through the axial Ward identity.

Our starting point is the work done in [13], where the space of bare parameters for this model has been explored. The lightest ensemble of that work is present in this analysis under the name A0. Details about the ensembles generated in this work are found in C.3. We have performed simulations for increasingly lighter masses, allowing the extrapolation of chiral points for both the fermionic representations. We generate gauge configurations at single lattice spacing, using $\beta = 11$, and at a single volume corresponding to a lattice of dimensions $(L/a)^3 \times T/a = 16^3 \times 32$. For the production of gauge configurations and the measurements of observables, we use the software Grid [55] and Hadrons [101].

4.3 Observables

In this section, we give a description of the observables that are targeted in this work. These include two point functions that will enable us to compute parameters for the chiral symmetry breaking, mesonic masses and smeared spectral densities. We compute correlation functions of the following interpolators,

$$\begin{aligned} O^R_{\mathrm{P}}(x) &= \bar{\psi}^R_{f_1}(x)\,\gamma_5\,\psi^R_{f_2}(x)\,, \\ O^R_{\mathrm{A}}(x) &= \bar{\psi}^R_{f_1}(x)\,\gamma_0\gamma_5\,\psi^R_{f_2}(x)\,, \qquad\qquad f_1 \neq f_2\,. \end{aligned} \tag{4.31}$$

In the previous equation we use the same notation of Sec. 4.2, i.e. ψ^R collects the fermionic degrees of freedom of the representation R into a flavor doublet of Dirac spinors. The flavor indices are denoted by f_1, f_2. In this work we only consider isospin-vector operators, and we build the following two-point functions

$$C^R_{ab}(t) = \frac{1}{L^3}\sum_{\boldsymbol{x}} \langle O^R_a(\boldsymbol{x},t) O^{R^\dagger}_b(0)\rangle \;, \qquad a,b = \mathrm{P},\mathrm{A}\,. \tag{4.32}$$

The two-point functions encode information about finite volume matrix elements and energy levels. This can be seen by expanding the previous expression on a complete set of states. Considering for instance the pseudoscalar-

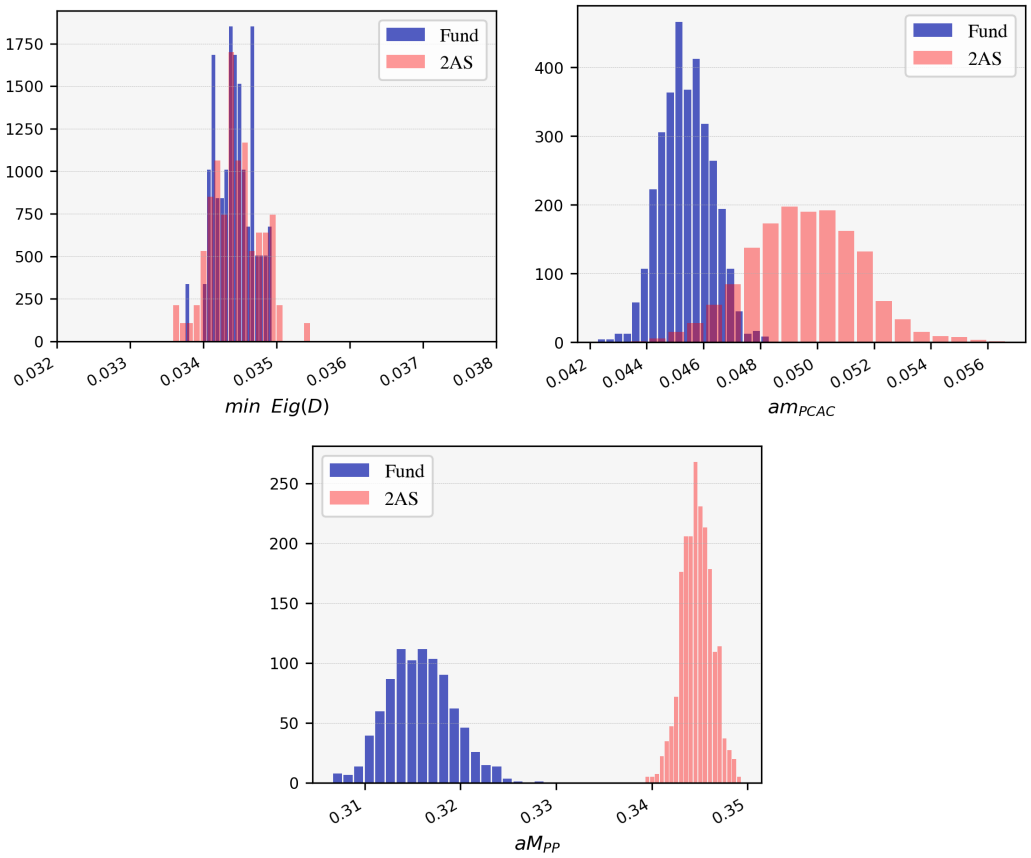

Figure 4.4 *Probability densities for the lowest eigenvalue of the fermionic operator (upper panel), the PCAC mass (central panel) and the pseudoscalar mass (lower panel) for both representations. These values are especially interesting since they are based on the ensemble S0, where we find compatible values for the lowest eigenvalues and, within* 1σ*, the PCAC masses. Nonetheless, a difference arises in the pseudoscalar masses. The distributions of the PCAC and the pseudoscalar masses are obtained from a resampled set of configurations.*

pseudoscalar correlator, we obtain

$$C^R_{PP}(t) = \left(e^{-tM^R_{PP}} + e^{(-T+t)M^R_{PP}}\right) \times \frac{\langle 0|O^R_P(0)|M^R_{PP}\rangle_L \langle M^R_{PP}|O^{R\dagger}_P(0)|0\rangle_L}{2M^R_{PP}} + \dots \,, \quad (4.33)$$

where the ellipsis denotes terms that do not correspond to the state $|M^R_{PP}\rangle_L$ and that are exponentially suppressed. The mass M^R_{PP} can be then obtained

by the asymptotic behaviour in the Euclidean time of the effective mass

$$aM_{\mathrm{PP}}^{R}(t) = \cosh^{-1}\left[\frac{C_{\mathrm{PP}}^{R}(t+a) + C_{\mathrm{PP}}^{R}(t-a)}{2C_{\mathrm{PP}}^{R}(t)}\right] . \tag{4.34}$$

Similarly the PCAC mass, defined through the axial Ward identity, is obtained from the pseudoscalar-pseudoscalar and axial correlators

$$m_{\mathrm{PCAC}}^{R} = \frac{\nabla_t C_{\mathrm{AP}}^{R}(t)}{2C_{\mathrm{PP}}^{R}} , \qquad \nabla_t f(t) = \frac{f(t+a) - f(t-a)}{2a} , \tag{4.35}$$

which has $\mathcal{O}(a)$ effects for our choice of the unimproved axial operator.

In the chiral limit, the pseudoscalar mass aM_{PP}^{R} for each representation vanishes. In our ensembles we generated configurations describing mesons of antisymmetric fermions being generally heavier: this can be understood from Fig. 4.4 where we show the gauge distributions of the lowest eigenvalue of the fermionic operator, the fermionic masses and the pseudoscalar masses for both representations from the ensemble $S0$. In this ensemble, differently from the case shown in Fig 4.3, the lowest eigenvalues of the Wilson operators in the two representations are the same, and the fermionic masses are also compatible within one σ. Nonetheless, an unambiguous gap appears in the masses of the mesons. The Gell-Mann–Oakes–Renner relation predicts this behaviour to be the result of different chiral condensates and pseudoscalar decay constants for the two representations.

Ground state energies can be estimated from lattice correlators according to the large time behaviour of Eq. (4.34). Other energy levels and matrix elements can be estimated by fitting sums of exponentials, as in Eq. (4.33). The extraction of excited states from these fits is in general hindered by the increasing number of degrees of freedom that are needed in order to perform the fit when more excited states are being targeted, with a given number of data points. This becomes particularly problematic when dealing with highly correlated data, which limits the information provided. Moreover, as the infinite volume limit is approached, the spectrum above the multi-particle threshold becomes denser and resolving energy levels becomes exponentially harder. For these reasons, it is desirable to have many correlators in order to perform simultaneous fits. Alternatively, variational methods such as the generalised eigenvalue problem (GEVP) are a well established way to obtain finite volume spectra [102].

Other observables that allow the extraction of finite volume energies and matrix elements are spectral densities. These are related to lattice correlators by a Laplace transform

$$C_{PP}^{R}(t) = \int_0^\infty dE\, \rho_{PP}^{R}(E)\, \left(e^{-tE} + e^{(-T+t)E}\right) \ , \tag{4.36}$$

where we neglect the thermal effects inside $\rho_{PP}^{R}(E)$.[1] Spectral densities contain the same information as lattice correlators, with the difference that for the spectral densities the information is encoded in a function of the energy rather than Euclidean time. A finite volume spectral density $\rho_{ab}^{L}(E)$ can in fact be expanded as

$$\rho_{PP}^{L,R}(E) = \sum_n \frac{\langle 0|O_P^R(0)|n\rangle_L \, \langle n|O_P^{R^\dagger}(0)|0\rangle_L}{2E_n(L)}\, \delta\left(E - E_n(L)\right) \ . \tag{4.37}$$

In order to cope with the distributional nature of the spectral density, we smear it [104] with a Gaussian function, $\Delta_\sigma(E) = \exp\left(-E^2/2\sigma^2\right)/\sqrt{2\pi}\sigma$

$$\rho_{\sigma,PP}^{L,R}(E) = \int_0^\infty dE'\, \Delta_\sigma(E - E')\, \rho_{PP}^{L,R}(E') \ , \tag{4.38}$$

so that the smeared spectral density $\rho_{\sigma,ab}^{L,R}(E)$ is a continuous function even at finite L.

In this work, we will focus on the extraction of the finite volume energies and matrix elements from smeared spectral densities. This task does not require us to take the infinite volume limit, neither to remove the regularisation by extrapolating at zero smearing radius σ. By rewriting Eq. (4.37) for the smeared spectral density,

$$\rho_{\sigma,PP}^{L,R}(E) = \sum_n \frac{\langle 0|O_P^R(0)|n\rangle_L \, \langle n|O_P^{R^\dagger}(0)|0\rangle_L}{2E_n(L)}\, \Delta_\sigma\left(E - E_n(L)\right) \ , \tag{4.39}$$

it is clear that this function can be fitted against sums of Gaussians in order to obtain the energies and the overlaps, similarly to how Eq. (4.33) is commonly used to extract the same quantities by fitting sums of exponentials. This offers a dual picture with quite different features that will be described in the next sections.

[1] In Sec. 3 of Ref. [103] is shown that Eq. (4.36) is valid up to thermal effects in $\rho_{PP}^{R}(E)$ that are exponentially suppressed, and that we neglect in our discussion.

4.4 Chiral Limit

At the chiral point, both pseudoscalar mesons become massless. The discretisation of the lattice action that we adopt breaks chiral symmetry explicitly. We therefore compute the PCAC masses from the axial Ward identity in order to quantify the breaking of chiral symmetry, and we scan the space of bare parameters until we are able to locate the bare masses for which the PCAC masses vanish. Around the chiral point we also expect the Gell-Man–Oakes–Renner relation to be valid, with the pseudoscalar mass squared $(M^R_{\rm PP})^2$ scaling as $m^R_{\rm PCAC}$ for the representation R. The correlation functions of fermions in the fundamental representation that we use to extract the masses are more affected by autocorrelation, which translates into usually larger statistical errors for the masses of the mesons related to that representation. The measurements of the PCAC masses are listed in Tables C.2 and C.3 of C.4. In order to perform a linear extrapolation for the vanishing of the PCAC mass in a given representation, the bare mass of the other must be kept fixed. Fig. 4.5 shows three of these extrapolations. In the top panel, we extrapolate the chiral point for the fundamental fermions by fixing $am_0^{(\rm 2AS)} = -0.45$. In the bottom panel, the two lines represent different extrapolations for the 2AS chiral point taken at different values of the bare fundamental mass, $am_0^{(\rm Fund)} = -0.45$ and $am_0^{(\rm Fund)} = -0.47$. The chiral point of antisymmetric fermions does not show a strong response to the shift in the bare mass of the fundamental fermions. This is in line with the perturbative prediction at two loops of Sec. 4.1, where we have found the critical mass to only mildly depend on the other representation. The critical masses for $\beta = 11.0$ are

$$\begin{aligned} am_{\rm c}^{(\rm Fund)}\Big|_{am_0^{(\rm 2AS)}=-0.45} &= -0.486(3)\ , \\ am_{\rm c}^{(2AS)}\Big|_{am_0^{(\rm Fund)}=-0.45} &= -0.637(3)\ , \\ am_{\rm c}^{(\rm 2AS)}\Big|_{am_0^{(\rm Fund)}=-0.47} &= -0.630(4)\ . \end{aligned} \tag{4.40}$$

Comparing these values to the perturbative results in Table 4.1, we see that the prediction improved by resumming cactus diagrams is the closest to the non-perturbative values. We can also observe from Tables C.2 and C.3 that taking a fermion in the representation R towards the chiral point pushes the fermion in the representation R' to be also lighter. Figure 4.6 shows the dependence

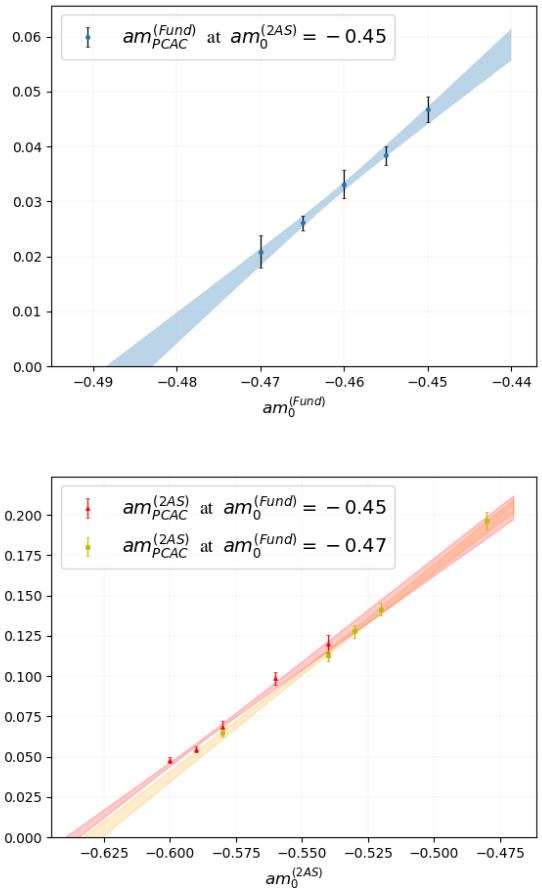

Figure 4.5 *Three chiral extrapolations, one on the top for fundamental fermions and two on the bottom for antisymmetric fermions. The bands correspond to linear fits. The heavier point in the plot on the top was also present in [13]. In the top panel, the fit has* $\chi^2/d.o.f. = 0.23$*. In the bottom panel,* $\chi^2/d.o.f. = 2.22$ *for* $am_0^{(\mathrm{Fund})} = -0.45$ *and* $\chi^2/d.o.f. = 0.48$ *for* $am_0^{(\mathrm{Fund})} = -0.47$

of the pseudoscalar masses M_{PP}^R with respect to the quark masses. For both representations R the scaling is compatible with the one predicted by the chiral Lagrangians, $(M_{\mathrm{PP}}^R)^2 \sim m_{\mathrm{PCAC}}^R$, with the pseudoscalar mesons becoming massless in the chiral limit. The pseudoscalar masses, reported in Table C.4, are obtained by fitting the effective masses of the pseudoscalar-pseudoscalar correlators.

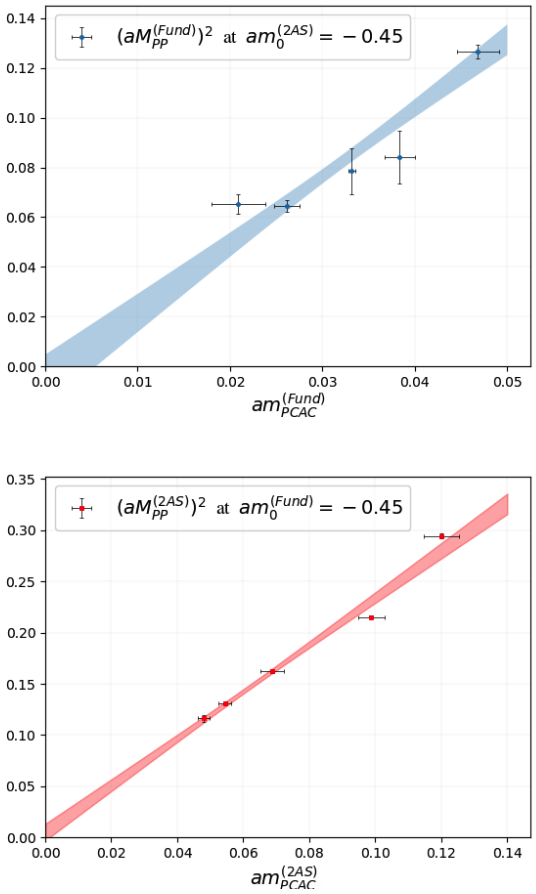

Figure 4.6 *Scaling predicted by the Gell-Man–Oakes–Renner relation, with the squared mass of the pseudoscalar Goldstone boson scaling linearly with the quark mass, here estimated from the PCAC relation. The extrapolation is compatible with the Goldstone bosons becoming massless at the chiral point. In the top panel, the fit has* $\chi^2/d.o.f. = 1.68$*, while in the bottom panel* $\chi^2/d.o.f. = 1.50$*.*

4.5 Smeared Spectral Densities from Lattice Correlators

The non-perturbative calculation of spectral densities has been receiving increasing attention [103–109]. In this work we will analyse spectral densities obtained from lattice correlators, for the first time to our knowledge, in the context of BSM and multi-representation theories. In order to facilitate the discussion, it is useful to recall the computational details of the calculation, aiming to a self-contained discussion.

4.5.1 The numerical procedure

Since we are interested in finite volume energies we will omit, in this section, the dependence on the spatial volume L that we will assume to be finite. Computing the spectral density $\rho^R_{PP}(E)$ from the Euclidean correlator $C^R_{PP}(t)$ involves the inversion of the Laplace transform,

$$C^R_{PP}(t) = \int_{E_{\min}}^{\infty} dE \, \left(e^{-tE} + e^{(-T+t)E}\right) \, \rho^R_{PP}(E) \, , \tag{4.41}$$

where $E_{\min}$ can range between zero and the energy of the ground state, since ρ^R_{PP} vanishes in that interval. The inversion of Eq. (4.41) is in this context an ill-posed problem which needs to be regularised. Recalling from Sec. 4.3 that we are interested in the smeared version of $\rho^R_{PP}(E)$, it is especially convenient to approach the inverse problem using the Backus–Gilbert type regularisation [110] introduced in [105], which yields spectral densities smeared with a chosen smearing function $f(E)$,

$$\rho^R_{PP}[f] = \int_0^{\infty} dE \, f(E) \, \rho^R_{PP}(E) \, . \tag{4.42}$$

An important observation is that a fixed smearing kernel is crucial in order to perform fits and extrapolations of the results. The idea of the algorithm is to generate the target smearing kernel, the Gaussian $\Delta_\sigma(E)$ of Eq. (4.38), as a linear combination of the same exponentials appearing in the Laplace transform of Eq. (4.41),

$$\Delta_\sigma(E - E') = \sum_{\tau=1}^{\infty} g_\tau \, \left(e^{-\tau a E} + e^{(-T+a\tau)E}\right) \, , \tag{4.43}$$

where $t = \tau a$, a being the lattice spacing. Once the coefficients $g_\tau \equiv g_\tau(\sigma, E')$ are known one can simply obtain an estimator for the smeared spectral density,

$$\rho^R_{PP,\,\sigma}(E') = \sum_{\tau=1}^{\infty} g_\tau \, C^R_{PP}(a\tau) \, . \tag{4.44}$$

On the lattice the correlators C^R_{PP} are available for a finite number of times, therefore the sum in Eqs. (4.43) and (4.44) must be truncated at the appropriate cutoff $\tau_{\max}$. Since our lattices have temporal length T and periodic

boundaries, we have $a\tau_{\max} = T/2$. The reconstructed smearing kernel,

$$f(E, \boldsymbol{g}) = \sum_{\tau=1}^{\tau_{\max}} g_\tau \left(e^{-\tau a E} + e^{(-T+a\tau)E} \right) , \tag{4.45}$$

will necessarily differ from the Gaussian $\Delta_\sigma(E)$ at finite $\tau_{\max}$, inducing a systematic error on the final result. The computation of the coefficients $\boldsymbol{g}$ is achieved through the minimisation of the functional $W_\alpha[\boldsymbol{g}]$

$$W_\alpha[\boldsymbol{g}] = \frac{A_\alpha[\boldsymbol{g}]}{A_\alpha[0]} + \lambda\, B[\boldsymbol{g}] , \tag{4.46}$$

where λ is a trade-off input parameter that we will discuss later in this section. The functional $A_\alpha[\boldsymbol{g}]$, introduced in [105], measures the difference between the exact smearing kernel and the one we can reconstruct with the available data

$$A_\alpha[\boldsymbol{g}] = \int_{E_{\min}}^{\infty} dE\, e^{\alpha a E} \left| f(E, \boldsymbol{g}) - \Delta_\sigma(E - E') \right|^2 . \tag{4.47}$$

The parameter $\alpha < 2$ enables the selection between a class of norms in order to measure the distance between the target and the exact function. Choosing larger values of α allows for the integrand to decay faster at high energies. The functional $B[\boldsymbol{g}]$ is needed to regularise the problem [110], making it numerically stable. We define $B[\boldsymbol{g}]$ to be dimensionless, namely

$$B[\boldsymbol{g}] = \frac{E^2}{C_{PP}^R(a)^2} \sum_{\tau,\tau'=1}^{\tau_{\max}} g_\tau \, \mathrm{Cov}_{\tau\tau'} \, g_{\tau'} , \tag{4.48}$$

where Cov is the covariance matrix of the correlator $C(a\tau)$ estimated over N bins (see C.1),

$$\begin{aligned} C(a\tau) &= \frac{1}{N} \sum_{n=0}^{N-1} C_n(a\tau) , \\ \mathrm{Cov}_{\tau\tau'}[C] &= \frac{1}{N-1} \sum_{n=0}^{N-1} \left[C_n(a\tau) - C(a\tau) \right] \left[C_n(a\tau') - C(a\tau') \right] . \end{aligned} \tag{4.49}$$

The algorithmic parameters can be gathered to simplify the notation

$$\boldsymbol{p} = (\alpha, \lambda, E_{\min}, \tau_{\max}) . \tag{4.50}$$

The minimisation of $W_\alpha[\boldsymbol{g}]$ corresponds to solving the following linear problem,

$$\left.\frac{\delta W_\alpha[\boldsymbol{g}]}{\delta g_\tau}\right|_{\boldsymbol{g}=\boldsymbol{g^p}} = 0 \,, \tag{4.51}$$

which has to be performed at each energy and smearing radius for which we want to estimate $\rho^R_{PP,\,\sigma}(E')$. The nature of the functionals appearing in these definitions is intimately related to the uncertainties on the estimator $\rho^R_{PP,\,\sigma}(E')$. The statistical error is in fact estimated by

$$\Delta_{\rm stat}(E', \boldsymbol{g^p}) = \frac{C^R_{ab}(1)}{E'}\sqrt{B[\boldsymbol{g^p}]} \,. \tag{4.52}$$

The systematic error, unavoidable at finite τ_{max}, is estimated by monitoring the quantity

$$d(\boldsymbol{g^p}) = \sqrt{\frac{A_0[\boldsymbol{g^p}]}{A_0[\boldsymbol{0}]}} \,, \tag{4.53}$$

as we now describe. Regions where $d(\boldsymbol{g^p})$ is small are dominated by the statistical uncertainty; on the other hand, the reconstructed smearing function of Eq. (4.43) will be as close as possible to the exact one. For these reasons, it is not surprising that where $d(\boldsymbol{g^p})$ is small, the results for $\rho^R_{PP,\,\sigma}$ are stable[2] in response to variations of the algorithmical, unphysical parameters $\boldsymbol{p}$, within statistical error, see for instance Fig. 4.7. If we define the coefficients $\boldsymbol{g^\star}$ as

$$A_\alpha[\boldsymbol{g^\star}]/A_\alpha[\boldsymbol{0}] = k\; B[\boldsymbol{g^\star}] \,, \tag{4.54}$$

we find, with the given normalisations of the functionals and with the quality of our data, that in the range $0.1 < k < 5$ and $\alpha = 1$ the outcome of the reconstruction is in a region of algorithmical stability: $d(\boldsymbol{g^p})$ is small, and systematic fluctuations are well within the statistical uncertainty. When this is not realised, the systematic error is estimated as

$$\Delta_{\rm sys}(E') = |\rho^R_{PP,\,\sigma}(E', \boldsymbol{g^\star}) - \rho^R_{PP,\,\sigma}(E', \boldsymbol{g^{\star\star}})| \,, \tag{4.55}$$

where $\boldsymbol{g^{\star\star}}$ is defined through Eq. (4.54) at a different value of k that allows us to account for the systematic fluctuations. In this work, we find that a definition of $g^{\star\star}$ at $k/10$ provides a conservative estimate of $\Delta_{\rm sys}(E')$ for a reconstruction performed with $g^\star$ at the value k. Fig. 4.7 shows an example, for a specific

[2]Ref. [105] shows that, with the value of $\tau_{\rm max}$ used in this work, we can expect a well reconstructed smearing kernel, at vanishing λ.

energy $E_\star$, of a stability regime where the spectral reconstruction for different values of λ (black points) does not fluctuate outside the statistical error (black bars). Three points on the plot are highlighted: the ones corresponding to the choices of $k = 0.1$, $k = 2.5$ and $k = 1$ in Eq. (4.54), showing that indeed no systematic component affects the uncertainty on the result. The value corresponding to $k = 1$ is associated to the value of λ at which one achieves the optimal balance $A_\alpha[\boldsymbol{g}^\star]/A_\alpha[\mathbf{0}] = B[\boldsymbol{g}^\star]$, in agreement with the prescription from Refs. [103, 105].

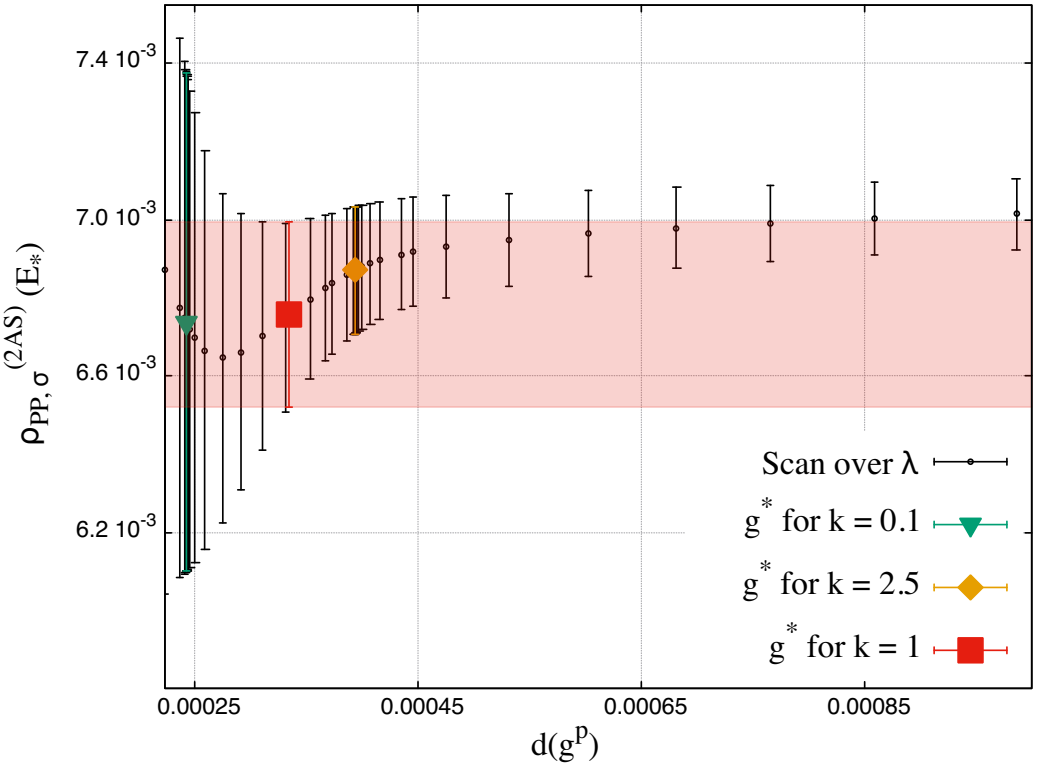

Figure 4.7 *Example of region of algorithmical stability at a given energy $E_\star$. Different values of λ, which translate into different values of $d(\boldsymbol{g}^{\boldsymbol{p}})$ on the x-axis, produce predictions for the smeared spectral density $\rho^R_{PP,\sigma}(E_\star)$ that are compatible within statistical error (black bars). In this case, R = 2AS, $\sigma = 0.21/a$ and $E_\star \simeq M^{(2\mathrm{AS})}_{\mathrm{PP}}$. The green and orange points correspond, according to Eq. (4.54), to values of $k = 0.1$ and $k = 2.5$ respectively. The red point, extended in the horizontal band, is obtained at $k = 1$ and it corresponds to the value of λ at which one achieves the optimal balance $A_\alpha[\boldsymbol{g}^\star]/A_\alpha[\mathbf{0}] = B[\boldsymbol{g}^\star]$.*

4.5.2 Excited states in the antisymmetric sector

The excited states created by hadronic interpolators have a big impact on the extraction of the effective masses, since it can be hard to distinguish them from the ground state. In theories with multiple representations (or even just more flavors of a single representation) this effect is amplified when all the fermions are approaching the chiral limit. An interpolator can now create states containing particles from both representations. Since we simulate lighter fundamental fermions, we can expect this feature to be more visible in the 2AS sectors rather the in the fundamental one. Moreover, the 2AS sector does not have G-parity selection rules preventing certain states to mix, and we thus expect this channel to have a richer dynamics. In order to go into more details, it is useful to set the notation for the pseudoscalar interpolators of Eq. (4.31)

$$\begin{aligned} \hat{\pi}(x) &= \bar{\psi}_{f_1}^{(\mathrm{Fund})}(x)\gamma_5\ \psi_{f_2}^{(\mathrm{Fund})}(x)\ , \\ \hat{\Pi}(x) &= \bar{\psi}_{f_1}^{(\mathrm{2AS})}(x)\gamma_5\,\psi_{f_2}^{(\mathrm{2AS})}(x)\ , \qquad f_1 \neq f_2\ , \end{aligned} \tag{4.56}$$

and the correlation functions

$$\begin{aligned} C_{\mathrm{PP}}^{(\mathrm{Fund})}(t) &= \frac{1}{L^3}\sum_{\boldsymbol{x}} \langle \hat{\pi}(\boldsymbol{x},t)\hat{\pi}^\dagger(0)\rangle\ , \\ C_{\mathrm{PP}}^{(\mathrm{2AS})}(t) &= \frac{1}{L^3}\sum_{\boldsymbol{x}} \langle \hat{\Pi}(\boldsymbol{x},t)\hat{\Pi}^\dagger(0)\rangle\ . \end{aligned} \tag{4.57}$$

The importance of both identifying and controlling the excited states can be appreciated by looking at the smeared spectral density, for instance, in the pseudoscalar channel

$$\rho_{\sigma,PP}^{L,R}(E) = \sum_n \frac{\langle 0|O_{\mathrm{P}}^R(0)|n\rangle_L \langle n|O_{\mathrm{P}}^{R^\dagger}(0)|0\rangle_L}{2E_n(L)}\,\Delta_\sigma\left(E - E_n(L)\right)\ . \tag{4.58}$$

The magnitude of each matrix element $\langle n|\bar{O}_{\mathrm{P}}^R(0)|0\rangle_L$ determines the weight of each Gaussian Δ_σ located at the energy $E_n(L)$. If these energies are too close, or the matrix elements are too large, resolving different states can become laborious. With this motivation, in order to control the excited states we build correlation functions including two different types of fermionic field: local, point-like operators and Gaussian-smeared ones[3]. Operator smearing allows working with interpolating operators that have a weaker overlap with excited

[3]Operator smearing is not to be confused with the smearing of spectral densities.

states. Details concerning the measurements of the correlation functions and operator smearing can be found in C.1.

The states created by each operator can be identified, as we have seen, by means of its symmetries. In the fundamental sector, at zero angular momentum, a pseudoscalar meson can induce the following transitions from the vacuum

$$\langle 0|\hat{\pi}|\pi\rangle \ , \quad \langle 0|\hat{\pi}|\pi\pi\pi\rangle \ , \quad \langle 0|\hat{\pi}|\pi\Pi\Pi\rangle \ , \ldots \tag{4.59}$$

that will enter in our analysis through Eq. (4.58). Since in our simulations $M_{\mathrm{PP}}^{(\mathrm{2AS})} > M_{\mathrm{PP}}^{(\mathrm{Fund})}$ this phenomenology is reminiscent, up to $E_{3\pi}$, of QCD, and one can expect computational aspects to be also similar. Conversely, due to the triviality of its G-parity, the 2AS sector has a multi-particle threshold located at $E_{2\Pi}$. In addition, since the other representation has lighter particles, states containing pseudoscalar mesons from the fundamental sector are not guaranteed to have energies far from the ground state. Possible overlaps with a pseudoscalar meson are in fact

$$\langle 0|\hat{\Pi}|\Pi\rangle \ , \quad \langle 0|\hat{\Pi}|\Pi\,\Pi\rangle \, , \quad \langle 0|\hat{\Pi}|\Pi\pi\pi\rangle \ , \quad \langle 0|\hat{\Pi}|\Pi\pi\pi\pi\pi\rangle \ , \ldots \tag{4.60}$$

The aforementioned features complicate the extraction of $M_{\mathrm{PP}}^{(\mathrm{2AS})}$, as it can be understood from Fig. 4.8 where we show two different types of signal from a correlator built with local, unsmeared operators. The excited states contaminate the signal for the ground state resulting, in the left panel, in an effective mass that does not reach a clear plateau. The problem is also manifest in the energy picture, as it is shown in the right panel of the same figure, where the smeared spectral density $\hat{\rho}_{\mathrm{PP},\sigma}^{(\mathrm{2AS})}$ does not exhibit the expected Gaussian peak around the mass of the pseudoscalar meson, but it rather grows monotonically. Indeed, by decreasing the smearing radius σ of Eq. (4.38) one should be able to resolve such peak, but this cannot be realised with the current quality of the data. While the temporal length of the lattice poses an intrinsic obstacle to the thermalisation of the effective mass, the spectral reconstruction in principle allows obtaining smaller smearing radii also by increasing the number of configurations, since the systematic and the statistical error are related by Eq. (4.46).

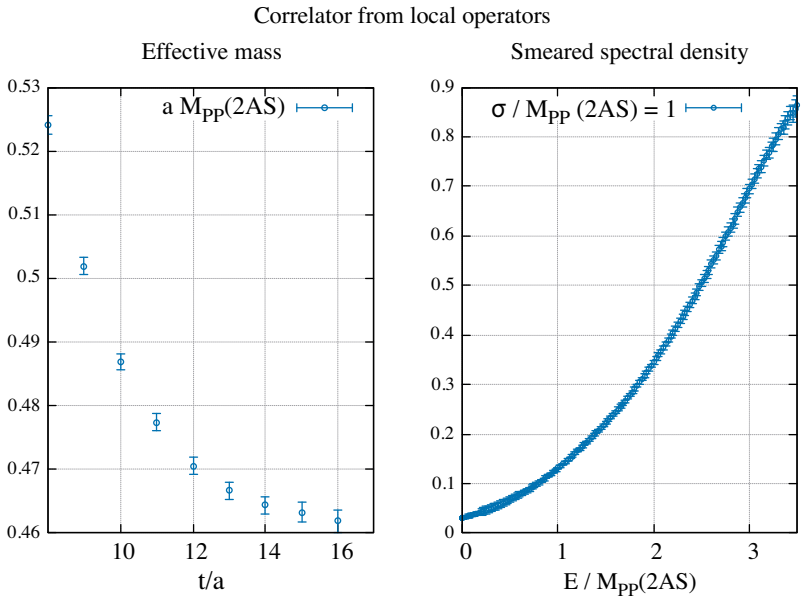

Figure 4.8 *Results from a two point function of pseudoscalar operators built with point-like antisymmetric fermionic fields. The correlator is estimated from the ensemble B1. The left panel exhibits the effective mass as a function of time. Due to the nature of the excited states in the 2AS sector, the mass does not reach a plateau in the available time. The dominance of the excited states can also be understood from the smeared spectral density in the right panel. The overlap between the interpolator and the excited states it creates is too large: the spectral density smeared according to Eq.* (4.38) *is dominated by contributions above the multi-particle threshold, preventing the identification of the ground state.*

Having established that the excited states present a challenge in the 2AS sector, it is natural to look at correlation functions of smeared operators defined in C.1, which have suppressed overlap with the excited states. Fig. 4.9 shows the effective mass and the spectral reconstruction from the correlation function of such operators. On the left panel, the plateau in the effective mass shows an improvement compared to the corresponding result in Fig. 4.8. The effective mass is independent of time, within its statistical errors, for $t/a > 10$. The smeared spectral density, shown in the right panel, demonstrates again the suppression of the excited states, with contributions from higher-energy states becoming smaller. As a result, a single peak is clearly visible at $E \simeq 2M_{\mathrm{PP}}^{(2\mathrm{AS})}$. The observed smeared spectral density is the result of two contributions coming mainly from the energy levels $M_{\mathrm{PP}}^{(2\mathrm{AS})}$ and $E_{\Pi\Pi} \simeq 2M_{\mathrm{PP}}^{(2\mathrm{AS})}$, which cannot be resolved because the smearing radius is too large, $\sigma \simeq M_{\mathrm{PP}}^{(2\mathrm{AS})}$. These energies can be nonetheless estimated by fitting the spectral density to a sum

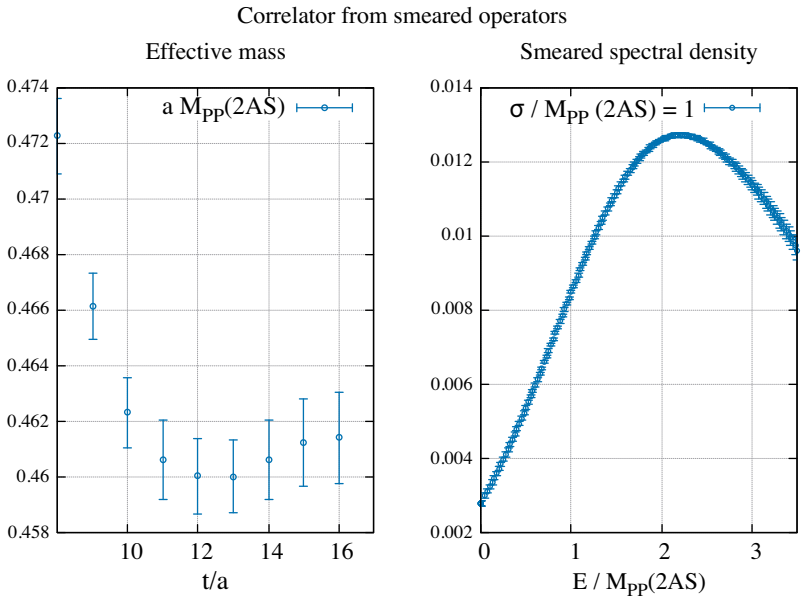

Figure 4.9 *Results from Fig. 4.8, this time using Gaussian-smeared interpolators according to C.1. These operators are tuned to have smaller overlaps with the excited states. Consequently, the effective mass plot on the left reaches a plateau, providing an estimate for* $aM_{\mathrm{PP}}^{(2\mathrm{AS})}$*. The right panel similarly shows how suppressed excited states allow for a clear peak to emerge in the spectral reconstruction smeared with* $\sigma = M_{\mathrm{PP}}^{(2\mathrm{AS})}$ *according to Eq.* (4.38)*. The peak includes contributions from mainly* M_{Π} *and* $E_{\Pi\Pi}$*.*

of Gaussians. This idea will be expanded in the next section.

4.5.3 Fits of spectral densities

In this section we describe fit strategies for spectral densities. A parallel discussion on fits of correlators will highlight the differences between the two methodologies and will lead to a quantitative comparison between predictions for the pseudoscalar masses obtained from the two approaches, which is presented in detail at the end of the section. The model functions used in the fits are $g^{(k)}(t)$ for correlators and $f_\sigma^{(k)}(t)$ for the smeared spectral densities

$$\begin{aligned} g^{(k)}(t) &= \sum_{n=1}^{k} a_n \left(e^{-tE_n} + e^{(-T+t)E_n}\right) \ , \\ f_\sigma^{(k)}(E) &= \sum_{n=1}^{k} b_n e^{-(E-E_n)^2/\,2\sigma^2} \ , \end{aligned} \tag{4.61}$$

where σ is the smearing radius defined by Eq. (4.38). The integer k encodes how many states are included in our model function. E_n, a_n and b_n are the fit parameters which relate to finite volume energies and matrix elements. These are estimated by minimising appropriate χ^2 functions

$$\chi^2_{g^{(k)}} = \sum_{t,r} \left(g^{(k)}(t) - C(t)\right) \mathrm{Cov}^{-1}_{tr}[C] \left(g^{(k)}(r) - C(r)\right) \ , \tag{4.62}$$

$$\chi^2_{f^{(k)}_\sigma} = \sum_{E,E'} \left(f^{(k)}_\sigma(E) - \rho_\sigma(E)\right) \mathrm{Cov}^{-1}_{EE'}[\rho_\sigma] \left(f^{(k)}_\sigma(E') - \rho_\sigma(E')\right) \ , \tag{4.63}$$

where covariance matrices are estimated as in Eq. (4.49) both for correlators and spectral densities.

On the lattice, the temporal length T constrains the maximum number of data points and hence degrees of freedom for fitting a correlator $C^R_{\mathrm{PP}}(t)$. The effect of correlation between times t and t' is taken into account by the covariance matrix appearing in $\chi^2_{g^{(k)}}$. The smeared spectral density $\rho^R_{\mathrm{PP},\sigma}(E)$ depends on the correlator at all lattice times t, and it can be in principle evaluated for any energy E. Not all points in energy, however, provide independent information. Indeed, the information contained in $\rho^R_{PP,\sigma}(E)$ and $\rho^R_{PP,\sigma}(E')$ for $|E - E'| \ll \sigma$ is essentially the same, from both the physical and the statistical viewpoint. With this motivation, it is interesting to study the number of degrees of freedom we can exploit in each correlated fit. While the correlators can only be evaluated at integers $0 \leq t < T$, we have freedom to choose the energies in a given interval at which we evaluate the spectral densities. Our criterion is to select those that minimise the condition number of $\mathrm{Cov}[\rho_\sigma]$ in order to maximise the information that is passed to the χ^2. We observe that correlated data in time does not necessarily translate into correlated data in energy space, as shown in Fig. 4.10, where we compare covariance matrices for $C^{(2AS)}_{\mathrm{PP}}(t)$ and $\rho^{(2\mathrm{AS})}_{\mathrm{PP},\sigma}(E)$ from the ensemble B3 with a smearing radius $\sigma = 0.2/a$.

In both cases, the number of data points is enough to fit at least two states. The matrix $\mathrm{Cov}^{-1}_{tt'}[C]$, in particular, is evaluated from correlators measured from $t/a = 8$ to $t/a = 16$ with an interval of two. Regardless of the thinning in time, adjacent points shows a very high correlation. If the covariance matrix of the correlator $\mathrm{Cov}[C]$ is ill-conditioned, it needs to be regularised by applying a cutoff on its smaller eigenvalues before $\chi^2_{g^k}$ is evaluated, a problem

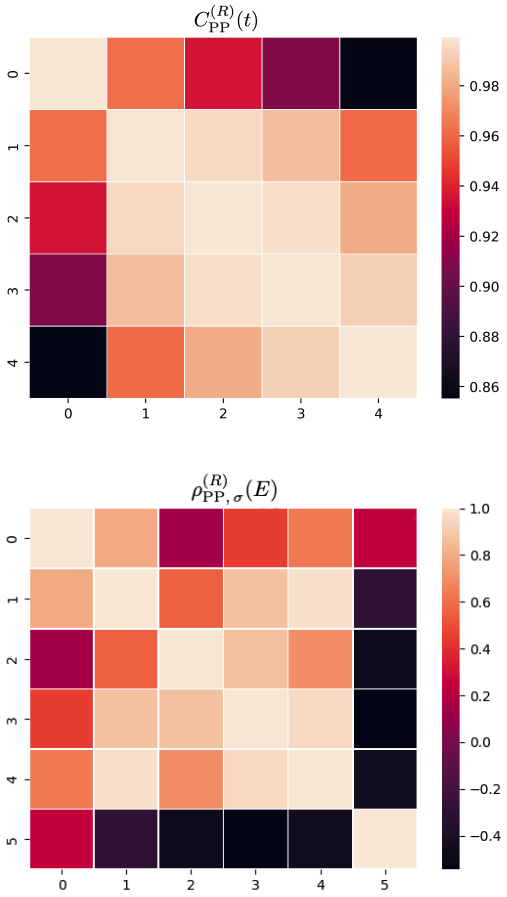

Figure 4.10 *Covariance matrices for the lattice correlator $C^{(2AS)}_{\mathrm{PP}}(t)$ at five time slices (top) and the smeared spectral density $\rho^{(2\mathrm{AS})}_{\mathrm{PP},\sigma}(E)$ evaluated at six energies (bottom) from $C^{(2\mathrm{AS})}_{\mathrm{PP}}(t)$. The points at which the spectral density is evaluated are chosen in order to minimise the condition number of its covariance matrix. Due to this freedom, we obtain a matrix for the spectral density that is better conditioned than the one for the correlator.*

that is not faced when fitting spectral densities, whose covariance matrix is easier to invert. Indeed, one has to invert the covariance of the correlators in order to compute the spectral density, but only in the combination defined by Eq. (4.46): the matrices obtained from the functionals $A_\alpha[\boldsymbol{g}]$ and $B[\boldsymbol{g}]$, if both ill conditioned, regularise each other for suitable values of λ. The choice of a cutoff for the covariance matrix $\mathrm{Cov}[C]$ is therefore absorbed into the choice of the parameter λ.

Fig. 4.11 shows two examples of correlated fits of the smeared spectral densities. On the top panel, the correlator used to extract $\rho^{(2\mathrm{AS})}_{\mathrm{PP},\sigma}$ is built with smeared interpolating fields. The model function is $f^{(3)}_\sigma$ from Eq. (4.61). The plot shows

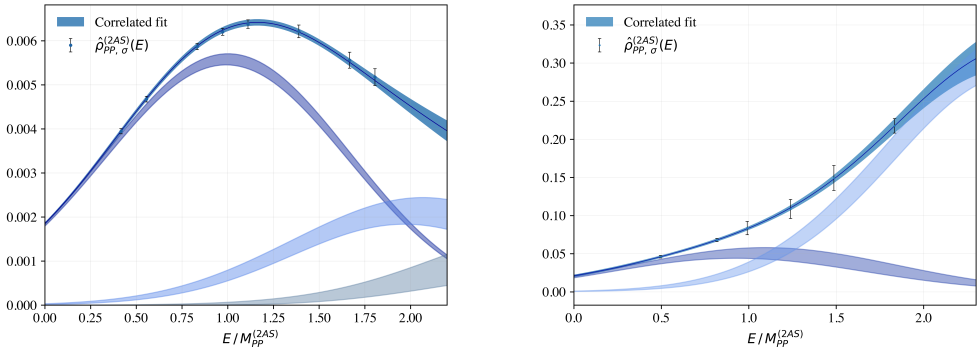

Figure 4.11 *Examples of fits of spectral densities, showing the breakdown of the contribution of each Gaussian. On the top panel, a three Gaussian fit of a smeared spectral density extracted from a correlator that uses smeared, non-local fields. Due to this choice for the interpolator, the Gaussians in the plot are shorter as we go higher in the energy range. On the bottom panel, we show a similar plot obtained from local interpolators: the two-Gaussian fit is still able to isolate the ground state even if the effective mass does not plateau. Both plots correspond to the pseudoscalar 2AS channel. The top panel is obtained from the ensemble B3 and the spectral density has smearing radius $\sigma = 0.24/a$. The bottom panel is derived from the ensemble B2 and the smearing radius of the spectral density is $\sigma = 0.3/a$.*

each individual Gaussian, which correspond to the contribution of different energy levels: as each of them becomes decreasingly important, we clearly see the excited state suppression achieved by the choice of smeared operators in the correlation function. At low energies, the spectral density is almost entirely dominated by the first energy level, therefore the corresponding fit parameter is mainly constrained by energies near the origin. Cancellations between the three correlated contributions combine in an error on the fit result that is generally smaller than the one on the single Gaussians. We identify the first peak as the value of $aM_{\mathrm{PP}}^{(2\mathrm{AS})}$ and the second with $aE_{\Pi\Pi}$. The bottom panel of Fig. 4.11 is instead obtained from local interpolators, which have a larger overlap with excited states. As shown in Fig. 4.8, the effective mass of Eq. (4.34) does not reach a clear plateau in this case, yet the fit of the spectral density is able to isolate the ground state. The error on the fit, however, is at best one order of magnitude larger than the corresponding one obtained in the top panel. The choice of smeared operators is therefore preferred.

We now turn to the comparison of the fit results. As described in Sec. 4.5.2, the extraction of the ground state presents challenges in the antisymmetric

sector, which therefore provides an interesting testbed to compare the two frameworks. We use for the comparison the ensembles B1-B4, where the PCAC masses of both representations are below 0.1 in lattice units, see C.1. We begin by discussing the estimate of $aM_{\mathrm{PP}}^{(\mathrm{2AS})}$ from lattice correlators. In some cases, the covariance matrix of the two point function had to be regularised by introducing a cutoff on its lower eigenvalues, in order to invert it in the χ^2. The choice of this cutoff can translate into fluctuations in the estimate of the pseudoscalar mass outside the statistical error, that have been accounted for by adding a systematic component to the uncertainty. This problem does not appear while fitting spectral densities, because the covariance of the spectral density is better conditioned. We have also ensured that no contamination was present in the estimate for the pseudoscalar mass by comparing fits of one and more exponentials. The values of the pseudoscalar mass obtained with this approach can be found in Table C.4. In this framework the smearing of the interpolators has been crucial, as it is clear from Fig. 4.8 where the effective mass of Eq. (4.34) does not plateau due to the short temporal extent of the lattice. The spectral density, on the other hand, does not rely on any large time behaviour. Its limit lies in the high energy range, where its error becomes large. In order to perform the reconstruction, the algorithmic inputs are chosen in the region of stability as described in Sec. 4.5. Fig. 4.12 updates the plot from Fig. 4.7 showing that stability for the reconstruction translates into stability for the fits: the blue band, which is the fit result for the smeared spectral density at the energy $E_\star$, is compatible with all the values generated by different choices for the unphysical parameter λ.

The choice of the smearing width is dictated by the quality of the data. In this work, we managed to obtain values ranging from $\sigma = 0.18/a$ to $0.33/a$. Since the separation between finite volume energies should be roughly $2\pi/L \simeq 0.4/a$, these values can be considered acceptable. For each ensemble, we have performed the fit at a fixed value of σ, obtaining a prediction for the pseudoscalar mass $aM_{\mathrm{PP},\sigma}^{(\mathrm{2AS})}$. We then performed a scan over different smearing radii to check for systematic effects. As shown in the example of Fig. 4.13, the smearing radii adopted were found to be small enough to identify the ground state; in most cases, still, we have observed fluctuations for $aM_{\mathrm{PP},\sigma}^{(\mathrm{2AS})}$ as σ varies. When they occurred, we added half the spread of these fluctuations as a systematic error. Fig. 4.13 also shows a comparison between fits that include two and three states: the results are in good agreement, signalling that no contamination from excited states is affecting the estimate of the mass.

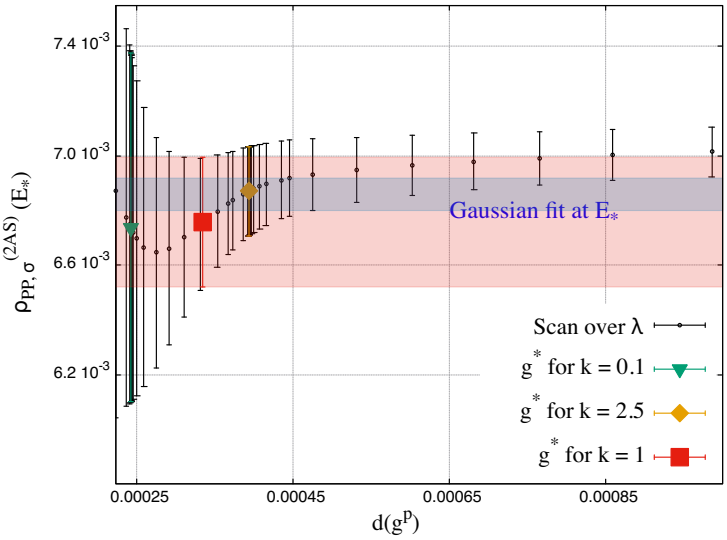

Figure 4.12 *The plot updates Fig. 4.7, which shows that the reconstruction (red band) does not change outside the statistical error (black bars) for different choices of the unphysical parameter λ, in the given range of $d(\boldsymbol{g^p})$ (cf. Eq. (4.53)). The blue band is the fit result of the smeared spectral density to a sum of Gaussians at the point $E_\star$. Encouragingly, the fit is compatible with all points in the scan, showing that stability in the reconstruction translates into stability for the fits.*

Ensemble	$aM_{\mathrm{PP}}^{(\mathrm{2AS})}$ from $C_{\mathrm{PP}}^{(2AS)}(t)$	$aM_{\mathrm{PP},\sigma}^{(\mathrm{2AS})}$ from $\rho_{\mathrm{PP},\sigma}^{(\mathrm{2AS})}(E)$
B1	0.4638(33)	0.4607(71)
B2	0.4035(24)	0.3996(88)
B3	0.3600(38)	0.3550(31)
B4	0.3407(48)	0.3420(71)

Table 4.2 *Predictions for the pseudoscalar mass in the 2AS sector from different ensembles. The values are depicted in Fig. 4.14.*

The comparison between fits of spectral densities and correlators is shown in Fig. 4.14. The predictions are always compatible, and the errors are of the same order of magnitude, but the uncertainty from the correlator is generally smaller, up to a factor of approximately two.

The numerical values used in this comparison are listed in Table 4.2. It should be noticed that the outcome of this comparison holds with the given amount of statistics and time extent of the lattice. These quantities, in fact, heavily influence the analysis both on the side of the correlators and the spectral density, yet the way in which the two methodologies are affected can be different.

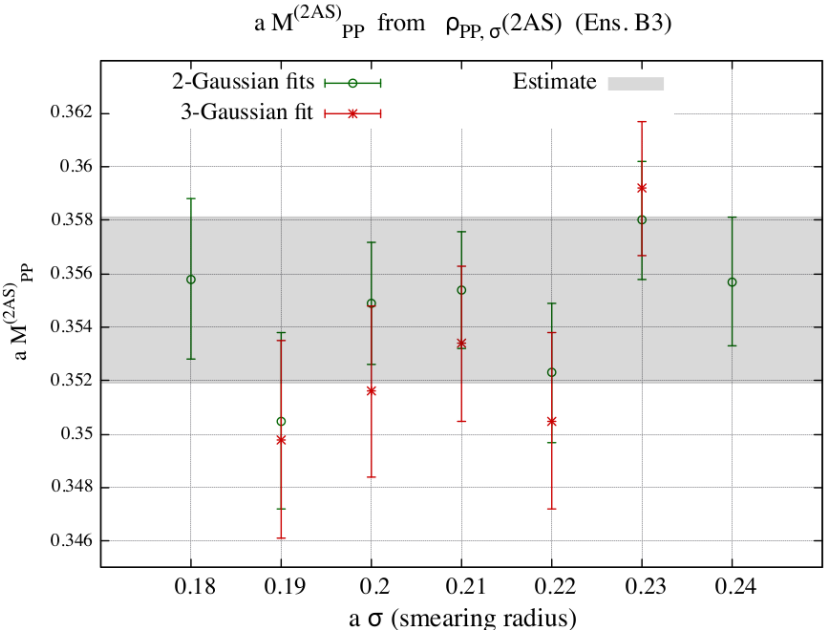

Figure 4.13 *Fit results for $aM_{\mathrm{PP}}^{(2\mathrm{AS})}$ from the ensemble B3, obtained from two (green) and three (red) Gaussian fits of smeared spectral densities at different smearing radii σ. Fluctuation at different values of the smearing radius translate into a systematic component of the uncertainty. This is summed in quadrature to the statistical error in the gray, horizontal band, the estimate for the pseudoscalar mass $aM_{\mathrm{PP}}^{(2\mathrm{AS})} = 0.3550(31)$.*

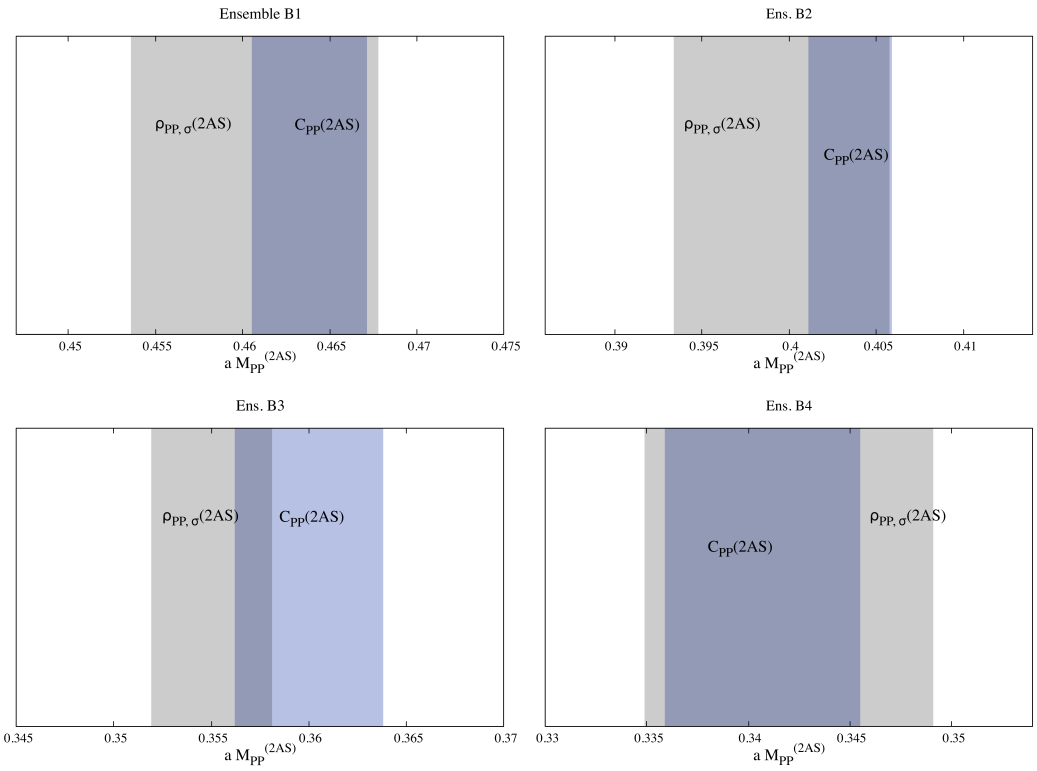

Figure 4.14 *Graphical comparison between the two predictions for* $aM_{\mathrm{PP}}^{(2\mathrm{AS})}$ *for the ensembles B1-B4.*

Chapter 5

Results for $Sp(4)$

In this Chapter, we analyse the physics of the $Sp(4)$ gauge theory with four fermions in the 2AS representation. This model, as motivated in Chapter 2.5, can be important for the understanding of the conformal window. The implementation of symplectic theories in Grid, more generally, opens the door to non-perturbative studies with a range of phenomenological applications: composite Higgs, Dark matter, top partial compositeness, and of course conformality. This Chapter reproduces parts of Ref. [2], a work done in collaboration with many people. The main contribution of the author of this thesis was to develop the code that has been used to simulate $Sp(2N)$ gauge theories.

Since we use new software, we first perform some checks in Section 5.1. We then show, in Section 5.2, the study of the bulk phase transition of $Sp(4)$ with four 2AS fermions. Finally, in Section 5.3, we discuss aspects of scale setting and topology.

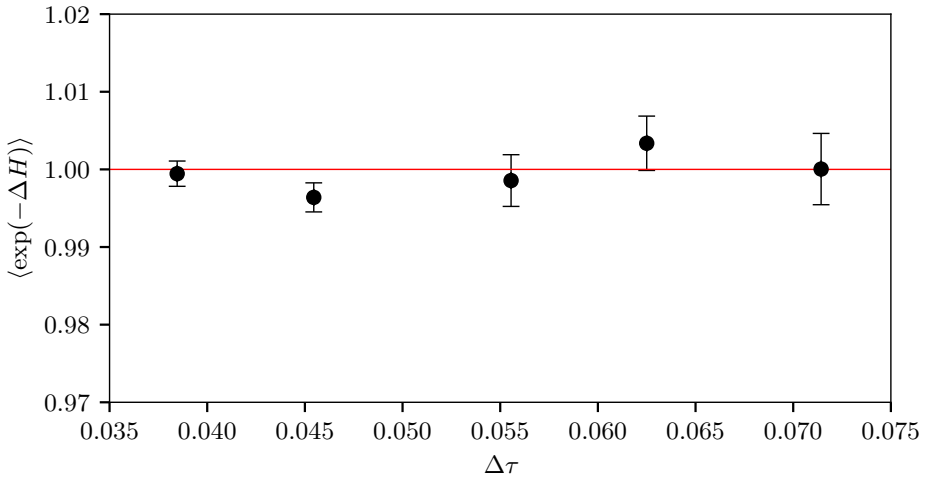

Figure 5.1 *Test of Creutz equality,* $\langle \exp(-\Delta H)\rangle = 1$*; dependence of* $\langle \exp(-\Delta H)\rangle$ *on the time–step* $\Delta\tau$ *in the MD integration, for* $N = 2$*,* $N_{\rm f} = 0$*, and* $N_{\rm as} = 4$*. The relevant parameters of this study are the trajectory length* $\tau = 1$*, number of steps* $n_{\rm steps} = 14, 16, 18, 22, 26$ *(*$\Delta\tau = \tau/n_{\rm steps}$*), for an ensemble with lattice volume* $\tilde{V}/a^4 = 8^4$*,* $\beta = 6.8$*, and* $am_0^{\rm as} = -0.6$*.*

5.1 Tests of the Algorithm

In this Section, which reproduces results shown from Ref. [2], we follow closely Sects. III and IV of Ref. [94] in order to validate our implementation of the HMC. The MD evolution is implemented using a second-order Omelyan integrator [111].

Given that the $Sp(2N)$ implementation is new, we focus here on testing the HMC for a $Sp(4)$ gauge theory, with $N_{\rm f} = 0$, and $N_{\rm as} = 4$ as a case study. We present the results in Figs. 5.1, 5.2, 5.3, 5.4, and 5.5, obtained, for convenience, setting the lattice parameters to $\beta = 6.8$, and $am_0 = -0.6$, on an isotropic lattice with volume $\tilde{V} = (8a)^4$.

The first test pertains to Creutz equality [112]: by measuring the difference in Hamiltonian, ΔH, evaluated before and after the MD evolution, one should find that

$$\langle \exp\Big(-\Delta H\Big)\rangle \;=\; 1\,. \tag{5.1}$$

This is supported by our numerical results: Fig. 5.1 shows the value of

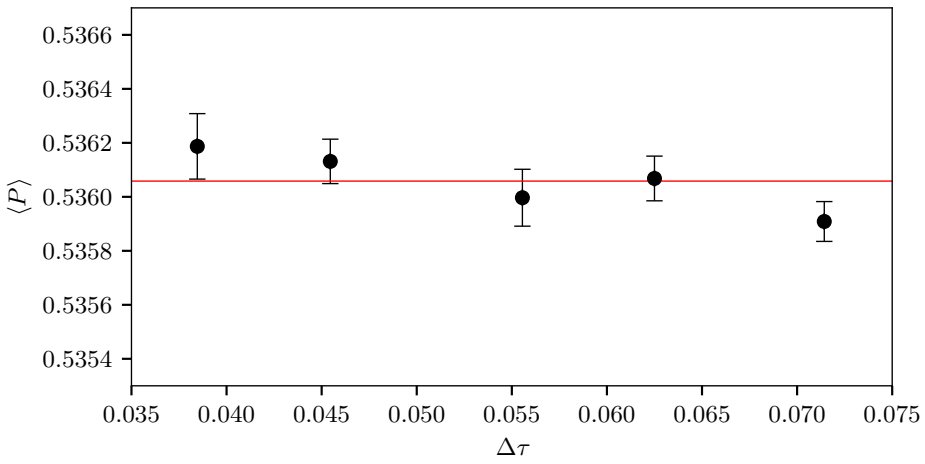

Figure 5.2 *Test of independence of the plaquette on the time–step $\Delta\tau$ used for the MD integration, for $N = 2$, $N_{\rm f} = 0$, and $N_{\rm as} = 4$. The relevant parameters of this study are the trajectory length $\tau = 1$, number of steps $n_{\rm steps} = 14, 16, 18, 22, 26$, $\Delta\tau = \tau/n_{\rm steps}$, for an ensemble with lattice volume $\tilde{V}/a^4 = 8^4$, $\beta = 6.8$, and $am_0^{\rm as} = -0.6$. The horizontal line corresponds to the plaquette value obtained averaging over trajectories having different a number of step values, $n_{\rm steps}$.*

$\left\langle \exp\left(-\Delta H\right)\right\rangle$ for five different choices of the time-step used in the MD integration, with $\Delta\tau = \tau/n_{steps}$, and the choice $\tau = 1$. The numerical results are obtained by considering a thermalised ensemble consisting of 3400 trajectories. A closely related test is shown in Fig. 5.2: the value of the ensemble average of the plaquette is independent of $\Delta\tau$.

A third test pertains to the dependence of $\langle \Delta H\rangle$ on $\Delta\tau$, which for a second-order integrator is supposed to scale as $\langle \Delta H\rangle \propto (\Delta\tau)^4$—see the discussion in Ref. [113]. In Fig. 5.3 we show our measurements, together with the result of a best-fit to the curve $\log\langle \Delta H\rangle = \mathcal{K}_1 \log(\Delta\tau) + \mathcal{K}_2$, with $\mathcal{K}_1 = 3.6(4)$ determined by minimising a simple χ^2. We find good agreement, as quantified by the value of the reduced $\chi^2/N_{\rm d.o.f.} = 0.6$, and $\mathcal{K}_1$ is compatible with 4. A closely related test is displayed in Fig. 5.4, confirming the prediction that the acceptance probability of the algorithm, $P_{\rm acc}$, obeys the relation [114]:

$$P_{\rm acc} \;=\; \mathrm{erfc}\left(\frac{1}{2}\sqrt{\left\langle \Delta\, H\right\rangle}\right)\,. \tag{5.2}$$

The final test of this section is displayed in Fig. 5.5. We refer the reader

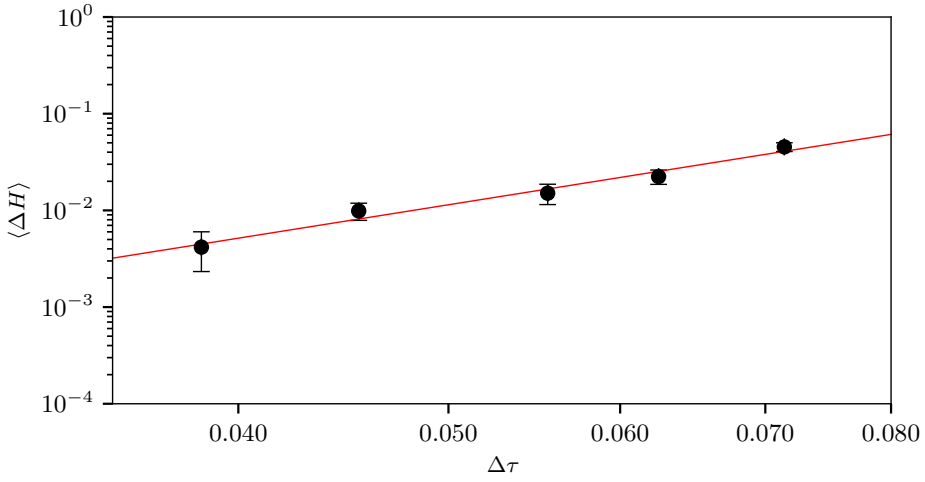

Figure 5.3 *Dependence of $\langle \Delta H \rangle$ on the time-step, $\Delta\tau$, used for the MD integration, for $N = 2$, $N_{\rm f} = 0$, and $N_{\rm as} = 4$. The expectation value $\langle \Delta H \rangle$ is proportional to $(\Delta\tau)^4$, consistently with the use of a second-order integrator. The plot is shown in log-log scale. The relevant parameters of this study are the trajectory length $\tau = 1$, number of steps $n_{steps} = 14, 16, 18, 22, 26$ ($\Delta\tau = \tau/n_{\rm steps}$), for an ensemble with lattice volume $\tilde{V}/a^4 = 8^4$, $\beta = 6.8$, and $am_0 = -0.6$.*

to Ref. [94] for discussions, rather than reproduce them here. The quantity $|\delta H|$ is the average difference of the Hamiltonian evaluated by evolving the MD forward and backward and flipping the momenta at $\tau = 1$. Since the Hamiltonian in these tests is of order $\sim 10^6$ and the typical $\delta H \sim 10^{-11}$, the results show that the violation of reversibility is consistent with having $|\delta H|/H$ of the order of the numerical accuracy. This is the expected relative precision for double-precision floating-point numbers. Moreover, the violation $|\delta H|$ is independent of $\Delta\tau$.

For illustration purposes, we find it useful to monitor the contribution to the MD of the fields, and how this changes as we dial the lattice parameters. We focus on the theory with $N = 2$, $N_{\rm f} = 0$, and $N_{\rm as} = 4$, and consider a few ensembles with isotropic lattice with $\tilde{V} = (8a)^4$, and lattice coupling $\beta = 6.8$, but vary the mass $am_0^{\rm as}$. We show in Fig. 5.6 the force, F, from Eq. (3.48) divided in its contribution from the gauge and fermion dynamics, the latter computed using the HMC for all fermions. The results are normalised so that the gauge contribution is held constant. As can be clearly appreciated, for large and positive values of $am_0^{\rm as}$ the fermions can be neglected, as for these choices of the mass, one expects to be in the quenched regime. When

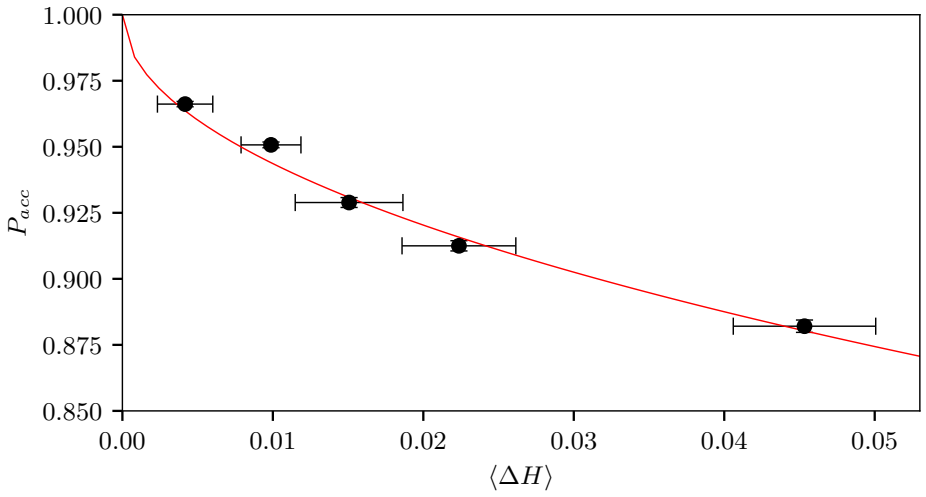

Figure 5.4 *Test of the relation between acceptance probability and ΔH, for $Sp(4)$, $N_{\rm f} = 0$, and $N_{\rm as} = 4$. The expected behaviour $P_{acc} = erfc(\sqrt{\Delta H}/2)$ is supported. The relevant parameters of this study are the trajectory length $\tau = 1$, number of steps $n_{\rm steps} = 14, 16, 18, 22, 26$ ($\Delta\tau = \tau/n_{\rm steps}$), for an ensemble with lattice volume $\tilde{V}/a^4 = 8^4$, $\beta = 6.8$, and $am_0 = -0.6$.*

decreasing the mass, the fermion contribution increases. For large, negative values of the Wilson bare mass, the fermion contribution is even larger than the contribution of the gauge part of the action.

While in this work we are mostly interested in the theory with $N = 2$, $N_{\rm f} = 0$, and $N_{\rm as} = 4$, and hence we can use the HMC algorithm, for the general purpose of identifying the extent of the conformal window in this class of lattice gauge theories it may be necessary to consider also odd numbers of fermions, for which we resort to the RHMC algorithm. The latter relies on a rational approximation in the computation of the fermionic force, but the presence of a Metropolis accept-reject step ensures that the algorithm is exact. Thus, a preliminary test must be made to check the consistency of the implementation—as was done for $SU(3)$ theories, see for instance Ref. [115]. To gauge whether the numerical implementation is working at the desired level of accuracy and precision, we performed the exercise leading to Fig. 5.7. We computed the average plaquette, $\langle P \rangle$, where P is defined as

$$P \equiv \frac{a^4}{6\tilde{V}} \sum_x \sum_{\mu<\nu} \left[\frac{1}{2N} \mathrm{Re}\,\mathrm{Tr}\, U_{\mu\nu}(x) \right] \tag{5.3}$$

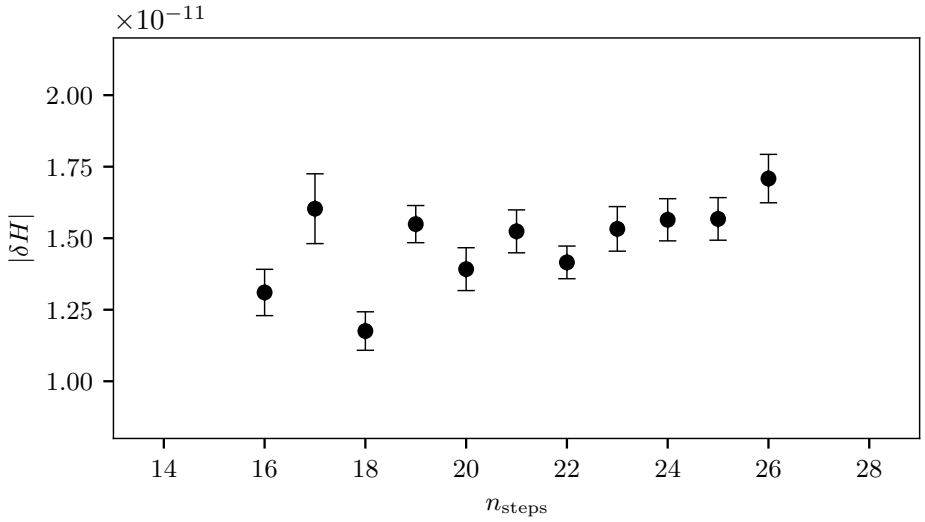

Figure 5.5 *Reversibility test, showing $|\delta H|$ for various choices of $\Delta\tau$, for $N = 2$, $N_{\rm f} = 0$, and $N_{\rm as} = 4$. The relevant parameters of this study are the trajectory length $\tau = 1$, number of steps $n_{\rm steps} \in [16, 26]$ ($\Delta\tau = \tau/n_{\rm steps}$), for an ensemble with lattice volume $\tilde{V}/a^4 = 8^4$, $\beta = 6.8$, and $am_0 = -0.6$.*

for ensembles having lattice volume $\tilde{V} = (8a)^4$ and coupling $\beta = 6.8$, for a few representative choices of the bare mass $-1.4 \leq am_0^{\rm as} \leq 0.0$. We repeated this exercise three times: at first, we treated all fermions with the HMC, then we treated them all with the RHMC, and finally we used a mixed strategy, treating two fermions with the HMC, and two with the RHMC. We display, in the two plots in the figure, the differences of the second and third approaches to the first one, respectively. We detect no visible discrepancies, the differences being compatible with zero within the statistical uncertainties.

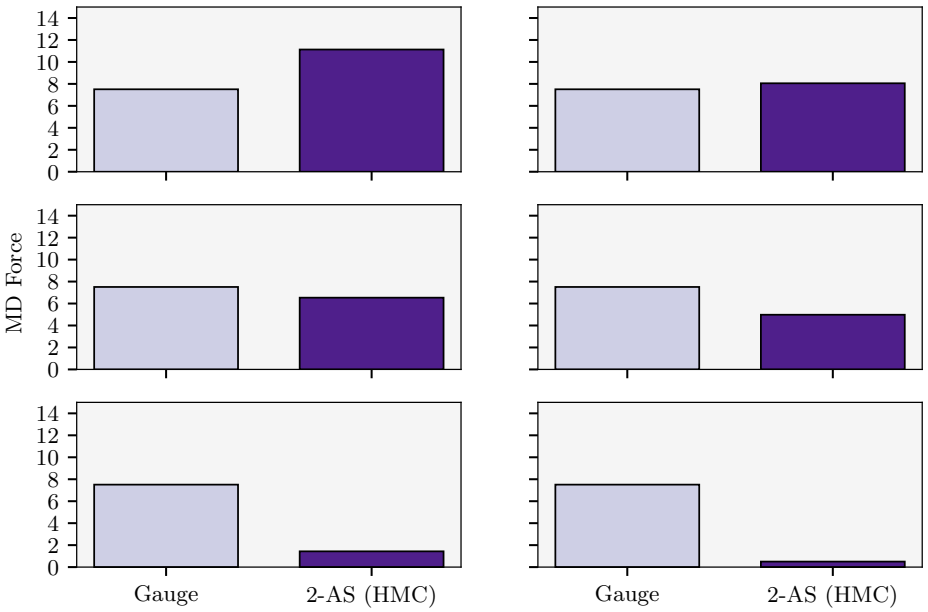

Figure 5.6 *Field contribution to the MD force for the theory with* $N = 2$, $N_{\mathrm{f}} = 0$, *and* $N_{\mathrm{as}} = 4$, *on isotropic lattice with* $\tilde{V} = (8a)^4$, *and lattice coupling* $\beta = 6.8$. *The two blocks are respectively indicating the gauge (light shading, left) and the fermion (dark shading, right) contribution, the latter computed with the HMC algorithm. Fermion contributions are summed over flavor. The six panels correspond to different choices of bare mass:* $am_0^{\mathrm{as}} = -0.9, -0.1, +0.6, +1.8, +15, +50$ *(left to right, top to bottom).*

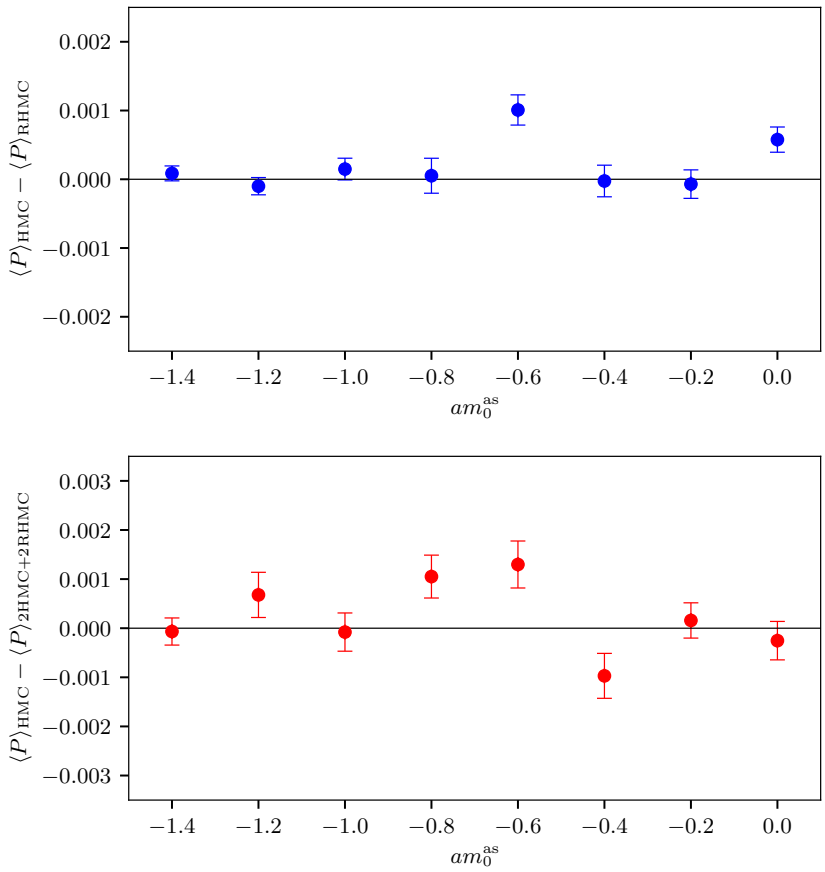

Figure 5.7 *Compatibility between plaquette averages $\langle P\rangle$ obtained with HMC and RHMC algorithms for the theory with $N = 2$, $N_{\mathrm{f}} = 0$, and $N_{\mathrm{as}} = 4$. $\langle P\rangle_{\mathrm{HMC}}$ is obtained running two couples of fermions with HMC. For $\langle P\rangle_{\mathrm{RHMC}}$ (top panel), RHMC was applied individually to each of the fermions. $\langle P\rangle_{\mathrm{2HMC+2RHMC}}$ (bottom panel) is obtained running two fermions with HMC, while the other two were run with RHMC. The lattice coupling is $\beta = 6.8$, with the bare mass in the range $-1.4 \leq am_0^{\mathrm{as}} \leq 0.0$. The lattice is isotropic and has volume $\tilde{V} = (8a)^4$.*

5.2 Investigation on the bulk phase transition

For $Sp(4)$ with four 2AS fermions, we performed a coarse scan of the lattice parameter space, to identify phase transitions in the (β, m_0) space, by studying the average plaquette, $\langle P \rangle$, its hysteresis, and its susceptibility. We provide an approximate estimate of the value of β above which there is no bulk phase transition. Above this value, that we refer to as β^*, one can safely perform lattice numerical calculations at finite lattice spacing, yet confident that the results can be extrapolated to the appropriate continuum limit.

Figure 5.8 displays the average plaquette, $\langle P \rangle$, defined in Eq. (5.3), obtained in ensembles generated using a cold start. The lattice size is $\hat{V} = (8a)^4$, and each point is obtained by varying the lattice coupling $\beta = 7.0, 6.8, 6.6, 6.5, 6.4, 6.3, 6.2, 6.0, 5.8, 5.6$ and the bare mass $-1.4 \leq am_0^{\text{as}} \leq 0.0$. The figure shows that, for small values of β and large, negative values of the bare mass, the average plaquette displays an abrupt change at a particular value $am_0^{\text{as}\,*}$, while being a smooth, continuous function elsewhere. This is a first indication of the existence of a first-order bulk phase transition.

To better understand whether a first-order phase transition is taking place, we study the effect of adopting different starting configurations in the HMC: we use both random (hot), and unit (cold) configurations. Figure 5.9 shows the comparison of the average plaquette, $\langle P \rangle$, computed for several fixed choices of the coupling β, while varying the bare mass $-1.4 \leq am_0^{\text{as}} \leq 0.0$ depending on the starting configuration used. The two curves in the plots represent the behaviour measured in ensembles obtained from a cold and hot start configuration. The effects of hysteresis are clearly visible for $\beta < 6.4$ and are an indication of the presence of a first-order phase transition taking place at a critical value of the bare mass $am_0^{\text{as}\,*}$.

The final test of the nature of the phase transition is shown in Fig. 5.10. For illustration purposes, we choose two values of the coupling for which we have evidence of a phase transition ($\beta = 6.2$), or of smooth behaviour of $\langle P \rangle$ for all value of am_0^{as} ($\beta = 6.5$), respectively. We compute the plaquette susceptibility, defined as

$$\chi_P \equiv \frac{\tilde{V}}{a^4} \left(\langle P^2 \rangle - (\langle P \rangle)^2 \right) , \tag{5.4}$$

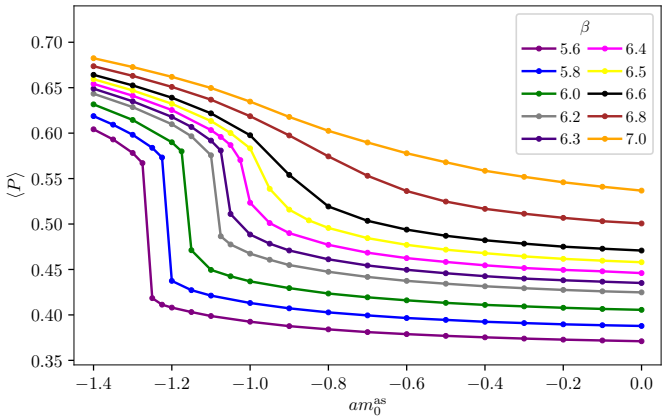

Figure 5.8 *Parameter scan of the $Sp(4)$ theory with $N_{\mathrm{as}} = 4$ fermions transforming in the 2-index antisymmetric representation, with ensembles generated from a cold start, using the HMC. We show the value of the average plaquette, $\langle P \rangle$, as a function of the bare mass, for a few representative values of the coupling. The lattice size is $\tilde{V} = (8a)^4$, and each point is obtained by varying the lattice coupling $\beta = 7.0, 6.8, 6.6, 6.5, 6.4, 6.3, 6.2, 6.0, 5.8, 5.6$ and the bare mass $-1.4 \leq am_0^{\mathrm{as}} \leq 0.0$.*

and compare the numerical results obtained with ensembles having two different volumes, $\tilde{V} = (8a)^4$ and $\tilde{V} = (16a)^4$. The results indicate that the peak height scales as the 4-volume when β is small, in which case the position of the peak also moves to a different value of am_0^{as}. These are indeed the expected signature of a first order phase transition. For large β, the curves obtained for different volumes are compatible with one another, a clear indication of a smooth crossover. We hence conclude that, in the theory with $N = 2$, $N_{\mathrm{f}} = 0$, and $N_{\mathrm{as}} = 4$, there is numerical evidence of a line of first-order phase transitions turning into a crossover at $\beta > \beta_* = 6.4$.

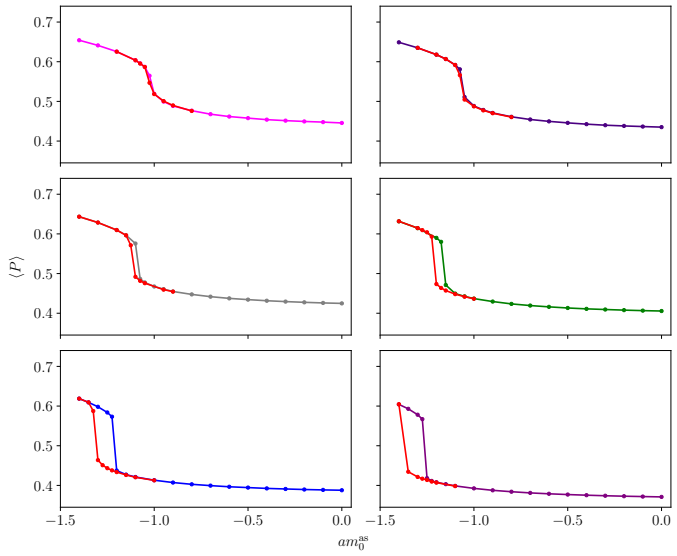

Figure 5.9 *Hysteresis between hot (red) and cold (other colors) starts for the $Sp(4)$ theory with $N_{\rm as} = 4$ fermions in the 2-index antisymmetric representation. The lattice coupling is $\beta = 6.4, 6.3, 6.2, 6.0, 5.8, 5.6$ (left to right, and top to bottom). The lattice size is $\tilde{V} = (8a)^4$, and each point is obtained by varying the bare mass $-1.4 \leq am_0^{\rm as} \leq 0.0$.*

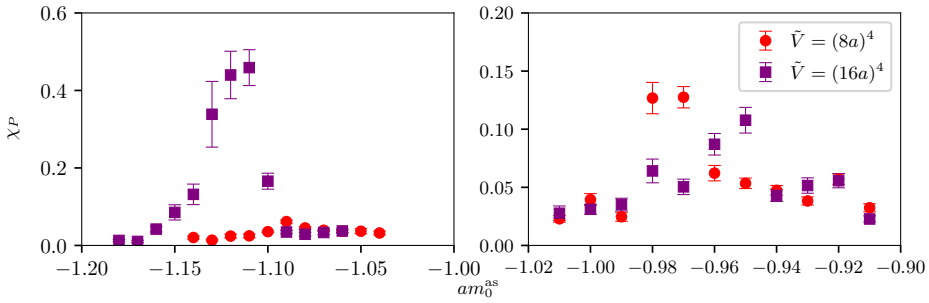

Figure 5.10 *Plaquette susceptibility, χ_P, in the $Sp(4)$ lattice theory with $N_{\rm as} = 4$ fermions in the 2-index antisymmetric representation. We use two values of the lattice size, $\tilde{V} = (8a)^4$ and $\tilde{V} = (16a)^4$. The ensembles have $\beta = 6.2$, $-1.18 \leq am_0 \leq -1.04$ (left panel), and $\beta = 6.5$, $-1.01 \leq am_0 \leq -0.91$ (right panel).*

5.2.1 Varying $N_{\rm as}$

We repeat the parameter scan for other choices of $N_{\rm as}$, using the RHMC for all fermions when $N_{\rm as}$ is odd, and the HMC algorithm otherwise. The purpose of the exercise is to study the dependence of the upper bound coupling for the bulk phase β_* on the number of fermions, $N_{\rm as}$. Indeed, for small $N_{\rm as}$ we expect the theory to confine, while for larger values of $N_{\rm as} \sim N_{\rm as}^c$ the theory should approach the lower end of the conformal window, and eventually lose asymptotic freedom. We recall that the latter scenario requires to impose the bound $N_{\rm as} < 33/4$ in $Sp(4)$, while setting the stage for a first truly non-perturbative determination of the lower bound of the conformal window is the main motivation for this study.

The results of these studies are shown in Fig. 5.11, which displays our measurements of the average plaquette, $\langle P \rangle$, as a function of the bare parameters of the theories. For the pure gauge $Sp(4)$ theory, we get plaquette values that are in agreement with the ones shown in Ref. [11]. The corresponding upper bound value of the coupling is roughly estimated to be $\beta_* \simeq 7.2$.

For theories with dynamical fermions, we vary both the masses and the coupling of the theories. As can be seen from Fig 5.11, for $N_{\rm as} = 1$ the upper bound is $\beta_* \simeq 6.8$. For $N_{\rm as} = 2$ the upper bound is $\beta_* \simeq 6.7$, and for $N_{\rm as} = 3$ it is $\beta_* \simeq 6.5$, in agreement with the values found in Ref. [116]. At a larger number of fermions species, we obtain progressively smaller values of β for the upper bound of the bulk phase β: for $N_{\rm as} = 5$, we get $\beta_* \simeq 6.3$. For $N_{\rm as} = 6$, the upper bound coupling is $\beta_* \simeq 6.2$. For $N_{\rm as} = 7$, we get $\beta_* \simeq 6.1 \div 6.2$ and for $N_{\rm as} = 8$, $\beta_* \simeq 6.1$.
Overall, we notice a trend according to which the more fermion flavors are present in the $Sp(4)$, the smaller the upper bound value of the coupling we find and the bigger is the corresponding critical bare mass $am_0^{({\rm as})*}$.

5.3 Scale setting and topology

We return now to the theory with $N = 2$, $N_{\rm f} = 0$, and $N_{\rm as} = 4$. We discuss a scale setting procedure that uses the Wilson flow. We also monitor

the evolution of the topological charge, to show that topological freezing was avoided. We focus the discussion on a few representative examples, although we checked that our conclusions have general validity for all choices of parameter relevant to this study.

The gradient flow [14], and its discretised counterpart, the Wilson flow [15], are useful for two complementary purposes. On the one hand, the Wilson flow provides a universal, well-defined way to set the scale in a lattice theory. On the other hand, the process we will describe consists of taking gauge configurations and evolving them with a flow equation, which results in the smoothening of such configurations, and the softening of short-distance fluctuations. The former property is beneficial because it allows to compare to one another different theories for which no experimental information is available, and that might have different matter content. The latter feature allows, in practical terms, to reduce the short-distance numerical noise and the effects of discretisation in the lattice calculation of observables, such as the topological charge, Q, which are sensitive to fluctuations at all scales.

We follow Refs. [10, 16] (and references therein). One introduces the flow time, t, as an additional, fifth component of the space-time variables, and solves the defining differential equation

$$\frac{\mathrm{d}B_\mu(x,\,t)}{\mathrm{d}t} \;=\; D_\nu G_{\nu\mu}(x,\,t)\,, \tag{5.5}$$

subject to the boundary conditions $B_\mu(x,\,0) = A_\mu(x)$. Here $A_\mu(x)$ are the gauge fields, and the covariant derivatives are $D_\mu \equiv \partial_\mu + [B_\mu,\,\cdot\,]$, and $G_{\mu\nu}(t) = [D_\mu,\,D_\nu]$. As anticipated, the main action of the flow is to introduce a Gaussian smoothening of the configurations, with mean-square radius $\sqrt{8t}$. In order to use this object to introduce a scale, one defines the quantities

$$\mathcal{E}(t) \;\equiv\; \frac{t^2}{2}\,\langle \mathrm{Tr}\,[G_{\mu\nu}(t)G_{\mu\nu}(t)]\rangle\,, \tag{5.6}$$

$$\mathcal{W}(t) \;\equiv\; t\frac{d}{dt}\mathcal{E}(t)\,, \tag{5.7}$$

and introduces a prescription that defines the scale on the basis of a reference value for either of the two. Two common choices in the literature are the scale, t_0, defined by setting

$$\mathcal{E}(t)|_{t=t_0} = \mathcal{E}_0\,, \tag{5.8}$$

or the scale, w_0, defined implicitly by the condition

$$\mathcal{W}(t)|_{t=w_0^2} = \mathcal{W}_0 \,. \tag{5.9}$$

Both $\mathcal{E}_0$ and $\mathcal{W}_0$ are set on the basis of theoretical considerations. For example, Ref. [16] advocates to set $\mathcal{W}_0 = c_w C_2(F)$, where $C_2(F) = (1 + 2N)/4$ is the quadratic Casimir operator of the fundamental representation in $Sp(2N)$ theories, and one sets $c_w = 0.5$, though other choices are possible.

On the discretised lattice, one replaces the gauge field, $A_\mu(x)$, with the link variable, $U_\mu(x)$, and the flow equation is rewritten by replacing $B_\mu(x,\, t)$ with the new $V_\mu(x,\, t)$ (with $V_\mu(x,\, 0) = U_\mu(x)$). There are then at least two ways to replace $G_{\mu\nu}$ with a discretised variable. We introduced the elementary plaquette $\mathcal{P}_{\mu\nu}$ when defining the lattice action in Chapter 3. The clover-leaf plaquette operator, $\mathcal{C}_{\mu\nu}$, provides an alternative to the elementary plaquette, and can be seen as a simple form of improvement. This was defined in Section 3.1.2 and we recall the definition here:

$$\begin{aligned}
\mathcal{C}_{\mu\nu}(x) \;\equiv\; & \frac{1}{8}\Big\{\, U_\mu(x)U_\nu(x+\hat{\mu})U_\mu^\dagger(x+\hat{\nu})U_\nu^\dagger(x)+ \\
& + U_\nu(x)U_\mu^\dagger(x+\hat{\nu}-\hat{\mu})U_\nu^\dagger(x-\hat{\mu})U_\mu(x-\hat{\mu}) + \\
& + U_\mu^\dagger(x-\hat{\mu})U_\nu^\dagger(x-\hat{\nu}-\hat{\mu})U_\mu(x-\hat{\nu}-\hat{\mu})U_\nu(x-\hat{\nu}) + \\
& + U_\nu^\dagger(x-\hat{\nu})U_\mu(x-\hat{\nu})U_\nu(x-\hat{\nu}+\hat{\mu})U_\mu^\dagger(x) - \text{h.c.}\,\Big\}\,.
\end{aligned} \tag{5.10}$$

One would like to set the scale in a way that does not depend crucially on microscopic details. To this purpose, in Fig. 5.12 we consider the $Sp(4)$ theory with $N_{\rm f} = 0$ and $N_{\rm as} = 4$, for two representative choices of β, and a representative choice of volume, $\tilde{V}$, and bare mass, $am_0^{\rm as}$, and we show $\mathcal{E}(t)$ and $\mathcal{W}(t)$ as functions of the flow time, t, by comparing explicitly the results obtained by adopting either the elementary or the clover-leaf plaquette as defining the lattice regularisation of the action. The plots illustrate the general trend evidenced elsewhere in the literature, according to which the function $\mathcal{W}(t)$ displays a milder dependence on the short distance regulator. In the following, we set the scale w_0 by conventionally setting $\mathcal{W}_0 = \frac{1}{2}C_2(F)$.

The topological charge density is defined as

$$q_L(x,t) \equiv \frac{1}{32\pi^2}\varepsilon^{\mu\nu\rho\sigma}\mathrm{Tr}\,[\mathcal{C}_{\mu\nu}(x,t)\mathcal{C}_{\rho\sigma}(x,t)]\,, \tag{5.11}$$

and the topological charge is $Q_L(t) \equiv \sum_x q_L(x,t)$, where, again, t is the flow time. In general, the topological charge on the lattice is not quantised, and in cases where it is the physical quantity of interest—for example because one is working towards a determination of the topological susceptibility, as in Ref. [16] and references therein—one needs to evolve to large t.

For the current purposes, we do not need a discretisation algorithm: what we want to verify is that there is no evidence of topological freezing, and to this purpose we perform three simple tests. In Fig. 5.13 we display the value of $Q_L(t = w_0^2)$ in the $Sp(4)$ theory coupled to $N_\mathrm{f} = 0$ and $N_\mathrm{as} = 4$ fermion species, for two values of the coupling, β, and a common value of the bare mass. We show how the topological charge evolves along the trajectories, and supplement it with a histogram displaying its distribution. Both visual tests confirm that there is no evidence of topological freezing. We can make these tests more quantitative by applying the standard Madras-Sokal windowing algorithm [117], and provide estimates of the integrated autocorrelation time τ_Q of the topological charge, which in both examples, as shown in Fig. 5.13, turns out to be many orders of magnitude smaller than the number of trajectories. Furthermore, fits of the histograms are compatible with a Gaussian distribution centred at $\langle Q_L(t = w_0^2)\rangle = 0$.

The main message from this section is that the behaviour of the Wilson flow and of the topological charge, computed using the new software based on Grid, and tested on GPU architecture machines, to examine the properties of the lattice $Sp(2N)$ gauge theory with $N = 2$, $N_\mathrm{f} = 0$, and $N_\mathrm{as} = 4$, provide results that are broadly comparable to those in the literature for related, though different, field theories. This suggests that the implementation of the simulation routines and of the observables are both consistent.

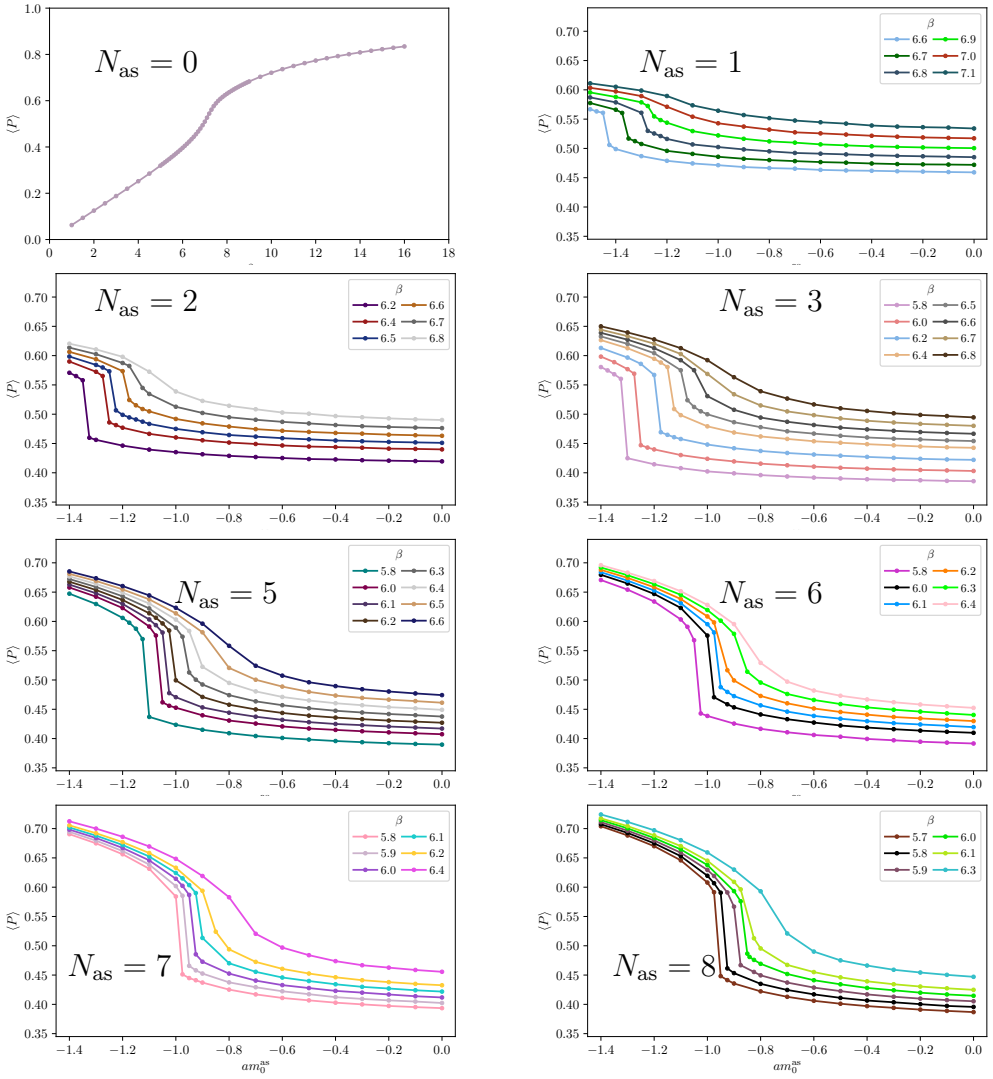

Figure 5.11 *Parameter scan in the $Sp(4)$ theory with $N_{\rm as} = 0 \ldots 8$ (left to right and top to bottom panels) fermions in the 2AS representation, obtained with ensembles generated from a cold start. For $N_{\rm as} > 0$, we show the value of the average plaquette, $\langle P \rangle$, as a function of the bare mass, for a few representative values of the coupling. For pure gauge, we just vary the value of β. The lattice size is $\tilde{V} = (8a)^4$ and the base mass is chosen in the range $-1.4 \leq am_0^{\rm as} \leq 0.0$ for $N_{\rm as} \geq 2$, and $-1.5 \leq am_0^{\rm as} \leq 0.0$ for $N_{\rm as} = 1$. For the pure gauge theory, the coupling is chosen to be $1.0 \leq \beta \leq 16.0$. For $N_{\rm as} = 1$, we have chosen $\beta = 7.1, 7.0, 6.9, 6.8, 6.7, 6.6$, while for $N_{\rm as} = 2$ we have $\beta = 6.8, 6.7, 6.6, 6.5, 6.4, 6.2$. For $N_{\rm as} = 3$, the coupling is $\beta = 6.8, 6.7, 6.6, 6.5, 6.4, 6.2, 6.0, 5.8$, while for $N_{\rm as} = 5$ we have chosen $\beta = 6.6, 6.5, 6.4, 6.3, 6.2, 6.1, 6.0, 5.8$. For $N_{\rm as} = 6$, $\beta = 6.4, 6.3, 6.2, 6.1, 6.0, 5.8$. For $N_{\rm as} = 7$, $\beta = 6.4, 6.2, 6.1, 6.0, 5.9, 5.8$ and for $N_{\rm as} = 8$, $\beta = 6.3, 6.1, 6.0, 5.9, 5.8, 5.7$.*

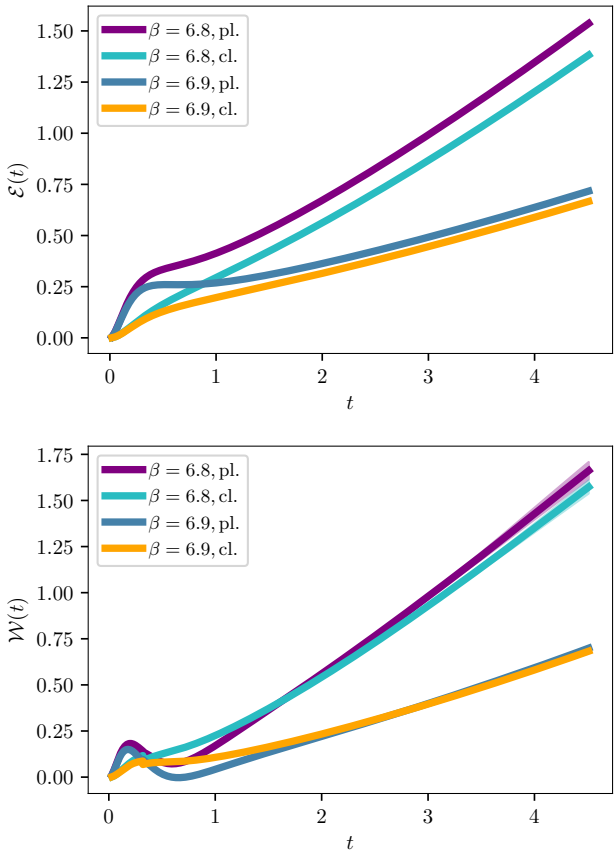

Figure 5.12 *Wilson Flow [14, 15] energy density $\mathcal{E}(t)$ (left panel) and $\mathcal{W}(t)$ (right), computed as in Refs. [10, 16], from the standard (pl) and the clover-leaf (cl) plaquette defined in Refs. [17, 18], for the $Sp(4)$ theory with $N_{\rm as} = 4$ fermions transforming in the 2-index antisymmetric representation. The lattice size is $\tilde{V} = (12a)^4$, and we display two representative choices of bare parameters, with $\beta = 6.8$ or 6.9 and common bare mass $am_0^{\rm as} = -0.8$. The time step is 0.01, $t_{max} = 4.5$ to reduce finite-size effects. Errors are computed by bootstrapping. We have chosen $\mathcal{W}_0 = \frac{1}{2}C_2(F)$ for the topological charge. The corresponding values of w_0 from the plaquette and the clover-leaf are $w_{0,pl.} = 1.485(3)$ and $w_{0,cl.} = 1.495(2)$ for $\beta = 6.8$ and $w_{0,pl.} = 2.005(2)$ and $w_{0,cl.} = 2.026(2)$ for $\beta = 6.9$. We have set $a = 1$, for notational convenience.*

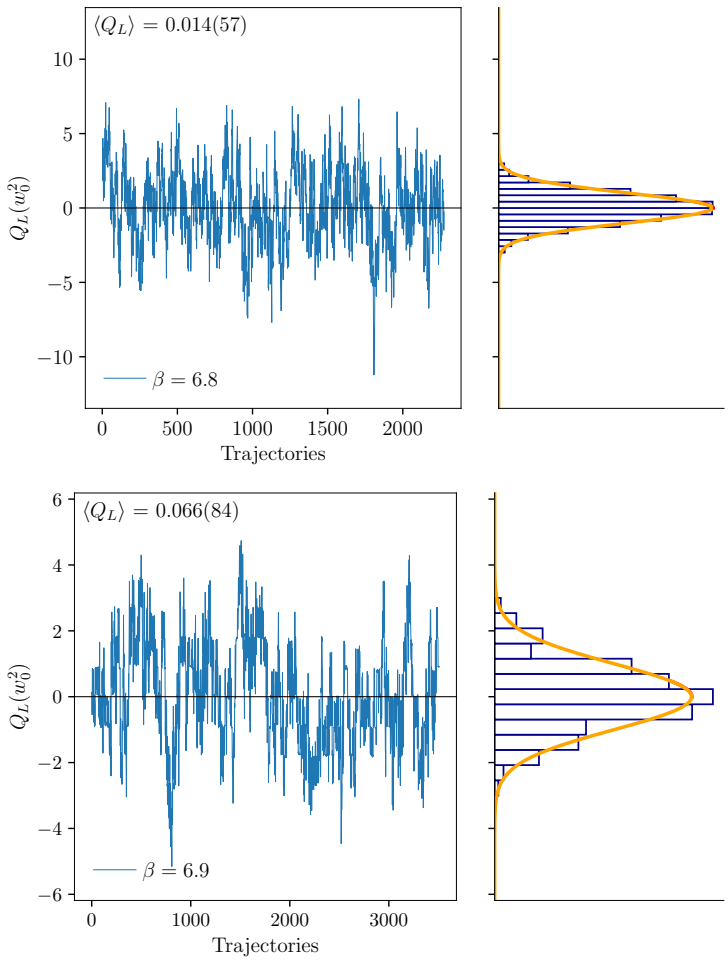

Figure 5.13 *Evolution with the ensemble trajectories of the topological charge* $Q_L(t = w_0^2) \equiv \sum_x \frac{1}{32\pi^2} \varepsilon^{\mu\nu\rho\sigma} \mathrm{Tr}\,[\mathcal{C}_{\mu\nu}(x)\mathcal{C}_{\rho\sigma}(x)]$*, computed (without rounding) at flow time* $t = w_0^2$ *for the* $Sp(4)$ *theory with* $N_{\mathrm{as}} = 4$ *fermions transforming in the 2-index antisymmetric representation. The lattice size is* $\tilde{V} = (12a)^4$*. The lattice parameters characterising the ensembles are* $\beta = 6.8$ *(top panel) and* $\beta = 6.9$ *(bottom), with bare mass* $am_0^{\mathrm{as}} = -0.8$*. The histograms of the measurements (right panels) are compatible with a normal distribution centred at zero, with reduced chi-square* $\chi^2/N_{\mathrm{d.o.f}} = \tilde{\chi}^2 = 1.1$ *for both panels. The integrated autocorrelation time computed using the Madras-Sokal windowing algorithm as in Ref. [16] is* $\tau_Q = 7.11(64)$ *(top) and* $\tau_Q = 59.58(92)$ *(bottom).*

Chapter 6

Conclusions

This thesis discusses some of the progress made towards the understanding of theories beyond the Standard Model on the lattice, in particular models of composite Higgs, and conformal field theories. We have shown results for an $SU(4)$ gauge theory, close to a model of partial compositeness, and an $Sp(4)$ theory that could lie on the lower edge of the conformal window.

The $SU(4)$ model, studied in Chapter 4, allows us to understand the dynamics of partial compositeness better, by extending the effort started in Ref. [13] at a reasonable computational cost. In order to make contact with the phenomenology of these theories from a lattice perspective, the systematics related to the computation of the spectrum and to the extrapolation to the chiral limit need to be under control. Our analysis has been developed in this context. We have explored the perturbative structure of the theory, extending previous computations of the critical mass [12, 52, 95–97] to the case of multiple fermionic representations. We have computed the self-energy of a fermion in a given representation, focusing on the dynamical effects due to the presence of more fermionic fields in a different representation of the gauge group. While leaving a clear footprint, the second representation has

only a minor numerical impact on the value of the critical mass. This result, while perturbative, found a counterpart at the non-perturbative level in the outcome of our simulations, as it is shown in Tables C.2–C.4. By approaching the chiral limit in a given representation, in fact, we found a weak dependence on the bare parameters of the other one. The extrapolation to the chiral limit was based on several ensembles that were generated for this study. This task was hindered by a strong autocorrelation affecting observables built from the fermion fields in the fundamental representation, the lightest in terms of pseudoscalar masses. A great portion of this work focused on the extraction of the spectrum, a crucial task in order to understand if these models are realistic from a phenomenological perspective. We have shown that the 2AS sector is characterised by complicated dynamics, due to the interplay between different representations, and the lack of selection rules dictated by discrete symmetries. We have found operator smearing to be essential, in this context, to provide a reliable analysis of the lattice data. In our analysis, we have taken advantage of recent progresses [103, 105] in the numerical solution of the inverse problem that allow precise reconstructions of smeared spectral densities. Our approach, introduced in Ref. [105], yields spectral densities smeared with a chosen function and with controlled systematics. Due to these features it was possible, for the first time, to explore in this work the extraction of finite volume energies from fits of spectral densities. Our results, compared to other established approaches, provide complementary insights and fully compatible results.

Encouraged by these conclusions, we invoke the possibility of extending this computational setup to the study of baryonic operators, as well as to other theories of composite Higgs. Our choices, both in terms of software [55, 101] and computational framework, are general and easy to adapt for the study of other theories, whether they contain different number of colors, fermionic content or gauge groups. Moreover, our work clarified technical aspects of the partial compositeness dynamics: this important step will allow moving towards studies of more phenomenological relevance. Theories of partial compositeness provide a rich set of new particles, from pseudo Goldstone bosons to heavy-quark partners, that are charged under the Standard Model and could be important for direct and indirect search of new physics. The extraction of spectral densities, validated in this context by our work, can be used not only to extract energy levels but also to directly compute inclusive cross-sections [104, 118], a possibility that we leave for future studies. The knowledge of inclusive

processes can be important for the indirect search of new physics, with particles from the new sector leaving footprints in observables precisely measured both at present and future colliders.

Another step done in this work, towards a better understanding of the composite Higgs dynamics, has been the developing of the necessary software to perform simulations of gauge theories based on $Sp(2N)$ with the lattice library Grid. $Sp(2N)$ theories are in fact relevant for the composite Higgs scenario, as well as many other extensions to the Standard model. The future prospects for this project rely on the high performance and platform-independence of Grid, which will allow to perform simulations on many exascale architectures. In this thesis, we have discussed details of the implementation in Section 3.2.5 and perform extensive tests on the algorithm in Section 5.1. As a case study, we explored the phase structure of $Sp(4)$ with four fermions in the two-index antisymmetric representation, a model that could lie on the lower edge of the conformal window. By developing the numerical tools needed to explore these models, this work sets the stage for future studies on the conformal window in $Sp(2N)$ gauge theories.

Appendix A

Group theory

A.1 Conventions

The groups that are discussed, or at least mentioned in this work are $SU(N_c)$ and, for even $N_c = 2N$, its subgroups $Sp(2N)$ and $SO(2N)$. The normalisation of their generators in the representation R are fixed by the following expression

$$[T_R^a, T_R^b] = i f^{abc} T_R^c \,, \tag{A.1}$$

where the structure constant are fully antisymmetric. We further establish the following conventions

$$\mathrm{Tr}\left(T_R^a T_R^b\right) = \lambda_R \, \delta^{ab} \,, \tag{A.2}$$

$$\sum_a \left(T_R^a T_R^a\right)_{ij} = C_2(R) \, \delta_{ij} \,, \tag{A.3}$$

implying

$$\lambda_R = \frac{\dim_{\mathrm{R}}}{\dim_{\mathrm{Adj}}} C_2(R) \,. \tag{A.4}$$

We will use $\lambda_F = \frac{1}{2}$.

A.2 On Unbroken Groups

In this Section we describe the features of groups that commonly arise in the building of model building for BSM physics. From the discussion in Ref. 1.5 about symmetry breaking patterns, it is clear that great interest lies on certain subgroups of $SU(2N)$ leaving invariant respectively and antisymmetric and a symmetric form. These are $Sp(2N)$ and $SO(2N)$.

A.2.1 $SU(N_c)$

$SU(N)$, the special unitary group of degree N. The explicit form of the generators that were used in this work is as follows. For the fundamental representation, the $N-1$ Cartan generators are defined as

$$T^k_{(\text{Fund})} = \frac{1}{\sqrt{2k(k+1)}} \text{diag}(\underbrace{1,\ldots,1}_{k \text{ terms}}, -k, \underbrace{0,\ldots,0}_{N-k-1 \text{ terms}}), \tag{A.5}$$

for $1 \leq k \leq N-1$, whereas the remaining $N^2 - N$ non-diagonal generators are defined as

$$\left(T^{(i,j;1)}_{(\text{Fund})}\right)_{a,b} = \frac{1}{2}\left(\delta_{a,i}\delta_{b,j} + \delta_{a,j}\delta_{b,i}\right), \tag{A.6}$$

$$\left(T^{(i,j;2)}_{(\text{Fund})}\right)_{a,b} = \frac{1}{2i}\left(\delta_{a,i}\delta_{b,j} - \delta_{a,j}\delta_{b,i}\right), \tag{A.7}$$

for $1 \leq i < j \leq N$. Note that, with these conventions, for $N = 2$ the generators in the fundamental representation reduce to $\frac{1}{2}\sigma^a$ (σ^a denoting a Pauli matrix), while for $N = 3$ the generators in the fundamental representation are $\frac{1}{2}\lambda^a$ (where λ^a denotes a Gell-Mann matrix).

R	$\dim(R)$	λ_R	$C_2(R)$
Fund	N	$\frac{1}{2}$	$\frac{N^2-1}{2N}$
2AS	$\frac{N(N-1)}{2}$	$\frac{N-2}{2}$	$C_2(\text{Fund})\frac{2(N-2)}{N-1}$

Table A.1 *Group-theoretical factors for $SU(N)$, used in Chapter 4.*

Explicitly, with these conventions the $SU(4)$ generators in the fundamental

representation take the form:

$$T^1_{(\text{Fund})} = \frac{1}{2}\begin{pmatrix} 0 & 1 & 0 & 0 \\ 1 & 0 & 0 & 0 \\ 0 & 0 & 0 & 0 \\ 0 & 0 & 0 & 0 \end{pmatrix}, \quad T^2_{(\text{Fund})} = \frac{1}{2}\begin{pmatrix} 0 & -i & 0 & 0 \\ i & 0 & 0 & 0 \\ 0 & 0 & 0 & 0 \\ 0 & 0 & 0 & 0 \end{pmatrix},$$

$$T^3_{(\text{Fund})} = \frac{1}{2}\begin{pmatrix} 1 & 0 & 0 & 0 \\ 0 & -1 & 0 & 0 \\ 0 & 0 & 0 & 0 \\ 0 & 0 & 0 & 0 \end{pmatrix}, T^4_{(\text{Fund})} = \frac{1}{2}\begin{pmatrix} 0 & 0 & 1 & 0 \\ 0 & 0 & 0 & 0 \\ 1 & 0 & 0 & 0 \\ 0 & 0 & 0 & 0 \end{pmatrix},$$

$$T^5_{(\text{Fund})} = \frac{1}{2}\begin{pmatrix} 0 & 0 & -i & 0 \\ 0 & 0 & 0 & 0 \\ i & 0 & 0 & 0 \\ 0 & 0 & 0 & 0 \end{pmatrix}, \quad T^6_{(\text{Fund})} = \frac{1}{2}\begin{pmatrix} 0 & 0 & 0 & 0 \\ 0 & 0 & 1 & 0 \\ 0 & 1 & 0 & 0 \\ 0 & 0 & 0 & 0 \end{pmatrix}, \tag{A.8}$$

$$T^7_{(\text{Fund})} = \frac{1}{2}\begin{pmatrix} 0 & 0 & 0 & 0 \\ 0 & 0 & -i & 0 \\ 0 & i & 0 & 0 \\ 0 & 0 & 0 & 0 \end{pmatrix}, \quad T^8_{(\text{Fund})} = \frac{1}{2\sqrt{3}}\begin{pmatrix} 1 & 0 & 0 & 0 \\ 0 & 1 & 0 & 0 \\ 0 & 0 & -2 & 0 \\ 0 & 0 & 0 & 0 \end{pmatrix},$$

$$T^9_{(\text{Fund})} = \frac{1}{2}\begin{pmatrix} 0 & 0 & 0 & 1 \\ 0 & 0 & 0 & 0 \\ 0 & 0 & 0 & 0 \\ 1 & 0 & 0 & 0 \end{pmatrix}, \quad T^{10}_{(\text{Fund})} = \frac{1}{2}\begin{pmatrix} 0 & 0 & 0 & -i \\ 0 & 0 & 0 & 0 \\ 0 & 0 & 0 & 0 \\ i & 0 & 0 & 0 \end{pmatrix},$$

$$T^{11}_{(\text{Fund})} = \frac{1}{2}\begin{pmatrix} 0 & 0 & 0 & 0 \\ 0 & 0 & 0 & 1 \\ 0 & 0 & 0 & 0 \\ 0 & 1 & 0 & 0 \end{pmatrix}, \quad T^{12}_{(\text{Fund})} = \frac{1}{2}\begin{pmatrix} 0 & 0 & 0 & 0 \\ 0 & 0 & 0 & -i \\ 0 & 0 & 0 & 0 \\ 0 & i & 0 & 0 \end{pmatrix},$$

$$T^{13}_{(\text{Fund})} = \frac{1}{2}\begin{pmatrix} 0 & 0 & 0 & 0 \\ 0 & 0 & 0 & 0 \\ 0 & 0 & 0 & 1 \\ 0 & 0 & 1 & 0 \end{pmatrix}, \quad T^{14}_{(\text{Fund})} = \frac{1}{2}\begin{pmatrix} 0 & 0 & 0 & 0 \\ 0 & 0 & 0 & 0 \\ 0 & 0 & 0 & -i \\ 0 & 0 & i & 0 \end{pmatrix},$$

$$T^{15}_{(\text{Fund})} = \frac{1}{2\sqrt{6}}\begin{pmatrix} 1 & 0 & 0 & 0 \\ 0 & 1 & 0 & 0 \\ 0 & 0 & 1 & 0 \\ 0 & 0 & 0 & -3 \end{pmatrix},$$

while the $SU(4)$ generators in the two-index antisymmetric representation read:

$$T^1_{(2AS)} = \frac{1}{2}\begin{pmatrix} 0&0&0&0&0&0\\ 0&0&1&0&0&0\\ 0&1&0&0&0&0\\ 0&0&0&0&1&0\\ 0&0&0&1&0&0\\ 0&0&0&0&0&0 \end{pmatrix}, \qquad T^2_{(2AS)} = \frac{1}{2}\begin{pmatrix} 0&0&0&0&0&0\\ 0&0&-i&0&0&0\\ 0&i&0&0&0&0\\ 0&0&0&0&-i&0\\ 0&0&0&i&0&0\\ 0&0&0&0&0&0 \end{pmatrix}, \quad (A.9)$$

$$T^3_{(2AS)} = \frac{1}{2}\begin{pmatrix} 0&0&0&0&0&0\\ 0&1&0&0&0&0\\ 0&0&-1&0&0&0\\ 0&0&0&1&0&0\\ 0&0&0&0&-1&0\\ 0&0&0&0&0&0 \end{pmatrix}, T^4_{(2AS)} = \frac{1}{2}\begin{pmatrix} 0&0&-1&0&0&0\\ 0&0&0&0&0&0\\ -1&0&0&0&0&0\\ 0&0&0&0&0&1\\ 0&0&0&0&0&0\\ 0&0&0&1&0&0 \end{pmatrix},$$

$$T^5_{(2AS)} = \frac{1}{2}\begin{pmatrix} 0&0&i&0&0&0\\ 0&0&0&0&0&0\\ -i&0&0&0&0&0\\ 0&0&0&0&0&-i\\ 0&0&0&0&0&0\\ 0&0&0&i&0&0 \end{pmatrix}, \qquad T^6_{(2AS)} = \frac{1}{2}\begin{pmatrix} 0&1&0&0&0&0\\ 1&0&0&0&0&0\\ 0&0&0&0&0&0\\ 0&0&0&0&0&0\\ 0&0&0&0&0&1\\ 0&0&0&0&1&0 \end{pmatrix},$$

$$T^7_{(2AS)} = \frac{1}{2}\begin{pmatrix} 0&-i&0&0&0&0\\ i&0&0&0&0&0\\ 0&0&0&0&0&0\\ 0&0&0&0&0&0\\ 0&0&0&0&0&-i\\ 0&0&0&0&i&0 \end{pmatrix}, \qquad T^8_{(2AS)} = \frac{1}{\sqrt{12}}\begin{pmatrix} 2&0&0&0&0&0\\ 0&-1&0&0&0&0\\ 0&0&-1&0&0&0\\ 0&0&0&1&0&0\\ 0&0&0&0&1&0\\ 0&0&0&0&0&-2 \end{pmatrix},$$

$$T^9_{(2AS)} = \frac{1}{2}\begin{pmatrix} 0&0&0&0&-1&0\\ 0&0&0&0&0&-1\\ 0&0&0&0&0&0\\ 0&0&0&0&0&0\\ -1&0&0&0&0&0\\ 0&-1&0&0&0&0 \end{pmatrix}, \qquad T^{10}_{(2AS)} = \frac{1}{2}\begin{pmatrix} 0&0&0&0&i&0\\ 0&0&0&0&0&i\\ 0&0&0&0&0&0\\ 0&0&0&0&0&0\\ -i&0&0&0&0&0\\ 0&-i&0&0&0&0 \end{pmatrix},$$

$$T^{11}_{(2AS)} = \frac{1}{2}\begin{pmatrix} 0&0&0&1&0&0\\ 0&0&0&0&0&0\\ 0&0&0&0&0&-1\\ 1&0&0&0&0&0\\ 0&0&0&0&0&0\\ 0&0&-1&0&0&0 \end{pmatrix}, \qquad T^{12}_{(2AS)} = \frac{1}{2}\begin{pmatrix} 0&0&0&-i&0&0\\ 0&0&0&0&0&0\\ 0&0&0&0&0&i\\ i&0&0&0&0&0\\ 0&0&0&0&0&0\\ 0&0&-i&0&0&0 \end{pmatrix}, \quad (A.10)$$

$$T^{13}_{\rm 2AS} = \frac{1}{2}\begin{pmatrix} 0&0&0&0&0&0\\ 0&0&0&1&0&0\\ 0&0&0&0&1&0\\ 0&1&0&0&0&0\\ 0&0&1&0&0&0\\ 0&0&0&0&0&0 \end{pmatrix}, \quad T^{14}_{\rm (2AS)} = \frac{1}{2}\begin{pmatrix} 0&0&0&0&0&0\\ 0&0&0&-i&0&0\\ 0&0&0&0&-i&0\\ 0&i&0&0&0&0\\ 0&0&i&0&0&0\\ 0&0&0&0&0&0 \end{pmatrix},$$

$$T^{15}_{\rm (2AS)} = \frac{1}{\sqrt{6}}\begin{pmatrix} 1&0&0&0&0&0\\ 0&1&0&0&0&0\\ 0&0&1&0&0&0\\ 0&0&0&-1&0&0\\ 0&0&0&0&-1&0\\ 0&0&0&0&0&-1 \end{pmatrix}.$$

A.2.2 $Sp(2N)$

We denote as $Sp(2N)$ the subgroup of $SU(2N)$ preserving the norm induced by the antisymmetric matrix Ω,

$$\Omega = \begin{pmatrix} 0 & \mathbb{1}_N \\ -\mathbb{1}_N & 0 \end{pmatrix} , \tag{A.11}$$

where $\mathbb{1}_N$ is the $N \times N$ identity matrix. This definition can be converted into a constraint on the group element U

$$U^T \Omega U = \Omega \, . \tag{A.12}$$

Due to unitarity, the previous condition can be also written as

$$U\Omega = \Omega U^* \, , \tag{A.13}$$

which implies the following block structure

$$U = \begin{pmatrix} A & B \\ -B^* & A^* \end{pmatrix} , \tag{A.14}$$

where Eq. (A.12) implies, for A and B, that

$$AB^T = BA^T \, , \qquad AA^\dagger + BB^\dagger = \mathbb{1}_N \, . \tag{A.15}$$

The algebra can be defined by expanding $U\Omega = \Omega U^*$ in terms of the hermitian generators t^a, i.e. $U = \exp(i\omega^a t^a)$ for real parameters ω^a. We arrive at the following condition on the generic element of the algebra $T = \sum_a \omega^a t^a$

$$T\Omega = -\Omega T^* \,, \tag{A.16}$$

which also implies that

$$T = \begin{pmatrix} X & Y \\ Y^* & -X^* \end{pmatrix} \,. \tag{A.17}$$

Hermiticity impose the conditions $X = X^\dagger$ and $Y = Y^T$. The number of degrees of freedom is then $2N(N+1)$, the dimension of the group.

Implementation of the generators in the fundamental

We show how the generators can be implemented in a numerical library, following what has been done in Grid. Let $T^a_{\rm f}$ be the generators of the Lie Algebra of $Sp(2N)$ in the fundamental representation, $a = 1, \dots \dim(Sp(2N)) = 2N^2+N$. When implemented as hermitian, they follow the block structure of Eq. (A.17). The following scheme can therefore be used. The $2N^2$ off-diagonal generators are identified by the following six relations among their matrix elements

$$T^a_{i,i+N} = T^a_{i+N,i} = \frac{1}{2} \,, \qquad i = 1, \dots, N \,, \tag{A.18}$$

with $a = 1, \dots, N(N-1)/2$,

$$T^a_{i,i+N} = -T^a_{i+N,i} = \frac{i}{2} \,, \qquad i = 1, \dots, N \,, \tag{A.19}$$

with $a = N(N-1)/2+1, \dots, N(N-1)$,

$$T^a_{i,j} = t^a_{j,i} = -T^a_{i+N,j+N} = -t^a_{j+N,i+N} = \frac{1}{2\sqrt{2}} \,, \qquad i = 1, \dots N-1 \,, \qquad i < j \leq N \,, \tag{A.20}$$

with $a = N(N-1)+1, \dots, 3N(N-1)/2$,

$$T^a_{i,j} = -t^a_{j,i} = T^a_{i+N,j+N} = -t^a_{j+N,i+N} = \frac{i}{2\sqrt{2}} \,, \qquad i = 1, \dots, N-1 \,, \qquad i < j \leq N \,, \tag{A.21}$$

with $a = 3N(N-1)/2+1, \ldots, 2N(N-1)$,

$$T^a_{i,j+N} = T^a_{j,i+N} = T^a_{i+N,j} = T^a_{j+N,i} = \frac{1}{2\sqrt{2}}\,, \qquad i = 1, \ldots, N{-}1, \qquad i < j \leq N{-}1\,, \tag{A.22}$$

with $a = 2N(N-1)+1, \ldots, 2N(N-1)+N$,

$$T^a_{i,j+N} = T^a_{j,i+N} = -T^a_{i+N,j} = -T^a_{j+N,i} = \frac{i}{2\sqrt{2}}\,, \qquad i = 1, \ldots, N{-}1\,, \qquad i < j \leq N{-}1\,. \tag{A.23}$$

with $a = 2N(N{-}1){+}N{+}1, \ldots, 2N(N{-}1){+}2N$. The remaining N generators in the Cartan subalgebra are

$$(t^a)_{i,i} = -(t^a)_{i+N,i+N} = \frac{1}{2}\,, \qquad i = 1, \ldots N\,, \tag{A.24}$$

with $a = 2N(N-1)+2N+1, \ldots, 2N(N-1)+3N = 2N^2+N$. It is useful to provide an explicit representation for $2N = 4$:

$$\begin{aligned}
t^1_{\rm f} &= \frac{1}{2\sqrt{2}}\begin{pmatrix} 0 & 1 & 0 & 0 \\ 1 & 0 & 0 & 0 \\ 0 & 0 & 0 & -1 \\ 0 & 0 & -1 & 0 \end{pmatrix} & t^6_{\rm f} &= \frac{1}{2}\begin{pmatrix} 0 & 0 & 0 & 0 \\ 0 & 0 & 0 & 1 \\ 0 & 0 & 0 & 0 \\ 0 & 1 & 0 & 0 \end{pmatrix} \\
t^2_{\rm f} &= \frac{1}{2\sqrt{2}}\begin{pmatrix} 0 & i & 0 & 0 \\ -i & 0 & 0 & 0 \\ 0 & 0 & 0 & i \\ 0 & 0 & -i & 0 \end{pmatrix} & t^7_{\rm f} &= \frac{1}{2}\begin{pmatrix} 0 & 0 & i & 0 \\ 0 & 0 & 0 & 0 \\ -i & 0 & 0 & 0 \\ 0 & 0 & 0 & 0 \end{pmatrix} \\
t^3_{\rm f} &= \frac{1}{2\sqrt{2}}\begin{pmatrix} 0 & 0 & 0 & 1 \\ 0 & 0 & 1 & 0 \\ 0 & 1 & 0 & 0 \\ 1 & 0 & 0 & 0 \end{pmatrix} & t^8_{\rm f} &= \frac{1}{2}\begin{pmatrix} 0 & 0 & 0 & 0 \\ 0 & 0 & 0 & i \\ 0 & 0 & 0 & 0 \\ 0 & -i & 0 & 0 \end{pmatrix} \\
t^4_{\rm f} &= \frac{1}{2\sqrt{2}}\begin{pmatrix} 0 & 0 & 0 & i \\ 0 & 0 & i & 0 \\ 0 & -i & 0 & 0 \\ -i & 0 & 0 & 0 \end{pmatrix} & t^9_{\rm f} &= \frac{1}{2}\begin{pmatrix} 1 & 0 & 0 & 0 \\ 0 & 0 & 0 & 0 \\ 0 & 0 & -1 & 0 \\ 0 & 0 & 0 & 0 \end{pmatrix} \\
t^5_{\rm f} &= \frac{1}{2}\begin{pmatrix} 0 & 0 & 1 & 0 \\ 0 & 0 & 0 & 0 \\ 1 & 0 & 0 & 0 \\ 0 & 0 & 0 & 0 \end{pmatrix} & t^{10}_{\rm f} &= \frac{1}{2}\begin{pmatrix} 0 & 0 & 0 & 0 \\ 0 & 1 & 0 & 0 \\ 0 & 0 & 0 & 0 \\ 0 & 0 & 0 & -1 \end{pmatrix}\,.
\end{aligned} \tag{A.25}$$

A.3 Isospin Generators for $SO(4)$

The isospin group of the 2AS sector in the 2-flavor Ferretti model is $SO(4)$. The Goldstone bosons arising from the $SU(4)/SO(4)$ cosets transform in a 9-dimensional representation of the isospin, whose generators X_n, $n = 1, \dots 6$ are listed in this appendix. These are obtained according to the convention of [13] regarding the generators and the structure constants of $SU(4)$.

$$X_1 = -\frac{i}{2}\begin{pmatrix} 0 & -2 & 0 & 0 & 0 & 0 & 0 & 0 & 0 \\ 2 & 0 & 0 & 0 & 0 & 0 & 0 & 0 & 0 \\ 0 & 0 & 0 & 1 & 0 & 0 & 0 & 0 & 0 \\ 0 & 0 & -1 & 0 & 0 & 0 & 0 & 0 & 0 \\ 0 & 0 & 0 & 0 & 0 & 0 & 0 & 0 & 0 \\ 0 & 0 & 0 & 0 & 0 & 0 & 1 & 0 & 0 \\ 0 & 0 & 0 & 0 & 0 & -1 & 0 & 0 & 0 \\ 0 & 0 & 0 & 0 & 0 & 0 & 0 & 0 & 0 \\ 0 & 0 & 0 & 0 & 0 & 0 & 0 & 0 & 0 \end{pmatrix}, \tag{A.26}$$

$$X_2 = -\frac{i}{2}\begin{pmatrix} 0 & 0 & 0 & 1 & 0 & 0 & 0 & 0 & 0 \\ 0 & 0 & 1 & 0 & 0 & 0 & 0 & 0 & 0 \\ 0 & -1 & 0 & 0 & -\sqrt{3} & 0 & 0 & 0 & 0 \\ -1 & 0 & 0 & 0 & 0 & 0 & 0 & 0 & 0 \\ 0 & 0 & \sqrt{3} & 0 & 0 & 0 & 0 & 0 & 0 \\ 0 & 0 & 0 & 0 & 0 & 0 & 0 & 1 & 0 \\ 0 & 0 & 0 & 0 & 0 & 0 & 0 & 0 & 0 \\ 0 & 0 & 0 & 0 & 0 & -1 & 0 & 0 & 0 \\ 0 & 0 & 0 & 0 & 0 & 0 & 0 & 0 & 0 \end{pmatrix}, \tag{A.27}$$

$$X_3 = -\frac{i}{2}\begin{pmatrix} 0 & 0 & 1 & 0 & 0 & 0 & 0 & 0 & 0 \\ 0 & 0 & 0 & -1 & 0 & 0 & 0 & 0 & 0 \\ -1 & 0 & 0 & 0 & 0 & 0 & 0 & 0 & 0 \\ 0 & 1 & 0 & 0 & -\sqrt{3} & 0 & 0 & 0 & 0 \\ 0 & 0 & 0 & \sqrt{3} & 0 & 0 & 0 & 0 & 0 \\ 0 & 0 & 0 & 0 & 0 & 0 & 0 & 0 & 0 \\ 0 & 0 & 0 & 0 & 0 & 0 & 0 & 1 & 0 \\ 0 & 0 & 0 & 0 & 0 & 0 & -1 & 0 & 0 \\ 0 & 0 & 0 & 0 & 0 & 0 & 0 & 0 & 0 \end{pmatrix}, \tag{A.28}$$

$$X_4 = -\frac{i}{2}\begin{pmatrix} 0 & 0 & 0 & 0 & 0 & 0 & 1 & 0 & 0 \\ 0 & 0 & 0 & 0 & 0 & 1 & 0 & 0 & 0 \\ 0 & 0 & 0 & 0 & 0 & 0 & 0 & 1 & 0 \\ 0 & 0 & 0 & 0 & 0 & 0 & 0 & 0 & 0 \\ 0 & 0 & 0 & 0 & 0 & 1/\sqrt{3} & 0 & 0 & 0 \\ 0 & -1 & 0 & 0 & -1/\sqrt{3} & 0 & 0 & 0 & -2\sqrt{2/3} \\ -1 & 0 & 0 & 0 & 0 & 0 & 0 & 0 & 0 \\ 0 & 0 & -1 & 0 & 0 & 0 & 0 & 0 & 0 \\ 0 & 0 & 0 & 0 & 0 & 2\sqrt{2/3} & 0 & 0 & 0 \end{pmatrix}, \quad \text{(A.29)}$$

$$X_5 = -\frac{i}{2}\begin{pmatrix} 0 & 0 & 0 & 0 & 0 & 1 & 0 & 0 & 0 \\ 0 & 0 & 0 & 0 & 0 & 0 & -1 & 0 & 0 \\ 0 & 0 & 0 & 0 & 0 & 0 & 0 & 0 & 0 \\ 0 & 0 & 0 & 0 & 0 & 0 & 0 & 1 & 0 \\ 0 & 0 & 0 & 0 & 0 & 0 & 1/\sqrt{3} & 0 & 0 \\ -1 & 0 & 0 & 0 & 0 & 0 & 0 & 0 & 0 \\ 0 & 1 & 0 & 0 & -1/\sqrt{3} & 0 & 0 & 0 & -2\sqrt{2/3} \\ 0 & 0 & 0 & -1 & 0 & 0 & 0 & 0 & 0 \\ 0 & 0 & 0 & 0 & 0 & 0 & 2\sqrt{2/3} & 0 & 0 \end{pmatrix}, \quad \text{(A.30)}$$

$$X_6 = -\frac{i}{2}\begin{pmatrix} 0 & 0 & 0 & 0 & 0 & 0 & 0 & 0 & 0 \\ 0 & 0 & 0 & 0 & 0 & 0 & 0 & 0 & 0 \\ 0 & 0 & 0 & 0 & 0 & 1 & 0 & 0 & 0 \\ 0 & 0 & 0 & 0 & 0 & 0 & 1 & 0 & 0 \\ 0 & 0 & 0 & 0 & 0 & 0 & 0 & -2/\sqrt{3} & 0 \\ 0 & 0 & -1 & 0 & 0 & 0 & 0 & 0 & 0 \\ 0 & 0 & 0 & -1 & 0 & 0 & 0 & 0 & 0 \\ 0 & 0 & 0 & 0 & 2/\sqrt{3} & 0 & 0 & 0 & -2\sqrt{2/3} \\ 0 & 0 & 0 & 0 & 0 & 0 & 0 & 2\sqrt{2/3} & 0 \end{pmatrix} \quad \text{(A.31)}$$

Appendix B

Gamma Matrices and Euclidean rotation

In this Appendix, we set the notation for the γ-matrices, both with the Minkowski and the Euclidean metric. We discuss the convention used in the Software and conversions with other basis. Alongside, it is convenient to discuss the transformation from Minkowski to Euclidean.

We define the Euclidean γ–matrices as the generators γ_μ^E, $\mu = 1, 2, 3, 4$ of a Clifford algebra satisfying

$$\gamma_\mu^E \gamma_\nu^E + \gamma_\nu^E \gamma_\mu^E = 2\delta_{\mu\nu} \mathbb{1}_4 \,. \tag{B.1}$$

We define γ_5, at this stage, up to a complex factor c_E

$$\gamma_5^E = c_E \; \gamma_1^E \gamma_2^E \gamma_3^E \gamma_4^E \,. \tag{B.2}$$

This definition satisfies

$$\gamma_5^E \gamma_\mu^E = -\gamma_\mu^E \gamma_5^E \,, \tag{B.3}$$

and

$$(\gamma_5^E)^2 = c_E^2 \, \mathbb{1} \; . \tag{B.4}$$

If $c_E^2 = 1$, the matrix γ_5^E can be used to form the projectors

$$P_{L/R} = \frac{\mathbb{1} \pm \gamma_5^E}{2} \; . \tag{B.5}$$

B.1 From Minkowski to Euclidean

The Dirac action in Minkowski space is

$$iS = i \int d^4x \; \bar{\psi}(i\gamma_\mu \partial^m u - m)\psi \; , \tag{B.6}$$

where we do not specify the representation of the γ–matrices. We define the Euclidean fields

$$\psi_E(x_E) = \psi(x) \; , \tag{B.7}$$

and we perform a Wick rotation, resulting in

$$x_4^E = ix^0 \; , \qquad \partial_4^E = -i\partial_0 \; , \qquad \partial_i^E = \partial_i \; , \tag{B.8}$$

With this premise, the following relation between Euclidean and Minkowskian gamma matrices

$$\gamma_4^E = \gamma_0 \qquad \gamma_{1,2,3}^E = i \, \gamma_{1,2,3} \; , \tag{B.9}$$

returns the expression for the Euclidean action,

$$iS \to -S_E = \int d^4x^E \; \bar{\psi}^E \left(\gamma_\mu^E \partial_\mu^E + m\right) \psi^E \; , \tag{B.10}$$

where $\mu = 1, 2, 3, 4$. Eq. B.9 implies that if $\gamma_{1,2,3}^E$ are hermitian, the correspondent quantities in Minkowski space will be anti–hermitian. Concerning γ_5, suppose we have

$$\gamma_5 = c \; \gamma_0 \gamma_1 \gamma_2 \gamma_3 \; . \tag{B.11}$$

Then, Eq. B.9 imply

$$\gamma_5 = i \, c \; \gamma_4^E \gamma_1^E \gamma_2^E \gamma_3^E = -i \, c \; \gamma_1^E \gamma_2^E \gamma_3^E \gamma_4^E \; . \tag{B.12}$$

Therefore if we define $-ic = c_E$ we have

$$\gamma_5 = \gamma_5^E \ . \tag{B.13}$$

We use $c = i$ and $c_E = 1$. We now give an explicit representation for the γ-matrices

B.2 An explicit representation of the Euclidean γ–matrices

We define the DeGrand-Rossi basis as follows,

$$\begin{aligned} \gamma_1^{DR} &= \begin{pmatrix} 0 & i\sigma_1 \\ -i\sigma_1 & 0 \end{pmatrix} \qquad \gamma_2^{DR} = \begin{pmatrix} 0 & -i\sigma_2 \\ i\sigma_2 & 0 \end{pmatrix} \\ \gamma_3^{DR} &= \begin{pmatrix} 0 & i\sigma_3 \\ -i\sigma_1 & 0 \end{pmatrix} \qquad \gamma_4^{DR} = \begin{pmatrix} 0 & I \\ I & 0 \end{pmatrix} \ . \end{aligned} \tag{B.14}$$

This is the basis used in Grid. γ_5 is defined to be

$$\gamma_5^{DR} = \gamma_1^{DR}\gamma_2^{DR}\gamma_3^{DR}\gamma_4^{DR} = \begin{pmatrix} I & 0 \\ 0 & -I \end{pmatrix} \ . \tag{B.15}$$

The correspondent γ–matrices back to Minkowski are obtained by Eq. B.9

$$\begin{aligned} \gamma_1^{DR} \to \gamma_1 &= \begin{pmatrix} 0 & \sigma_1 \\ -\sigma_1 & 0 \end{pmatrix} = -i\gamma_1^{DR} \\ \gamma_2^{DR} \to \gamma_2 &= \begin{pmatrix} 0 & -\sigma_2 \\ \sigma_2 & 0 \end{pmatrix} = -i\gamma_2^{DR} \\ \gamma_3^{DR} \to \gamma_3 &= \begin{pmatrix} 0 & \sigma_3 \\ -\sigma_3 & 0 \end{pmatrix} = -i\gamma_3^{DR} \\ \gamma_4^{DR} \to \gamma_0 &= \begin{pmatrix} 0 & I \\ I & 0 \end{pmatrix} = \gamma_4^{DR} \ . \end{aligned} \tag{B.16}$$

The spatial ones are anti–hermitian. Since we defined γ_5^{DR} with $c_E = 1$ the fifth matrix will be unchanged in Minkowski space.

Appendix C

Ensembles properties of the $SU(4)$ study

C.1 Measurements of Correlation Functions

In this section we discuss the details behind the measurement of correlation functions $C^R_{ab}(t) \equiv C^R_{ab}(t,0)$

$$C^R_{ab}(t,0) = \frac{1}{L^3}\sum_{\boldsymbol{x}} \langle O^R_a(\boldsymbol{x},t) O^{R^\dagger}_b(0,t_i)\rangle \ , \qquad a,b = P,A \ , \tag{C.1}$$

where R denotes the representation of the fermionic fields. For each gauge configuration $n = 1,\dots N_{cfg}$ we average measurements performed every 4 source-times t_i, resulting in the correlator $C^R_{ab,\,n}(t)$,

$$C^R_{ab,\,n}(t) = \frac{8}{T}\sum_{t_i=0,4,\dots}^{T/2} C^R_{ab,\,n}(t,t_i) \ . \tag{C.2}$$

The gauge average $C^R_{PP}(t)$ and its variance $\delta C^R_{ab}(t)^2$ are then estimated from a new set of N correlators, $C^R_{ab,\,n'}$, resampled with a bootstrap procedure from $C^R_{ab,\,n}$. In this step, trajectories are discarded in order to account for the autocorrelation that is monitored across observables and ensembles according to C.2

$$C^R_{ab}(t) = \frac{1}{N'}\sum_{n'=0}^{N'-1} C^R_{ab,\,n'}\ , \qquad \delta C^R_{ab}(t)^2 = \frac{1}{N'}\sum_{n'=0}^{N'-1}\left[C^R_{ab,\,n'} - C^R_{ab}(t)\right]^2 \tag{C.3}$$

In order to suppress the excited states created by the hadronic operator in Eq. (C.1), we compute the two point functions by using different types of smearing on the fermionic fields. The procedure is not gauge invariant and requires working at fixed gauge. In particular, we adopt local ($\psi^R(x)$) and smeared ($\tilde{\psi}^R(x)$) fields

$$\begin{aligned}
\psi^R(x)^c_\alpha &= \int dy\, \delta(x-y)\delta_{\alpha\alpha'}\delta_{cc'}\, \psi^R(y)^{c'}_{\alpha'};, \\
\tilde{\psi}^R_g(x)^c_\alpha &= \int dy\, \frac{e^{-(x-y)^2/2g^2}}{\sqrt{2\pi}g}\delta_{\alpha\alpha'}\delta_{cc'}\psi^R(y)^{c'}_{\alpha'}\ ,
\end{aligned} \tag{C.4}$$

where c, c' are color indices, α, α' are Dirac indices and a sum is intended over α', c'. The parameter g can is tuned according to Section 4.5.2 in order to suppress the excited states in the spectral reconstruction. By combining local and smeared operators, we obtain three types of correlators: local-local, smeared-smeared, local-smeared. In the latter, the operators at the source and the sink are different, and this can produce negative contributions to the spectral density. As demonstrated in the Appendix of [105], such terms do not jeopardise the extraction of the spectral density from the correlators.

C.2 Autocorrelation Times

In an HMC algorithm, gauge configurations are generated through a Markov chain process. As a consequence, subsequent configurations can be correlated. Accounting for autocorrelation is essential in the estimation of observables through the Monte Carlo average. Consider a succession a_i of measurements of an observable A. We estimate the integrated autocorrelation time τ_{int} of

the observable A as

$$\tau_{int} = \frac{1}{2} + \sum_{t=1}^{W} \frac{\Gamma(t)}{\Gamma(0)} \,, \tag{C.5}$$

where t is the Monte Carlo time, W is the summation window, and $\Gamma(t)$ is our approximation of the autocorrelation function of the series:

$$\begin{aligned} &\Gamma(t) \simeq \frac{1}{N_{cfg} - t} \sum_{n=1}^{N_{cfg}-t} \left(a_n - \langle a_- \rangle\right) \left(a_{n+t} - \langle a_+ \rangle\right) \,, \\ &0 \leq t < N_{cfg} \,. \end{aligned} \tag{C.6}$$

$\langle a_- \rangle$ and $\langle a_+ \rangle$ are the averages over $N_{cfg} - t$ measurements, respectively the first and the last ones (see Section 4 of Ref. [119] for more details). In order to choose a summation window W of Eq. (C.5), we check at which Monte Carlo time t the function $\Gamma(t)/\Gamma(0)$ is smaller than twice its variance, which is estimated within the Madras Sokal approximation [117, 119]. Typical plots that we obtain for these quantities are shown in Fig. C.1 for the pseudoscalar-pseudoscalar correlator of fundamental fermions at different lattice times. In the top panel, our estimation of the autocorrelation function $\Gamma(t)/\Gamma(0)$ is plotted as a function of Monte Carlo time, showing the typical decaying behaviour. The bottom panel shows the integrated autocorrelation time τ_{int} of Eq. (C.5) for an increasing summation window W. The error is computed in the Madras Sokal approximation,

$$\langle \delta \tau_{int}^2 \rangle \simeq \frac{4W + 2}{N_{cfg}} \, \tau_{int}^2 \,. \tag{C.7}$$

In both panels, the correlation functions are computed for operators at different lattice times in order to monitor both the short and long distance behaviour. By knowing the correlation of an observable between trajectories in the HMC, we can establish how many of them have to be skipped performing the measurement. This is our strategy for the computation of the correlators on our ensembles. Alternatively, the naive estimate for the statistical error σ_0 of a given observable can be corrected to be $\sigma^2 = 2\tau_{int}\sigma_0^2$.
Accounting for autocorrelation has been essential in the following analysis, especially for those quantities computed in the proximity of the chiral limit, where the autocorrelation was more significant.

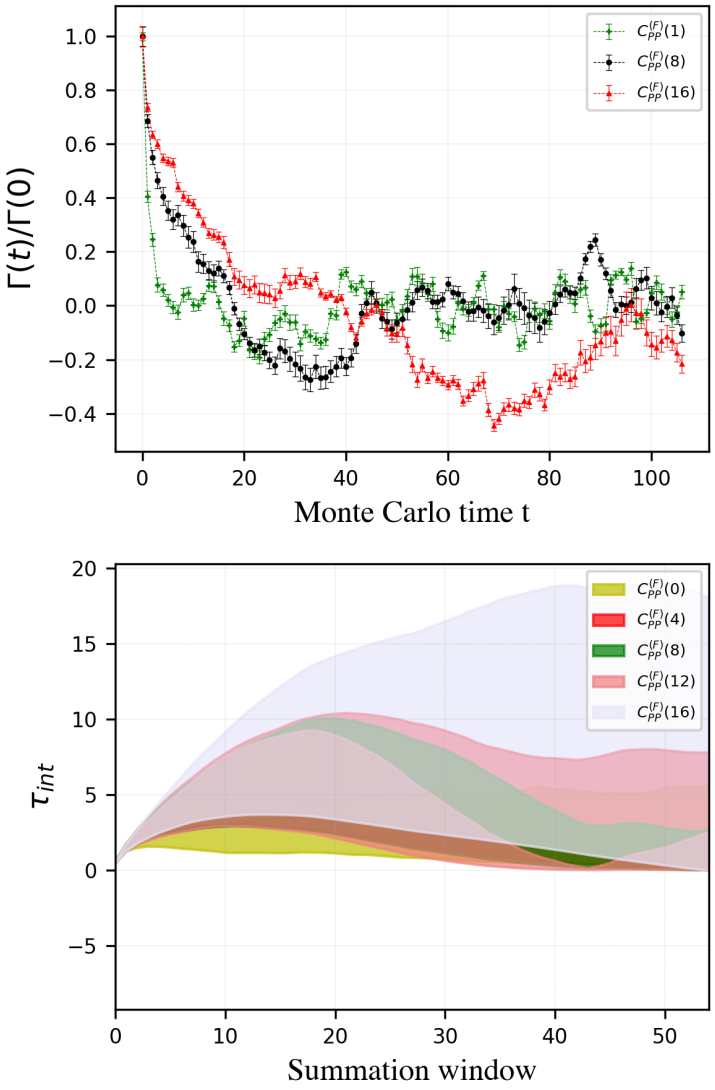

Figure C.1 *Top panel: autocorrelation function* $\Gamma(t)/\Gamma(0)$ *computed for the two point function of two pseudoscalar mesons with fermions in the fundamental representation. Different colors represent different intervals in lattice time between the source and the sink. Bottom panel: integrated autocorrelation time as a function of the summation window, computed for the same correlator on the top at several times. The two point function is obtained from the ensemble A0.*

C.3 Ensembles for $SU(4)$

Details about the gauge ensembles used for the study described in Chapter 4 are reported in Table C.1.

C.4 Masses for $SU(4)$

C.4.1 PCAC masses

Details about the PCAC masses measured within the study described in Chapter 4 are reported in Table C.1.

C.4.2 Meson masses

Details about the mesonic masses measured within the study described in Chapter 4 are reported in Table C.1.

	$am_0^{(\mathrm{Fund})}$	$am_0^{(2AS)}$	$\langle P \rangle$	N_{cfg}	$am_{PCAC}^{(\mathrm{Fund})}$	$am_{PCAC}^{(2AS)}$
A0	-0.45	-0.45	0.60893(2)	216	0.0468(23)	0.2327(37)
A1	-0.455	-0.45	0.60896(3)	99	0.0386(17)	0.2311(13)
A2	-0.46	-0.45	0.61392(2)	694	0.0332(26)	0.2290(30)
A3	-0.465	-0.45	0.60917(4)	82	0.0262(14)	0.2280(19)
A4	-0.47	-0.45	0.60942(1)	446	0.0209(29)	0.2277(35)
B0	-0.45	-0.54	0.61181(4)	65	0.0321(78)	0.1200(53)
B1	-0.45	-0.56	0.61259(2)	232	0.0338(94)	0.0988(40)
B2	-0.45	-0.58	0.61344(4)	243	0.0313(16)	0.0691(35)
B3	-0.45	-0.59	0.61392(2)	180	0.0306(36)	0.0544(19)
B3	-0.45	-0.60	0.61427(2)	176	0.0480(17)	0.0292(12)
C0	-0.47	-0.48	0.61011(3)	116	0.0205(34)	0.1962(54)
C1	-0.47	-0.52	0.61148(3)	78	0.0170(67)	0.1415(41)
C2	-0.47	-0.53	0.61203(3)	90	0.0143(56)	0.1279(39)
C3	-0.47	-0.54	0.61248(3)	92	0.0114(45)	0.1126(32)
C4	-0.47	-0.58	0.61398(6)	53	0.0068(15)	0.0651(27)
S0	-0.44	-0.60	0.61403(5)	43	0.0454(10)	0.0495(20)

Table C.1 *Ensembles used to extrapolate the chiral limit of the $SU(4)$ gauge theory with two fundamental and two two-index antisymmetric fermions. The coupling is $\beta = 11$, and the volume of the lattice is $16^3 \times 32$.*

$am_0^{(\mathrm{Fund})}$	$am_{PCAC}^{(\mathrm{Fund})}$	$am_{PCAC}^{(2AS)}$
-0.45	0.0468(23)	0.2327(37)
-0.455	0.0386(17)	0.2311(13)
-0.46	0.0332(26)	0.2290(30)
-0.465	0.0262(14)	0.2280(19)
-0.47	0.0209(29)	0.2277(35)

Table C.2 *PCAC masses for the fundamental representation used in the chiral extrapolation. The bare mass of the antisymmetric fermions is fixed at $am_0^{(2AS)} = -0.45$. They correspond to the ensembles A0-A4.*

$am_0^{(2AS)}$	$am_{PCAC}^{(2AS)}$	$am_{PCAC}^{(\text{Fund})}$	$am_0^{(2AS)}$	$am_{PCAC}^{(2AS)}$	$am_{PCAC}^{(\text{Fund})}$
-0.54	0.1200(53)	0.0321(78)	-0.48	0.1962(54)	0.0205(34)
-0.56	0.0988(40)	0.0338(94)	-0.52	0.1415(41)	0.0170(67)
-0.58	0.0691(35)	0.0313(16)	-0.53	0.1279(39)	0.0143(56)
-0.59	0.0544(19)	0.0306(36)	-0.54	0.1126(32)	0.0114(45)
-0.60	0.0480(17)	0.0292(12)	-0.58	0.0651(27)	0.0068(15)

Table C.3 *PCAC masses for the antisymmetric representation used in the chiral extrapolation. The values on the left are obtained with* $am_0^{(\text{Fund})} = -0.45$ *(ensembles B0-B4), the ones on the right with* $am_0^{(\text{Fund})} = -0.47$ *(ensembles C0-C4).*

$am_0^{(\text{Fund})}$	$aM_{PP}^{(\text{Fund})}$	$aM_{PP}^{(2AS)}$	$am_0^{(2AS)}$	$aM_{PP}^{(2AS)}$	$aM_{PP}^{(\text{Fund})}$
-0.45	0.3555(38)	0.8037(14)	-0.54	0.5426(22)	0.375(36)
-0.455	0.290(60)	0.7701(31)	-0.56	0.4638(33)	0.3114(69)
-0.46	0.280(16)	0.7640(28)	-0.58	0.4035(24)	0.3147(40)
-0.465	0.254(16)	0.7635(29)	-0.59	0.3600(38)	0.3038(67)
-0.47	0.255(10)	0.7634(20)	-0.60	0.3407(48)	0.321(13)

Table C.4 *Masses of the pseudoscalar mesons. On the left, we vary the bare fundamental mass while keeping* $am_0^{(\text{2AS})} = -0.45$ *(ensembles A0-A4). Conversely, on the right the fundamental bare mass is fixed at* $am_0^{(\text{Fund})} = -0.45$ *(ensembles B0-B4).*

$a\sigma$	$aM_{\text{PP}}^{(\text{2AS})}$	$\chi^2_{f_\sigma^{(n)}}$ / d.o.f.	n
0.18	0.3558(30)	0.61	2
0.19	0.3505(33)	0.75	2
0.2	0.3550(23)	1.36	2
0.21	0.3554(22)	0.81	2
0.22	0.3523(26)	1.18	2
0.23	0.3580(22)	2.13	2
0.24	0.3557(24)	1.58	2
0.19	0.3498(37)	0.71	3
0.2	0.3516(32)	0.96	3
0.21	0.3534(29)	1.80	3
0.22	0.3505(33)	1.38	3
0.23	0.3592(25)	2.04	3

Table C.5 *Fit results for* $aM_{PP}^{(2AS)}$ *from smeared spectral densities for different smearing radii* σ *and different number of states* n*. These values appear in Fig. 4.13.*

Bibliography

[1] Luigi Del Debbio, Alessandro Lupo, Marco Panero, and Nazario Tantalo. Multi-representation dynamics of SU(4) composite Higgs models: chiral limit and spectral reconstructions. *Eur. Phys. J. C*, 83(3):220, 2023.

[2] Ed Bennett, Peter Boyle, Luigi Del Debbio, Niccolò Forzano, Deog Ki Hong, Jong-Wan Lee, Julian Lenz, C-J David Lin, Biagio Lucini, Alessandro Lupo, Maurizio Piai, and Davide Vadacchino. Symplectic lattice gauge theories on Grid: approaching the conformal window. -, -, 6 2023.

[3] Andreas S. Kronfeld. Twenty-first Century Lattice Gauge Theory: Results from the QCD Lagrangian. *Ann. Rev. Nucl. Part. Sci.*, 62:265–284, 2012.

[4] Thomas A. Ryttov and Robert Shrock. Scheme-Independent Calculations of Properties at a Conformal Infrared Fixed Point in Gauge Theories with Multiple Fermion Representations. *Phys. Rev. D*, 98(9):096003, 2018.

[5] Byung Su Kim, Deog Ki Hong, and Jong-Wan Lee. Into the conformal window: Multirepresentation gauge theories. *Phys. Rev. D*, 101(5):056008, 2020.

[6] Thomas A. Ryttov and Francesco Sannino. Supersymmetry inspired QCD beta function. *Phys. Rev. D*, 78:065001, 2008.

[7] Thomas A. Ryttov and Robert Shrock. Higher-order scheme-independent series expansions of $\gamma_{\bar{\psi}\psi,IR}$ and β'_{IR} in conformal field theories. *Phys. Rev. D*, 95(10):105004, 2017.

[8] Jong-Wan Lee. Conformal window from conformal expansion. *Phys. Rev. D*, 103(7):076006, 2021.

[9] T. van Ritbergen, J. A. M. Vermaseren, and S. A. Larin. The Four loop beta function in quantum chromodynamics. *Phys. Lett. B*, 400:379–384, 1997.

[10] Ed Bennett, Deog Ki Hong, Jong-Wan Lee, C. J. David Lin, Biagio Lucini, Maurizio Piai, and Davide Vadacchino. Sp(4) gauge theory on the lattice: towards SU(4)/Sp(4) composite Higgs (and beyond). *JHEP*, 03:185, 2018.

[11] K. Holland, M. Pepe, and U. J. Wiese. The Deconfinement phase transition of Sp(2) and Sp(3) Yang-Mills theories in (2+1)-dimensions and (3+1)-dimensions. *Nucl. Phys. B*, 694:35–58, 2004.

[12] E. Follana and H. Panagopoulos. The Critical mass of Wilson fermions: A Comparison of perturbative and Monte Carlo results. *Phys. Rev. D*, 63:017501, 2001.

[13] Guido Cossu, Luigi Del Debbio, Marco Panero, and David Preti. Strong dynamics with matter in multiple representations: SU(4) gauge theory with fundamental and sextet fermions. *Eur. Phys. J. C*, 79(8):638, 2019.

[14] Martin Lüscher. Properties and uses of the Wilson flow in lattice QCD. *JHEP*, 08:071, 2010. [Erratum: JHEP 03, 092 (2014)].

[15] Martin Lüscher. Future applications of the Yang-Mills gradient flow in lattice QCD. *PoS*, LATTICE2013:016, 2014.

[16] Bennett, Deog Ki Hong, Jong-Wan Lee, C. J. David Lin, Biagio Lucini, Maurizio Piai, and Davide Vadacchino. Sp(2N) Yang-Mills theories on the lattice: Scale setting and topology. *Phys. Rev. D*, 106(9):094503, 2022.

[17] B. Sheikholeslami and R. Wohlert. Improved Continuum Limit Lattice Action for QCD with Wilson Fermions. *Nucl. Phys. B*, 259:572, 1985.

[18] M. Hasenbusch and K. Jansen. Speeding up lattice QCD simulations with clover improved Wilson fermions. *Nucl. Phys. B*, 659:299–320, 2003.

[19] Gabriele Ferretti and Denis Karateev. Fermionic UV completions of Composite Higgs models. *JHEP*, 03:077, 2014.

[20] Sidney R. Coleman, J. Wess, and Bruno Zumino. Structure of phenomenological Lagrangians. 1. *Phys. Rev.*, 177:2239–2247, 1969.

[21] Curtis G. Callan, Jr., Sidney R. Coleman, J. Wess, and Bruno Zumino. Structure of phenomenological Lagrangians. 2. *Phys. Rev.*, 177:2247–2250, 1969.

[22] H. Leutwyler. On the foundations of chiral perturbation theory. *Annals Phys.*, 235:165–203, 1994.

[23] J. Gasser and H. Leutwyler. Chiral Perturbation Theory: Expansions in the Mass of the Strange Quark. *Nucl. Phys. B*, 250:465–516, 1985.

[24] Markus A. Luty. Strong Conformal Dynamics at the LHC and on the Lattice. *JHEP*, 04:050, 2009.

[25] Thomas DeGrand. Finite-size scaling tests for SU(3) lattice gauge theory with color sextet fermions. *Phys. Rev. D*, 80(11):114507, 2009.

[26] Luigi Del Debbio, Biagio Lucini, Agostino Patella, Claudio Pica, and Antonio Rago. Mesonic spectroscopy of Minimal Walking Technicolor. *Phys. Rev. D*, 82:014509, 2010.

[27] Luigi Del Debbio and Roman Zwicky. Scaling relations for the entire spectrum in mass-deformed conformal gauge theories. *Phys. Lett. B*, 700:217–220, 2011.

[28] Agostino Patella. A precise determination of the psibar-psi anomalous dimension in conformal gauge theories. *Phys. Rev. D*, 86:025006, 2012.

[29] Shinya Matsuzaki and Koichi Yamawaki. Dilaton Chiral Perturbation Theory: Determining the Mass and Decay Constant of the Technidilaton on the Lattice. *Phys. Rev. Lett.*, 113(8):082002, 2014.

[30] Maarten Golterman and Yigal Shamir. Low-energy effective action for pions and a dilatonic meson. *Phys. Rev. D*, 94(5):054502, 2016.

[31] Maarten Golterman and Yigal Shamir. Explorations beyond dilaton chiral perturbation theory in the eight-flavor SU(3) gauge theory. *Phys. Rev. D*, 102:114507, 2020.

[32] Thomas Appelquist, James Ingoldby, and Maurizio Piai. Dilaton EFT Framework For Lattice Data. *JHEP*, 07:035, 2017.

[33] Maarten Golterman and Yigal Shamir. Large-mass regime of the dilaton-pion low-energy effective theory. *Phys. Rev. D*, 98(5):056025, 2018.

[34] Oscar Catà and Christoph Müller. Chiral effective theories with a light scalar at one loop. *Nucl. Phys. B*, 952:114938, 2020.

[35] Thomas Appelquist, James Ingoldby, and Maurizio Piai. Dilaton Effective Field Theory. *Universe*, 9(1):10, 2023.

[36] Tom Banks and A. Zaks. On the Phase Structure of Vector-Like Gauge Theories with Massless Fermions. *Nucl. Phys. B*, 196:189–204, 1982.

[37] Michael E. Peskin. The Alignment of the Vacuum in Theories of Technicolor. *Nucl. Phys. B*, 175:197–233, 1980.

[38] Georges Aad et al. Observation of a new particle in the search for the Standard Model Higgs boson with the ATLAS detector at the LHC. *Phys. Lett. B*, 716:1–29, 2012.

[39] Serguei Chatrchyan et al. Observation of a New Boson at a Mass of 125 GeV with the CMS Experiment at the LHC. *Phys. Lett. B*, 716:30–61, 2012.

[40] Giuliano Panico and Andrea Wulzer. *The Composite Nambu-Goldstone Higgs*, volume 913. Springer, 2016.

[41] Michael J. Dugan, Howard Georgi, and David B. Kaplan. Anatomy of a Composite Higgs Model. *Nucl. Phys. B*, 254:299–326, 1985.

[42] R. L. Workman et al. Review of Particle Physics. *PTEP*, 2022:083C01, 2022.

[43] David B. Kaplan. Flavor at SSC energies: A New mechanism for dynamically generated fermion masses. *Nucl. Phys. B*, 365:259–278, 1991.

[44] Ed Bennett, Deog Ki Hong, Jong-Wan Lee, C. J. David Lin, Biagio Lucini, Maurizio Piai, and Davide Vadacchino. Sp(4) gauge theories on the lattice: $N_f = 2$ dynamical fundamental fermions. *JHEP*, 12:053, 2019.

[45] Ed Bennett, Deog Ki Hong, Jong-Wan Lee, Chi-Jen David Lin, Biagio Lucini, Michele Mesiti, Maurizio Piai, Jarno Rantaharju, and Davide Vadacchino. $Sp(4)$ gauge theories on the lattice: quenched fundamental and antisymmetric fermions. *Phys. Rev. D*, 101(7):074516, 2020.

[46] Ed Bennett, Jack Holligan, Deog Ki Hong, Jong-Wan Lee, C. J. David Lin, Biagio Lucini, Maurizio Piai, and Davide Vadacchino. Glueballs and strings in $Sp(2N)$ Yang-Mills theories. *Phys. Rev. D*, 103(5):054509, 2021.

[47] Bennett, Deog Ki Hong, Ho Hsiao, Jong-Wan Lee, C. J. David Lin, Biagio Lucini, Michele Mesiti, Maurizio Piai, and Davide Vadacchino. Lattice studies of the Sp(4) gauge theory with two fundamental and three antisymmetric Dirac fermions. *Phys. Rev. D*, 106(1):014501, 2022.

[48] Venkitesh Ayyar, Thomas DeGrand, Daniel C. Hackett, William I. Jay, Ethan T. Neil, Yigal Shamir, and Benjamin Svetitsky. Partial compositeness and baryon matrix elements on the lattice. *Phys. Rev. D*, 99(9):094502, 2019.

[49] Venkitesh Ayyar, Thomas Degrand, Daniel C. Hackett, William I. Jay, Ethan T. Neil, Yigal Shamir, and Benjamin Svetitsky. Baryon spectrum of SU(4) composite Higgs theory with two distinct fermion representations. *Phys. Rev. D*, 97(11):114505, 2018.

[50] Venkitesh Ayyar, Thomas DeGrand, Maarten Golterman, Daniel C. Hackett, William I. Jay, Ethan T. Neil, Yigal Shamir, and Benjamin Svetitsky. Spectroscopy of SU(4) composite Higgs theory with two distinct fermion representations. *Phys. Rev. D*, 97(7):074505, 2018.

[51] Y. Aoki et al. FLAG Review 2021. *Eur. Phys. J. C*, 82(10):869, 2022.

[52] Luigi Del Debbio, Mads T. Frandsen, Haralambos Panagopoulos, and Francesco Sannino. Higher representations on the lattice: Perturbative studies. *JHEP*, 06:007, 2008.

[53] Bennett, Ho Hsiao, Jong-Wan Lee, Biagio Lucini, Axel Maas, Maurizio Piai, and Fabian Zierler. Singlets in gauge theories with fundamental matter. -, -, 4 2023.

[54] Ed Bennett, Jack Holligan, Deog Ki Hong, Ho Hsiao, Jong-Wan Lee, C. J. David Lin, Biagio Lucini, Michele Mesiti, Maurizio Piai, and Davide Vadacchino. Sp(2N) Lattice Gauge Theories and Extensions of the Standard Model of Particle Physics. *Universe*, 9(5):236, 2023.

[55] Peter A. Boyle, Guido Cossu, Azusa Yamaguchi, and Antonin Portelli. Grid: A next generation data parallel C++ QCD library. *PoS*, LATTICE2015:023, 2016.

[56] Gabriele Ferretti. UV Completions of Partial Compositeness: The Case for a SU(4) Gauge Group. *JHEP*, 06:142, 2014.

[57] Yonit Hochberg, Eric Kuflik, Tomer Volansky, and Jay G. Wacker. Mechanism for Thermal Relic Dark Matter of Strongly Interacting Massive Particles. *Phys. Rev. Lett.*, 113:171301, 2014.

[58] Yonit Hochberg, Eric Kuflik, Hitoshi Murayama, Tomer Volansky, and Jay G. Wacker. Model for Thermal Relic Dark Matter of Strongly Interacting Massive Particles. *Phys. Rev. Lett.*, 115(2):021301, 2015.

[59] Yonit Hochberg, Eric Kuflik, and Hitoshi Murayama. SIMP Spectroscopy. *JHEP*, 05:090, 2016.

[60] Suchita Kulkarni, Axel Maas, Seán Mee, Marco Nikolic, Josef Pradler, and Fabian Zierler. Low-energy effective description of dark $Sp(4)$ theories. *SciPost Phys.*, 14:044, 2023.

[61] Fabian Zierler, Suchita Kulkarni, Axel Maas, Seán Mee, Marco Nikolic, and Josef Pradler. Strongly Interacting Dark Matter from Sp(4) Gauge Theory. *EPJ Web Conf.*, 274:08014, 2022.

[62] Naoki Seto, Seiji Kawamura, and Takashi Nakamura. Possibility of direct measurement of the acceleration of the universe using 0.1-Hz band laser interferometer gravitational wave antenna in space. *Phys. Rev. Lett.*, 87:221103, 2001.

[63] Seiji Kawamura et al. The Japanese space gravitational wave antenna: DECIGO. *Class. Quant. Grav.*, 28:094011, 2011.

[64] Jeff Crowder and Neil J. Cornish. Beyond LISA: Exploring future gravitational wave missions. *Phys. Rev. D*, 72:083005, 2005.

[65] Vincent Corbin and Neil J. Cornish. Detecting the cosmic gravitational wave background with the big bang observer. *Class. Quant. Grav.*, 23:2435–2446, 2006.

[66] John Baker et al. The Laser Interferometer Space Antenna: Unveiling the Millihertz Gravitational Wave Sky. -, -, 7 2019.

[67] Benjamin P Abbott et al. Exploring the Sensitivity of Next Generation Gravitational Wave Detectors. *Class. Quant. Grav.*, 34(4):044001, 2017.

[68] Edward Witten. Cosmic Separation of Phases. *Phys. Rev. D*, 30:272–285, 1984.

[69] Marc Kamionkowski, Arthur Kosowsky, and Michael S. Turner. Gravitational radiation from first order phase transitions. *Phys. Rev. D*, 49:2837–2851, 1994.

[70] Pedro Schwaller. Gravitational Waves from a Dark Phase Transition. *Phys. Rev. Lett.*, 115(18):181101, 2015.

[71] Djuna Croon, Verónica Sanz, and Graham White. Model Discrimination in Gravitational Wave spectra from Dark Phase Transitions. *JHEP*, 08:203, 2018.

[72] James Halverson, Cody Long, Anindita Maiti, Brent Nelson, and Gustavo Salinas. Gravitational waves from dark Yang-Mills sectors. *JHEP*, 05:154, 2021.

[73] Giacomo Cacciapaglia, Claudio Pica, and Francesco Sannino. Fundamental Composite Dynamics: A Review. *Phys. Rept.*, 877:1–70, 2020.

[74] Oliver Witzel. Review on Composite Higgs Models. *PoS*, LATTICE2018:006, 2019.

[75] R. Sekhar Chivukula. Lectures on technicolor and compositeness. In *Theoretical Advanced Study Institute in Elementary Particle Physics (TASI 2000): Flavor Physics for the Millennium*, pages 731–772, 6 2000.

[76] Francesco Sannino. Conformal Dynamics for TeV Physics and Cosmology. *Acta Phys. Polon. B*, 40:3533–3743, 2009.

[77] Maurizio Piai. Lectures on walking technicolor, holography and gauge/gravity dualities. *Adv. High Energy Phys.*, 2010:464302, 2010.

[78] Yasumichi Aoki et al. Light composite scalar in eight-flavor QCD on the lattice. *Phys. Rev. D*, 89:111502, 2014.

[79] Yasumichi Aoki et al. Light flavor-singlet scalars and walking signals in $N_f = 8$ QCD on the lattice. *Phys. Rev. D*, 96(1):014508, 2017.

[80] T. Appelquist et al. Nonperturbative investigations of SU(3) gauge theory with eight dynamical flavors. *Phys. Rev. D*, 99(1):014509, 2019.

[81] T. Appelquist et al. Goldstone boson scattering with a light composite scalar. *Phys. Rev. D*, 105(3):034505, 2022.

[82] Anna Hasenfratz. Emergent strongly coupled ultraviolet fixed point in four dimensions with eight Kähler-Dirac fermions. *Phys. Rev. D*, 106(1):014513, 2022.

[83] Zoltan Fodor, Kieran Holland, Julius Kuti, Daniel Nogradi, Chris Schroeder, and Chik Him Wong. Can the nearly conformal sextet gauge model hide the Higgs impostor? *Phys. Lett. B*, 718:657–666, 2012.

[84] Chung Ngoc Leung, S. T. Love, and William A. Bardeen. Spontaneous Symmetry Breaking in Scale Invariant Quantum Electrodynamics. *Nucl. Phys. B*, 273:649–662, 1986.

[85] William A. Bardeen, Chung Ngoc Leung, and S. T. Love. The Dilaton and Chiral Symmetry Breaking. *Phys. Rev. Lett.*, 56:1230, 1986.

[86] Walter D. Goldberger, Benjamin Grinstein, and Witold Skiba. Distinguishing the Higgs boson from the dilaton at the Large Hadron Collider. *Phys. Rev. Lett.*, 100:111802, 2008.

[87] Azusa Yamaguchi, Peter Boyle, Guido Cossu, Gianluca Filaci, Christoph Lehner, and Antonin Portelli. Grid: OneCode and FourAPIs. *PoS*, LATTICE2021:035, 2022.

[88] S. Duane, A. D. Kennedy, B. J. Pendleton, and D. Roweth. Hybrid Monte Carlo. *Phys. Lett. B*, 195:216–222, 1987.

[89] Kenneth G. Wilson. Confinement of Quarks. *Phys. Rev. D*, 10:2445–2459, 1974.

[90] Holger Bech Nielsen and M. Ninomiya. No Go Theorem for Regularizing Chiral Fermions. *Phys. Lett. B*, 105:219–223, 1981.

[91] K. Symanzik. Continuum Limit and Improved Action in Lattice Theories. 1. Principles and φ^4 Theory. *Nucl. Phys. B*, 226:187–204, 1983.

[92] K. Symanzik. Continuum Limit and Improved Action in Lattice Theories. 2. O(N) Nonlinear Sigma Model in Perturbation Theory. *Nucl. Phys. B*, 226:205–227, 1983.

[93] Martin Luscher, Stefan Sint, Rainer Sommer, and Peter Weisz. Chiral symmetry and O(a) improvement in lattice QCD. *Nucl. Phys. B*, 478:365–400, 1996.

[94] Luigi Del Debbio, Agostino Patella, and Claudio Pica. Higher representations on the lattice: Numerical simulations. SU(2) with adjoint fermions. *Phys. Rev. D*, 81:094503, 2010.

[95] H. Panagopoulos and E. Vicari. Resummation of cactus diagrams in lattice QCD. *Phys. Rev. D*, 58:114501, 1998.

[96] C. Alexandrou, M. Constantinou, T. Korzec, H. Panagopoulos, and F. Stylianou. Renormalization constants of local operators for Wilson type improved fermions. *Phys. Rev. D*, 86:014505, 2012.

[97] M. Constantinou, H. Panagopoulos, and A. Skouroupathis. Improved perturbation theory for improved lattice actions. *Phys. Rev. D*, 74:074503, 2006.

[98] I.P. Omelyan, I.M. Mryglod, and R. Folk. Symplectic analytically integrable decomposition algorithms: classification, derivation, and application to molecular dynamics, quantum and celestial mechanics simulations. *Computer Physics Communications*, 151(3):272–314, 2003.

[99] S. Musberg, G. Münster, and S. Piemonte. Perturbative calculation of the clover term for Wilson fermions in any representation of the gauge group SU(N). *JHEP*, 05:143, 2013.

[100] L. Del Debbio, Leonardo Giusti, M. Lüscher, R. Petronzio, and N. Tantalo. Stability of lattice QCD simulations and the thermodynamic limit. *JHEP*, 02:011, 2006.

[101] Antonin Portelli, Ryan Abott, Nils Asmussen, Alessandro Barone, Peter A Boyle, Felix Erben, Nelson Lachini, Michael Marshall, Vera Gülpers, Ryan C Hill, Raoul Hodgson, Fabian Joswig, Fionn Ó hÓgáin, and James P Richings. aportelli/hadrons: Hadrons v1.3, March 2022.

[102] Benoit Blossier, Michele Della Morte, Georg von Hippel, Tereza Mendes, and Rainer Sommer. On the generalized eigenvalue method for energies and matrix elements in lattice field theory. *JHEP*, 04:094, 2009.

[103] John Bulava, Maxwell T. Hansen, Michael W. Hansen, Agostino Patella, and Nazario Tantalo. Inclusive rates from smeared spectral densities in the two-dimensional O(3) non-linear σ-model. *JHEP*, 07:034, 2022.

[104] Maxwell T. Hansen, Harvey B. Meyer, and Daniel Robaina. From deep inelastic scattering to heavy-flavor semileptonic decays: Total rates into multihadron final states from lattice QCD. *Phys. Rev. D*, 96(9):094513, 2017.

[105] Martin Hansen, Alessandro Lupo, and Nazario Tantalo. Extraction of spectral densities from lattice correlators. *Phys. Rev. D*, 99(9):094508, 2019.

[106] John Bulava and Maxwell T. Hansen. Scattering amplitudes from finite-volume spectral functions. *Phys. Rev. D*, 100(3):034521, 2019.

[107] Paolo Gambino, Shoji Hashimoto, Sandro Mächler, Marco Panero, Francesco Sanfilippo, Silvano Simula, Antonio Smecca, and Nazario Tantalo. Lattice QCD study of inclusive semileptonic decays of heavy mesons. *JHEP*, 07:083, 2022.

[108] Mattia Bruno and Maxwell T. Hansen. Variations on the Maiani-Testa approach and the inverse problem. *JHEP*, 06:043, 2021.

[109] Gabriela Bailas, Shoji Hashimoto, and Tsutomu Ishikawa. Reconstruction of smeared spectral function from Euclidean correlation functions. *PTEP*, 2020(4):043B07, 2020.

[110] George Backus and Freeman Gilbert. The Resolving Power of Gross Earth Data. *Geophysical Journal International*, 16(2):169–205, 10 1968.

[111] Tetsuya Takaishi and Philippe de Forcrand. Testing and tuning new symplectic integrators for hybrid Monte Carlo algorithm in lattice QCD. *Phys. Rev. E*, 73:036706, 2006.

[112] M. Creutz. Global Monte Carlo algorithms for many-fermion systems. *Phys. Rev. D*, 38:1228–1238, 1988.

[113] Tetsuya Takaishi. Choice of integrator in the hybrid Monte Carlo algorithm. *Comput. Phys. Commun.*, 133:6–17, 2000.

[114] Sourendu Gupta, A. Irback, F. Karsch, and B. Petersson. The Acceptance Probability in the Hybrid Monte Carlo Method. *Phys. Lett. B*, 242:437–443, 1990.

[115] M. A. Clark and A. D. Kennedy. The RHMC algorithm for two flavors of dynamical staggered fermions. *Nucl. Phys. B Proc. Suppl.*, 129:850–852, 2004.

[116] Jong-Wan Lee, Ed Bennett, Deog Ki Hong, C. J. David Lin, Biagio Lucini, Maurizio Piai, and Davide Vadacchino. Progress in the lattice simulations of Sp($2N$) gauge theories. *PoS*, LATTICE2018:192, 2018.

[117] Neal Madras and Alan D. Sokal. The Pivot algorithm: a highly efficient Monte Carlo method for selfavoiding walk. *J. Statist. Phys.*, 50:109–186, 1988.

[118] Paolo Gambino and Shoji Hashimoto. Inclusive Semileptonic Decays from Lattice QCD. *Phys. Rev. Lett.*, 125(3):032001, 2020.

[119] L. Del Debbio, Leonardo Giusti, M. Luscher, R. Petronzio, and N. Tantalo. QCD with light Wilson quarks on fine lattices. II. DD-HMC simulations and data analysis. *JHEP*, 02:082, 2007.